Orographic Controls on Extreme Precipitation associated with a Mei-yu Front

Ian C. Cornejo

A Thesis submitted in partial fulfillment of
the requirements for the degree of
Master of Science
(Atmospheric and Oceanic Sciences)

at the
University of Wisconsin-Madison
2023

Abstract

Taiwan regularly receives extreme rainfall due to seasonal Mei-yu fronts that are modified by Taiwan's steep and complex topography. One such case occurred between 1-3 June 2017 when a Mei-yu front produced severe flooding and landslides as a result of over 600 mm of rainfall in 12 hours near Taipei basin, and over 1500 mm of rainfall in 2 days near the Central Mountain Range (CMR). This Mei-yu front event is simulated using the Weather Research and Forecasting (WRF) model with halved terrain as a sensitivity test to better understand the orographic mechanisms that modify the intensity, duration, and location of extreme rainfall.

The reduction in terrain height in WRF produced a decrease in rainfall duration and accumulation in Northern Taiwan and a decrease in rainfall duration, intensity, and accumulation over the CMR. The reductions in Northern Taiwan are linked to a weaker orographic barrier jet resulting from a lowered terrain height. With a weaker barrier jet, the front propagates south faster, decreasing the time rainfall accrues in Northern Taiwan. The reductions in rainfall intensity and duration over the CMR are partially explained by a lack of orographic enhancements to Mei-Yu frontogenesis near the terrain. A prominent feature missing with the reduced terrain is a redirection of postfrontal westerly winds attributed to orographic deformation. These orographically deforming winds converge with prefrontal flow to maintain the Mei-Yu front. These orographic features will be further explored using observations of heavy rainfall events captured during the Prediction of Rainfall Extremes Campaign in the Pacific 2022 field campaign in Taiwan.

Dedication

For my father, an enduring inspiration

Acknowledgements

I'd like to express gratitude to all the people to got me this point. First and foremost, I want to thank my advisor, Angela Rowe, for accepting me into her lab as well as her continued guidance, support, and unfathomable patience. I would also like to thank my other committee members, Dr. Jonathan Martin and Dr. Tristan L'Ecuyer, for their advice and insight as I progressed through my research. Within the AOS department, I'd like to thank all the faculty, staff, and students I've interacted with while I've been a part of this community. There isn't a day that goes by where I'm not amazed by the talent and expertise just outside my office door.

Outside of the department, I'd like to thank everyone involved in the PRECIP 2022 field campaign. I'm grateful for the advice, feedback, and support provided by the orographic team, radar team, and the modeling team. I've felt like I've learned so much from each and every member and I'm proud to participate in such a great project.

Lastly, I want to thank my family. I thank my mother, my father, my kuya, my sister-in-law, and my nephew for supporting me and encouraging me to strive for more.

For everyone who has helped me in some way, thank you.

This research is supported by the National Science Foundation (AGS-2013743), the Cooperative Institute for Meteorological Satellite Studies, and the Advanced Opportunity Fellowship.

Contents

Acronyms

BJ Barrier Jet.

CAPE Convective Available Potential Energy.

CIN Convetive Inhibition.

CMR Central Mountain Range.

CWB Central Weather Bureau.

ECMWF European Centre for Medium-Range Weather Forecasts.

ERA5 ECMWF Reanalysis v5.

IOP Intensive Observation Period.

LLJ Low Level Jet.

MBLJ Marine Boundary Layer Jet.

NCAR National Center for Atmospheric Research.

NWS National Weather Service.

PRECIP Prediction of Rainfall Extremes Campaign in the Pacific.

QPESUMS Quantitative Precipitation Estimation and Segregation Using Multiple Sensors.

RCCG Radar Code of Chigu.

RCWF Radar Code of Wu-FenShan.

RIP Read/Interpolate/Plot.

SCS South China Sea.

SLLJ Synoptic Low Level Jet.

SMR Snow Mountain Range.

SoWMEX Southwest Monsoon Experiment.

TAMEX Taiwan Area Mesoscale Experiment.

TiMREX Terrain-influenced Monsoon Rainfall Experiment.

WEPS WRF Ensemble Prediction System.

WRF Weather Research and Forecasting model.

List of Figures

List of Tables

Chapter 1

Introduction

1.1 Defining Extreme Rainfall

Rainfall is a phenomenon almost ubiquitous across the world. The effects of a single rainfall event could be momentous, signaling the end of a drought (Antofie et al. 2015) or putting a stop to a wildfire (Reid et al. 2010). It can also be disastrous, creating flash floods (Chi and Jian 2008) or over watering crops (Liu et al. 2022). As rainfall scales from light to extreme, the danger and impact associated with such an event amplifies. The classification of "extreme" rainfall is tricky, however. Although rainfall accumulation can be viewed as an objective variable for determining extreme rainfall, it's actually rather contextual and requires the proper context.

For example, the great Colorado flood of September 2013 was the result of rainfall exceeding 450 mm over an 8-day period (Gochis et al. 2015). The floods as well as numerous landslides proved to be a socio-economical nightmare leading to emergency evacuations, multiple fatalities, and damages with an estimated cost over $2 billion. Records were shattered during this event with a rain gauge at Fort Carson, Colorado recording a 24-hour rainfall maximum of 316 mm between the 12th and 13th and the nearby National Weather Service forecast office in Denver reporting the wettest September on record (NWS 2015). Although this event was a climatological extreme for Colorado, when contrasted with a region like Taiwan, the rainfall totals pale in comparison. A rain gauge climatology for

the southern city Kaohsiung, Taiwan reveals average rainfall accumulation for the month of June to be just under 400 mm, nearing the extremes of the great Colorado floods (Jong et al. 2011). The joint Terrain Induced Monsoon Rainfall Experiment (TiMREX) / Southwest Monsoon Experiment (SoWMEX) of 2008 highlight a local extreme in Kaohsiung capturing approximately 1200 mm of rainfall during the month of June. Despite the rain associated with the great Colorado floods of September 2013 shattering multiple local records, it would be treated as commonplace in Taiwan.

We find that although "extreme" rainfall is highly contextual, commonalities can be found within each extreme rainfall event. For instance, extreme rainfall in Colorado may have similarities to extreme rainfall in Taiwan with both environments being regions of complex terrain known for orographically-enhanced precipitation. By breaking individual events into their characteristic components, whether they be sources of lift, moisture, instability, etc., an objective method of studying extreme rainfall can be used to improve our understanding of extreme rainfall formation, prediction, and effects.

One of the formative frameworks for understanding extreme rainfall was proposed by Doswell et al. (1996) whereby precipitation, P, could be expressed as:

$$P = RD \tag{1.1}$$

Where R is the rainfall intensity and D is the duration of the rainfall. With these two variables, precipitation can be defined by scaling rainfall intensity and duration to create a spectrum of light to extreme rainfall with absolute magnitudes varying by climatic region.

To understand the ingredients contributing to rainfall, intensity and duration can be expressed as:

$$R = E(\frac{\rho}{\rho_w})(wq_v) \tag{1.2}$$

$$D = \frac{L_s}{C_s} \tag{1.3}$$

Where E is precipitation efficiency, ρ/ρ_w is a relative moisture density, wq_v is a vertical moisture flux, L_s is a storm length scale, and C_s is a storm relative motion vector. Rainfall

intensity becomes a function of high vertical forcing of moisture such as observed within a deep convective core. Rainfall duration is a function of high horizontal forcing of moisture such as that replenishing broad stratiform precipitation. Therefore, duration can increase either through broadening the spatial coverage of a storm or through stalling a storm over a location.

These ingredients reveal that individual storm types can be placed on the intensity and duration spectrum to compare with one another (Fig. 1.1). Deep convective cores are likely to inhabit the high intensity, low duration side of the spectrum, whereas stratiform rainfall might inhabit the high duration, low intensity side of the spectrum. Tropical cyclones may lead to extreme rainfall through exhibiting both high intensity and duration. The great Colorado flood of September 2013 was characterized by orographically lifted, stratiform rainfall with embedded convective cells (Gochis et al. 2015) similar to multiple intensive observation periods (IOPs) as part of TiMREX/SoWMEX (Jong et al. 2011). Therefore, there is a necessity to incorporate topography into this framework. The overarching goal of this research will be determining how topography modifies not only the intensity and duration of rainfall, but the location of it as well. By understanding this modification, the ability to predict and forecast orographic precipitation improves.

1.2 Taiwan as a Precipitation Laboratory

One of the major centers for studying extreme orographic precipitation is Taiwan due to the steep topography that makes up much of the island (Fig. 1.2). Two major mountain ranges, the Zhongyang Range, or Central Mountain Range (CMR), which runs south-southwest to north-northeast and the Xueshan Range, also referred to as the Snow Mountain Range (SMR), which runs southwest to northeast, cover roughly two thirds of the entire island with complex terrain. The maximum terrain height on the island is found at Yushan, or Jade Mountain, (23.47°N, 120.96°E) with an altitude of 3952 m. With such steep topography isolated to a small island in the Pacific Ocean, Taiwan makes for an ideal location to study orographic precipitation. Precipitation in the most densely

populated region of Taiwan, Taipei basin (25.03°N, 121.57°E), is often heavily influenced by the nearby SMR and the mountains found at Yangmingshan National Park (25.17°N, 121.55°E) (Tu et al. 2022).

With such complex topography, Taiwan has hosted numerous field campaigns revolving around orographic precipitation. Major field campaigns include the Taiwan Mesoscale Experiment (TAMEX) in 1987 (Kuo and Chen 1990) and the TiMREX/SoWMEX experiments in 2008 (Jong et al. 2011). One of the most recent projects was the Prediction of Rainfall Extremes Campaign in the Pacific (PRECIP) which has adopted the intensity and duration framework as a guiding principle (PRECIP 2022). Each campaign seeks to better understand extreme rainfall in the context of Taiwan.

One reason for multiple campaigns focused on Taiwan is highlighted through a limitation of the intensity and duration framework. Studying the intensity and duration of rainfall requires guaranteed rainfall. While the floods in Colorado may have been ideal for study, storms of that caliber are not always guaranteed during a season. Taiwan, on the other hand, is almost guaranteed to receive rainfall during the warm season as seen during the TiMREX field campaign, though locally, Taiwan splits the warm season into the Mei-yu season that runs from mid-May to the end of June and the typhoon season that runs from July to September. In a climatology of rainfall from Henny et al. (2021), it was found that while the peak daily rainfall average was found in the typhoon season, the 20-day running average daily rainfall was found in the Mei-yu season with a value of 12.5 mm/day over the entirety of Taiwan (Fig. 1.3).

1.3 The Mei-yu

Translated from mandarin, Mei-yu means “plum rain” based on the seasonal ripening of plums near the Yangtze River in China that are often soaked in rain as they fall (Allen et al. 2015). Although first named in China, this season extends to much of East Asia with other names for it being the Baiu/Tsuyu in Japan and the Changma/Jangma in Korea. The Mei-yu signifies a transitional period of the waning wintertime northeast monsoon

and strengthening summertime southwest monsoon (Chen 1992). The southwest monsoon is relatively warm and transports moisture from the equator to the Bay of Bengal and then to Taiwan and the rest of East Asia (Chang and Chen 1995). The monsoonal flow is typically southwesterly as a result. Opposite of the southwest monsoon is the northeast monsoon dominated by relatively drier and cold northeasterly flow originating from the Siberian high-pressure system (Jhun and Lee 2004).

The boundary between these two monsoons forms the Mei-yu front, a quasi-stationary moisture front which is the predominant source of rainfall during the Mei-yu season (Chen 1992). Although temperature gradients might be appreciable while the front is over China, once the front passes south of the Chinese coastline into the Taiwan Strait, the warm waters act to weaken the temperature gradients (Chen 1992; Chen et al. 2007). Upon entering Taiwan, the dominant forms of Mei-yu frontogenesis become convergence and deformation while baroclinic terms become negligible or frontolytic (Chen et al. 2007). This convergence and deformation stems from a wind shift line spanning from the surface to 1 km height along the leading edge (Chen 1992; Chen and Hui 1990; Chen et al. 1989; Trier et al. 1990). A cross section through a Mei-yu front from Ke et al. (2019) using multi-Doppler synthesis from Taiwan's operational radar network reveals that the prefrontal southwesterlies rise over the postfrontal northeasterlies to produce intense rainfall along the front with more stratiform rainfall to the north of the front (Fig. 1.4).

Multiple mechanisms enhance rainfall associated with Mei-yu fronts including mesoscale convective systems, or MCS, that form and propagate along the Mei-yu front (Zhang et al. 2000; Houze 2004), as well as low-level jets (LLJ) that enhance moisture transport and frontal convergence. The three low-level jets that play the largest role in Mei-yu front rainfall are the synoptic low-level jet (SLLJ), marine boundary layer jet (MBLJ), and the barrier jet (BJ). The SLLJ was extensively explored during TAMEX and TiMREX and is often found between 900-600 hPa to the south of the Mei-yu front (Chen et al. 2022). As the frontal cyclone deepens, the SLLJ develops through the Coriolis force acting on cross-contour ageostrophic winds (Chen et al. 2022; Chen et al. 1997). The MBLJ is

often found near 925 hPa over water to the south of the Mei-yu front (Chen et al. 2022). Formation of the MBLJ is like the SLLJ with sub-synoptic pressure gradients aligning cross-contour ageostrophic winds toward the Mei-yu trough (Chen et al. 2022, Tu et al. 2019). The barrier jet is an orographically induced jet found at 1 km ASL near Taiwan (Chen et al. 2022). These jets are most common in the prefrontal sector of Mei-yu fronts as southwesterly flow collides with the CMR, orographically deforms, and then converges with the southwesterly flow downstream near northwestern Taiwan (Fig. 1.5) (Chen et al. 2022; Li and Chen 1998). Unlike the SLLJ and MBLJ, the barrier jet is not necessarily formed through pressure gradients associated with the Mei-yu trough. They can, however, still interact with the front as seen in Fig. 1.6 where a barrier jet collides with a cold pool ahead of a Mei-yu front, slowing the progression of the front (Ke et al. 2019).The interaction of the barrier jet with the Mei-yu front was a focal point of the TAMEX field campaign, with implications for densely populated regions of Taipei Basin.

Another way in which orographic modification of the Mei-yu front occurs is the splitting of the front upon approach toward the SMR (Chen 1992). This splitting produces a windward front that resides west of the CMR and a leeside front that resides east of the CMR, each propagating south with the windward front being the most extreme from a rainfall perspective (Chen et al. 1992). In a climatology from Wang et al. (2012) of average 6-hour rain accumulation distribution relative to windward Mei-yu front placement, rainfall was found to be linked not only to front placement, but also topography (Fig. 1.7). Frontal placement, however, was set at the western coastline as it is difficult to pinpoint the Mei-yu front on land. Therefore, as to how the fronts are modified by orography as they propagate south over land through the mountainous island is still an active research topic.

1.4 Research Objectives

A Mei-yu front case that produced extreme rainfall throughout Taiwan occurred between 1-3 June 2017. This Mei-yu front made landfall in northern Taiwan producing intense

rainfall over Taipei Basin before propagating south into central Taiwan where rainfall persisted on the windward slopes of the CMR for the entirety of the observation period. Prior studies on this event have already determined there to be orographic modification to rainfall associated with the Mei-yu front in northern Taiwan with an active barrier jet found in the prefrontal sector of the front (Tu et al. 2022; Chen 2022), yet there is still more to explore with regards to the intensity and duration of rainfall relative to the topography.

This study will expand on prior works to better understand how orography modified the location, intensity, and duration of rainfall associated with the 1-3 June 2017 Mei-yu front. To address this broader goal, the specific science objectives are to:

1. Determine how the orography modified the Mei-yu front, comparing the more studied interactions in northern Taiwan with the less defined interactions in central Taiwan.

2. Understand the impact of this frontal modification on rainfall intensity, duration, and location.

3. Compare orographically modified rainfall in northern versus central Taiwan.

Section 2 will discuss the data and methods employed in this study to isolate topographic influences on rainfall during this extreme rainfall event. Section 3 will provide an overview of the 1-3 June 2017 Mei-yu front case. Section 4 describes results for both northern and central Taiwan. Section 5 will provide a discussion of the results and section 6 will include conclusions of this study as well as plans to continue this work in the future.

1.5 Figures

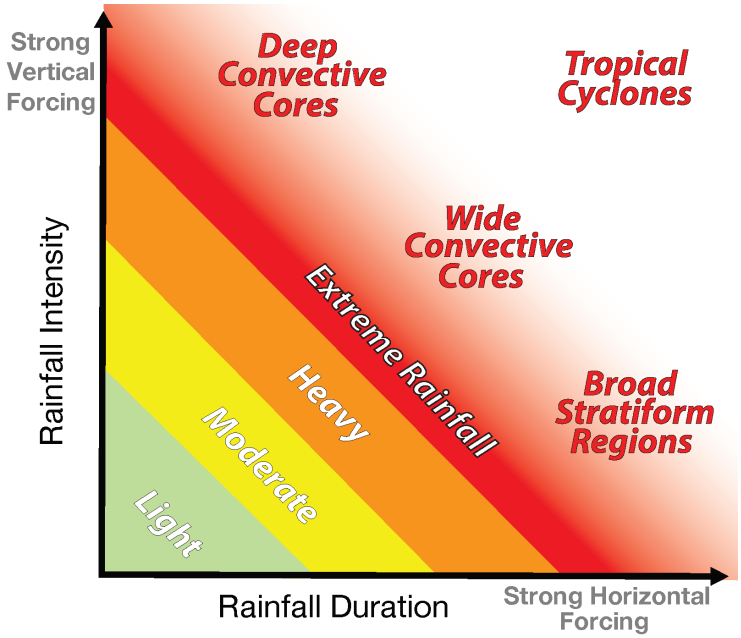

Figure 1.1: Rainfall intensity and duration framework (PRECIP 2022).

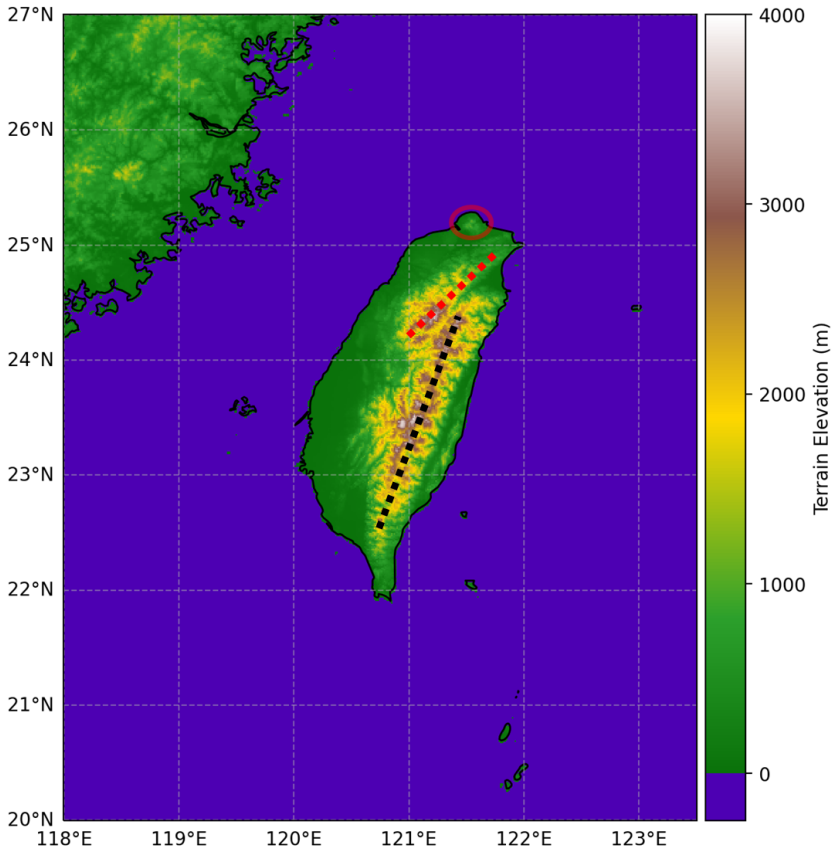

Figure 1.2: Terrain elevation map of Taiwan. The dashed black line indicates the Central Mountain Range and the dashed red line indicates the Snow Mountain Range. The red circle indicates the location of the Yangmingshan National Park.

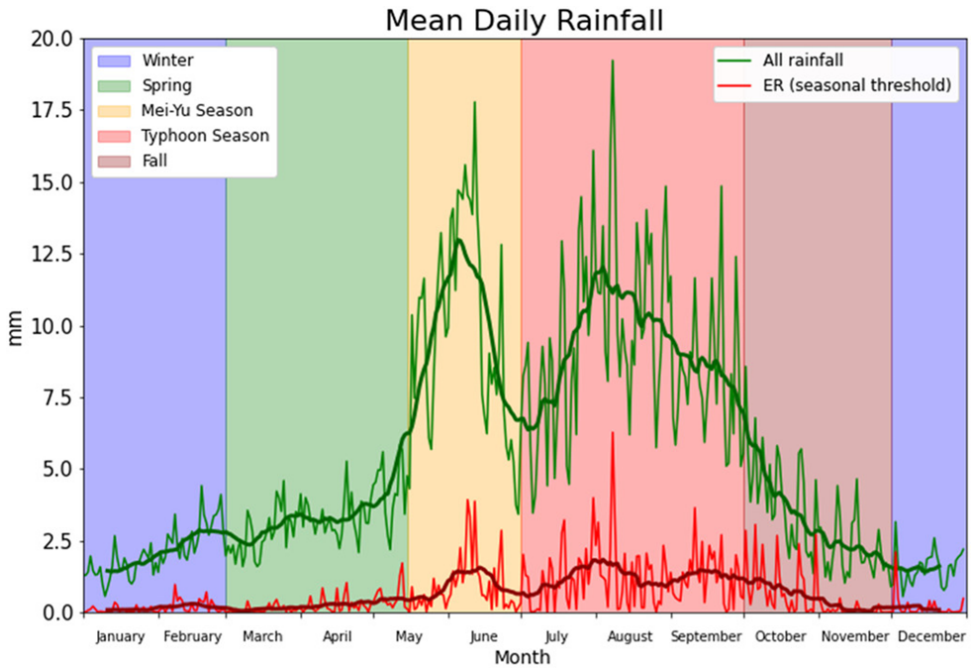

Figure 1.3: The mean total (green) and extreme (red) rainfall for each day of the year, with color-coded seasons. The Taiwan Climate Change Projection Information and Adaptation Knowledge Platform rain data are averaged spatially. The thick lines denote 20-day running means. ER is defined based on a spatially and seasonally varying 99th-percentile threshold so as not to eliminate cold-season extreme events. From Henny et al. (2021).

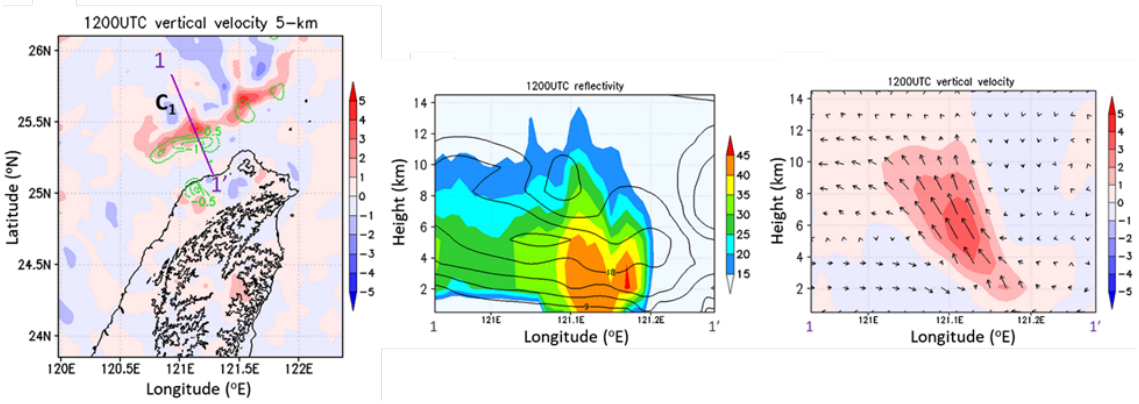

Figure 1.4: Retrieved result at 1200 UTC 11 June 2012: (a) vertical velocity (colour shaded, unit: m s^{-1}) at 5 km and convergence area (green contour, interval is 0.5 $\times$ 10^{-3} s^{-1}) at 1 km; (b) vertical cross-section of radar reflectivity (color shaded, unit: dBZ) and the horizontal wind speed (contour lines); (c) cross-section of vertical wind (colour shaded, unit: m s^{-1}) and wind vector relative to the system motion. Adapted from Ke et al. (2019).

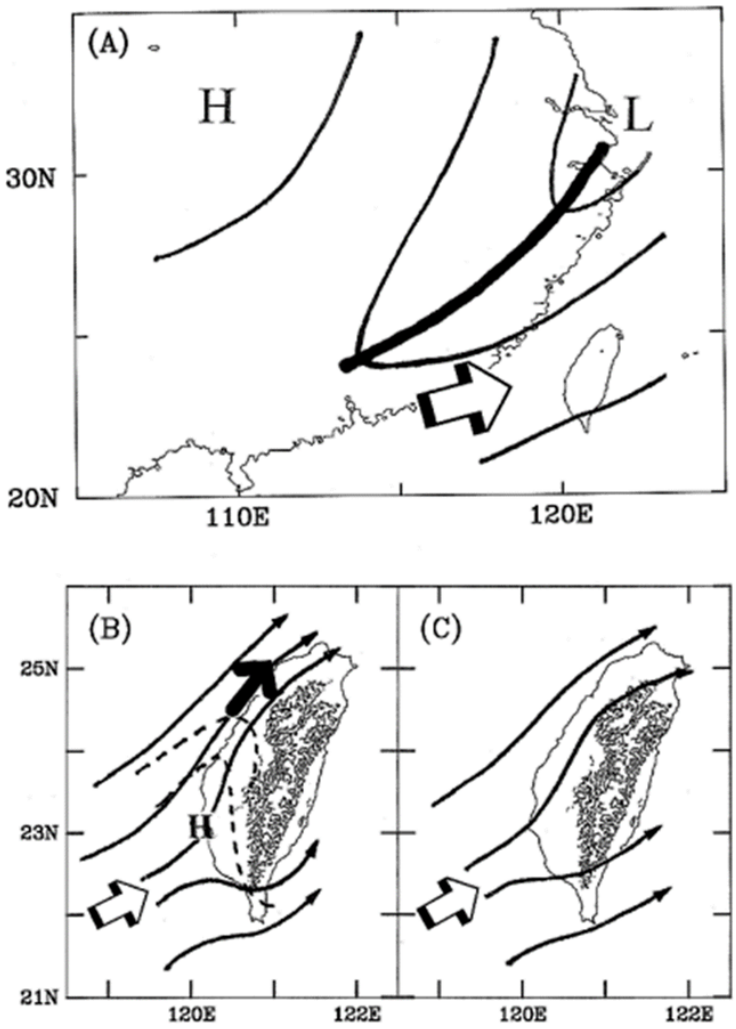

Figure 1.5: A schematic diagram for the barrier jet formation. (a) The large-scale low-level flow pattern, (b) the mesoscale airflow near the 1-km level, and at (c) 2.5-km level over the Taiwan area are shown. The heavy line, open arrow, and heavy arrow represent the low-level pressure trough, upstream southwesterly flow, and barrier jet, respectively. The distribution for the geopotential height in (a), local sea level pressure pattern (dashed) in (b) and streamlines (solid) in (b) and (c) are also shown. Adapted from Li and Chen (1998).

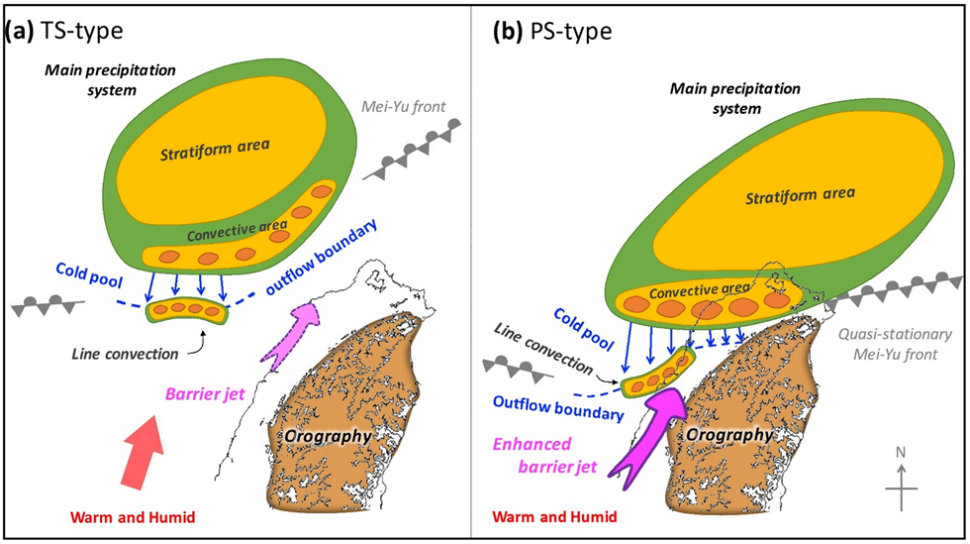

Figure 1.6: Schematic diagrams to demonstrate the mechanism of the extremely heavy rainfall event. (a) Prefrontal convection forms a trailing stratiform type precipitation over the ocean, and the line convection is triggered due the cold outflow encountering a warm and humid southwesterly flow; (b) the strengthened cold pool and enhanced barrier jet repeatedly triggered the Y-shaped echo line convection, then merge with the main convection to form a PS-type precipitation over northern Taiwan. The location of the Mei-yu front and the warm/humid southwesterly flow (red arrow) illustrate the environmental condition of the synoptic scale over Taiwan. The location of the cold pool and the orography in northern Taiwan blocks the displacement of the main convection. From Ke et al. (2019).

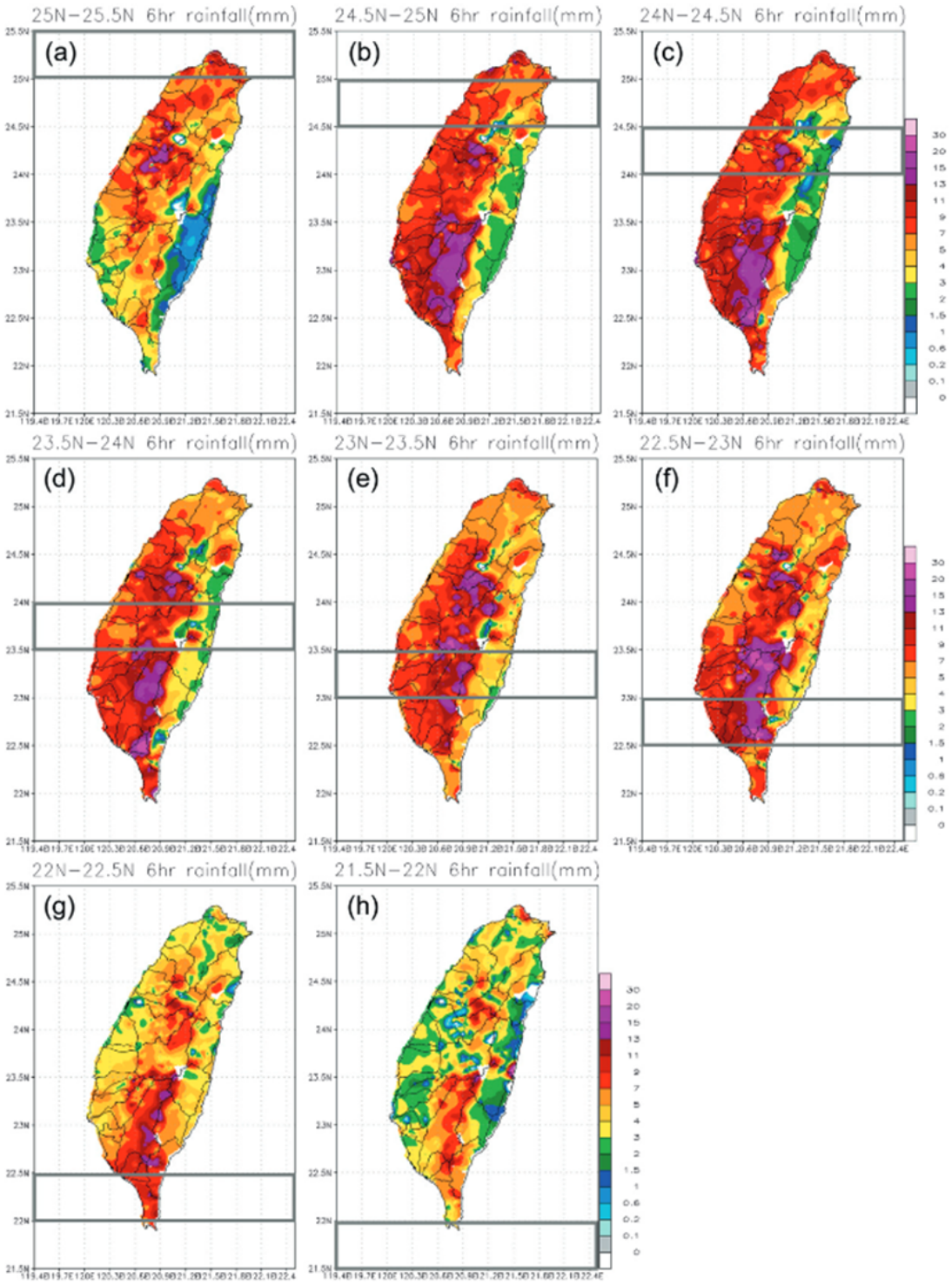

Figure 1.7: The averaged 6-h rainfall distribution (mm, scale on right) over Taiwan during May–June 1991–2006 when the surface Mei-yu front is within each 0.5°-latitude interval (as marked by gray box) from (a) 25°–25.5° to (h)21.5°–22°N (north to south). From Wang et al. (2012).

Chapter 2

Data and Methods

2.1 Case Overview

The European Centre for Medium-Range Weather Forecasts (ECMWF) Reanalysis v5 (ERA5) was used to provide the synoptic and mesoscale contextualization of this case study. ERA5 is an atmospheric reanalysis dataset produced by the Copernicus Climate Change Service at ECMWF on a 0.25° latitude-longitude grid at 1-hr time intervals. Data from 1200 UTC 1, 2, and 3, June 2017 was accessed using the National Center for Atmospheric Research (NCAR) – Research Data Archive (European Centre for Medium-Range Weather Forecasts 2019). On the synoptic scale, zonal wind speed, meridional wind speed, geopotential height, relative vorticity, and specific humidity at 300 hPa, 500 hPa, and 850 hPa were obtained from ERA5. ERA5 mean sea level pressure and 925 hPa equivalent potential temperature (θ_e), zonal wind speed, and meridional wind speed were obtained for a mesoscale analysis of this event.

Observational datasets provided by the Central Weather Bureau of Taiwan (CWB) include radiosondes and operational radar data. The radiosonde data was from CWB's Taipei launch station (121.52°E, 25.04°N) for 1200 UTC 1 June 2017, 0000 UTC 2 June 2017, and 1200 UTC 2 June 2017. The data was used to create Skew-T diagrams using MetPy (May et al. 2022) to provide vertical profiling of environmental conditions for the event. The operational radar network of Taiwan consists of 12 radars, 4 S-band radars and

8 C-band radars (Fig. 2.1). To track movement of the front close to Taiwan using radar reflectivity, data from the S-band Radar Code of Wu-Fenshan (RCWF) radar (121.77°E, 25.07°N) and Radar Code of Chigu (RCCG) radar (120.09°E, 23.15°N) were used. Raw RCWF and RCCG files first had to be converted into CfRadial format (Dixon et al. 2016) using the Lidar Radar Open Software Environment – "Topaz" (Bell 2022). Once converted, data was plotted using the Python ARM Radar Toolkit (Helmus and Collis 2016).

Data from the Himawari-8 geostationary weather satellite operated by the Japanese Meteorological Agency was used to track the horizontal and vertical extent of the Mei-yu frontal system beyond Taiwan's operational borders. The 10-minute level-1 full-disk gridded product used in this study was by the P-Tree System, Japan Aerospace Exploration Agency. Channels 1, 2, and 3 reflectance was used to create corrected true color imagery (LoneSky 2020) and channel 10 brightness temperature was used for low-level water vapor inferences.

2.2 Quantitative Precipitation Estimation and Segregation Using Multiple Sensors (QPESUMS) System

The QPESUMS system is a 10-minute frequency rain gauge corrected rain rate and rainfall accumulation product produced by the CWB (Chang et al. 2021). The system integrates reflectivity-inferred rain rates from 12 operational radars (Fig. 2.1) to create a gridded rain rate product which is corrected using the 1000+ rain gauges on the island. A flowchart of the operational QPESUMS system is shown in Figure 2.2. The 1-hour accumulation precipitation product with 0.0125° x 0.0125° resolution spanning 120° - 123.5° E and 20° – 27° N was used for its coverage, accuracy over Taiwan, and ability to quantify rainfall within rain bands associated with the Mei-yu front. An accompanying terrain elevation dataset provided by CWB with similar resolution and horizontal extent as the 1-hour accumulation QPESUMS product was also used for topographical subdivision of rainfall accumulation.

2.3 Intensity and Duration Framework

To translate the Doswell et al. (1996) intensity and duration framework into a methodology for categorizing extreme rainfall using the QPESUMS dataset, the following method was used:

1. For a given grid point, build a time series of 1-hour rainfall accumulation over a 48-hour window.

2. Define rain periods within the 48-hour period where minimum rainfall for any hour is at least 0.25 mm. The 0.25 mm criteria is based on QPESUMS minimum detectable rainfall of 0.25 mm. To account for pauses in continuous rainfall that might be the result of slight shifts in rainfall location, consecutive rain periods with gaps in rainfall of 1 hour are combined into one rain period.

3. Each rain period has a total accumulation of rainfall and a contiguous duration which can both be used to define an average rain rate in mm/hr. The contiguous duration and average rain rate act as proxies for the duration and intensity ingredients as part of Doswell et al. (1996).

The reasoning behind the 1-hour gap allowance is seen in Figure 2.3. Figure 2.3a-d shows the results of placing all rain periods over land using the QPESUMS dataset onto a duration and rain rate grid. Four different methods of defining duration were tested: noncontiguous duration where any time gap is allowed, contiguous duration with no gap allowance, contiguous duration with 1-hour gap allowance, and contiguous duration with 2-hour gap allowance. The choice to use 1-hour gap allowance was made as it best fits the objectives of this study. Noncontiguous duration strongly diluted the maximum average rain rate achievable and resulted in too few rain periods. No gap allowance results in far too many rain periods that if this data is broken up into terrain height bins (e.g., 1500 – 2000 m in Fig. 2.3e-g), the relative density remains is focused towards low rain rates and durations with little spread. Contiguous duration with 2-hour gap allowance begins

to dilute high rain rate rain periods. The 2-hour gap is also a long period of no rainfall and begins to lose physical meaning. For example, if a rain period is found within a single convective cell, a 2-hour gap in rainfall is more likely to be caused by a second source of rainfall rather than the original convective cell moving back over the same grid point. For these reasons, the 1-hour gap allowance strikes a balance between number of rain periods, physical meaning, and dilution of high rain rates. For the remainder of this study, all instances of duration and intensity will be in the context of contiguous 1-hour gap allowed duration and average rain rate.

2.4 Weather Research and Forecasting (WRF) Model

The WRF model is a nonlinear, non-hydrostatic, full physics numerical weather prediction model developed by members of NCAR, NWS, and the meteorological community. For this study, version 4.1.3 is used (Skamarock et al. 2019). Parameterization schemes used can be found in Table 1.

The model was initially run with 40 ensemble members using two nested grids, each with 50 vertical levels, and an inner and outermost grid resolution of 3-km and 9-km, respectively (Fig. 2.4). The model was initialized using model data from the Global Forecast System. These members were run from 1200 UTC 1 June 2017 to 1200 UTC 3 June 2017 with 12-hour timesteps for the outermost grid and 3-hour timesteps for the innermost grid .

Once an ensemble member was found that most resembled the observations for this event with regards to timing and accumulation of rainfall, the NDOWN program was used on that member to downscale a third, innermost grid with horizontal resolution of 1 km and 15-minute timesteps (Fig. 2.4). The reasoning for this third grid is that mesoscale features related to the complex terrain would not be resolved on a 3-km grid with duration shorter than a 3-hour window. As a test of orographic influence for this study, the NDOWN program was repeated using the same 1-km resolution and 15-minute timestep, but with halved terrain for the innermost grid only. The gradient in Taiwan's terrain height is

large compared to much of the world with mountain peaks near 4 km height a short distance away from the coastline. By placing this event in a halved terrain environment, the results are more applicable to regions with more gradual and shallow topography. Since this study focuses on changes in rainfall associated with changes in topography, only results from this innermost grid will be considered. These 1-km resolution model runs will hereafter be labeled Control and Half-T. All analysis of WRF data was done using MetPy (May et al. 2022) and WRF-Python (Ladwig 2017).

2.5 Read/Interpolate/Plot (RIP) v4.7

RIP is a Fortran program produced by NCAR for the purpose of post-processing WRF and NCAR Mesoscale Model v5 data. The trajectory analysis function of RIP was used for this study. RIP is capable of releasing trajectories forward and backward in time in sub-grid scale coordinates and output diagnostic variables in sub-timestep intervals. The strength of RIP over other trajectory analysis programs is its high efficiency in processing WRF data and ability to produce large numbers of trajectories in short amounts of time.

2.6 Figures and Tables

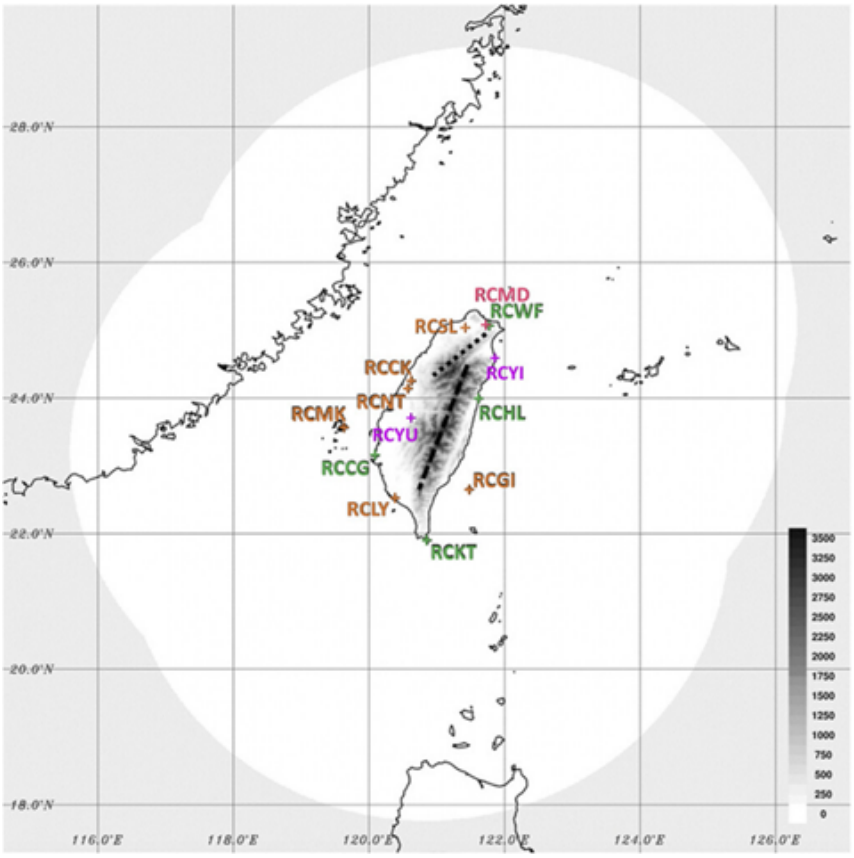

Figure 2.1: The weather radar network in Taiwan. Green and orange plus symbols and four-letter identifiers (IDs) indicate the operational S- and C-band radars, respectively. RCYU and RCYI are C-pol radars that have not been deployed as of July 2020 and RCMD is a special C-pol radar collocated with RCWF for the calibration, training, and scan strategy design of the C-pol radars. The white region shows the maximum range of the radar coverage and gray shades the ground elevation. The black dotted line indicates the Snow Mountain Range and the dashed line the Central Mountain Range. From Chang et al. (2021).

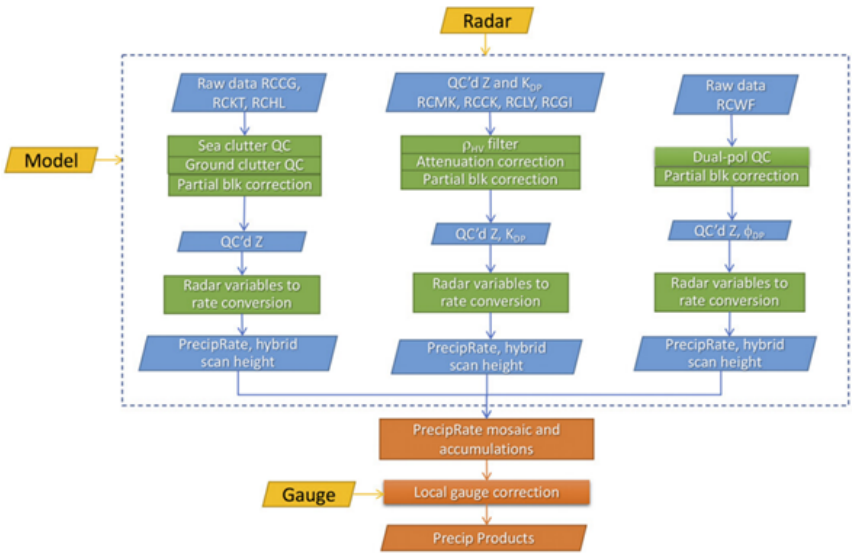

Figure 2.2: An overview flowchart of the Taiwan QPESUMS system. From Chang et al. (2021).

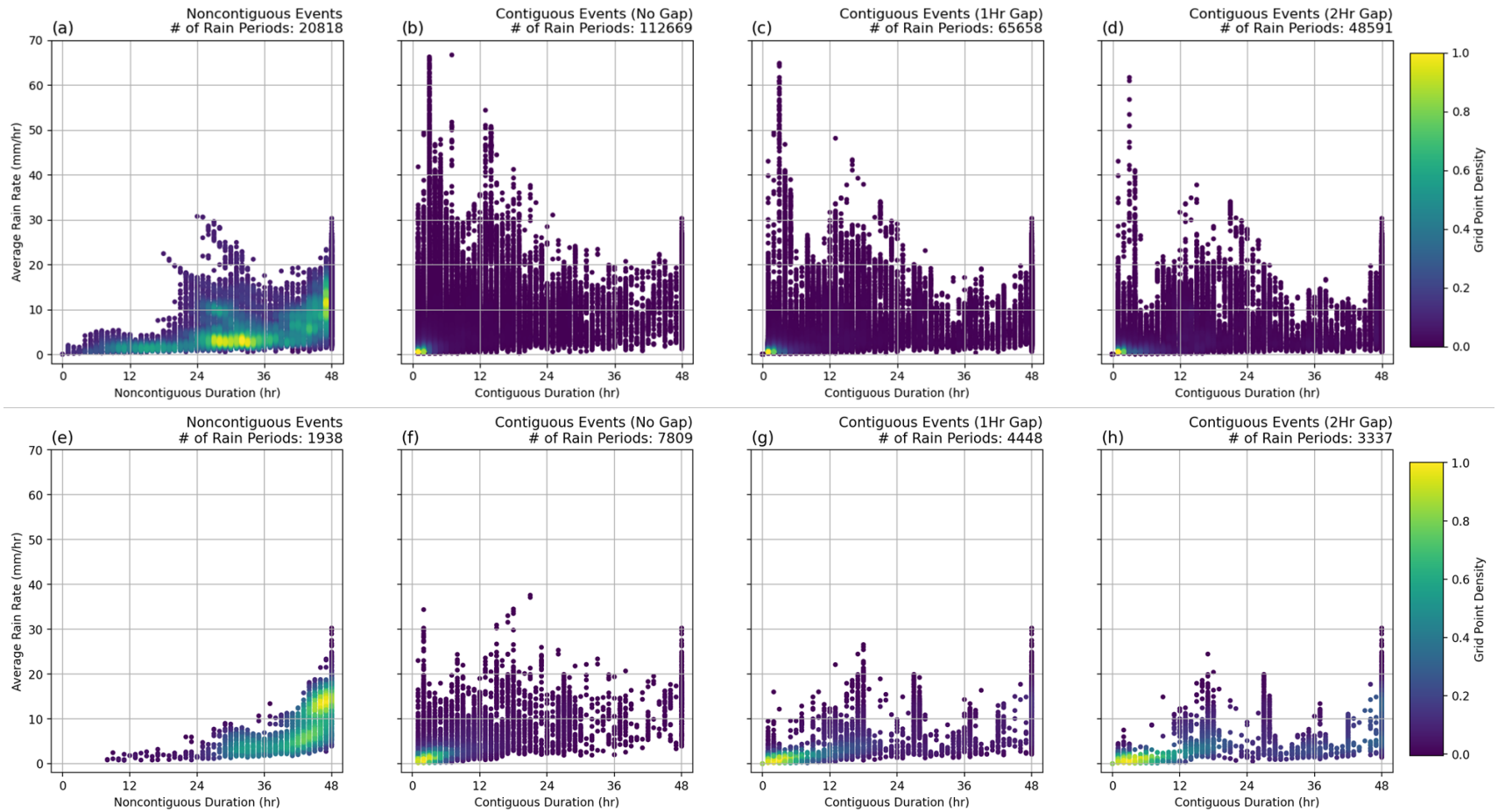

Figure 2.3: Intensity and duration scatterplots for all QPESUMS rain periods (a-d) over land and (e-g) between 1500 – 2000 m terrain height, with different methods of defining duration. The durations are defined as (a, e) noncontiguous duration, (b, f) contiguous duration with no allowance for gaps in rainfall, (c, g) contiguous duration with 1-hour gap allowance in rainfall, and (d, g) contiguous duration with 2-hour gap allowance in rainfall. Coloring is based on relative density of points.

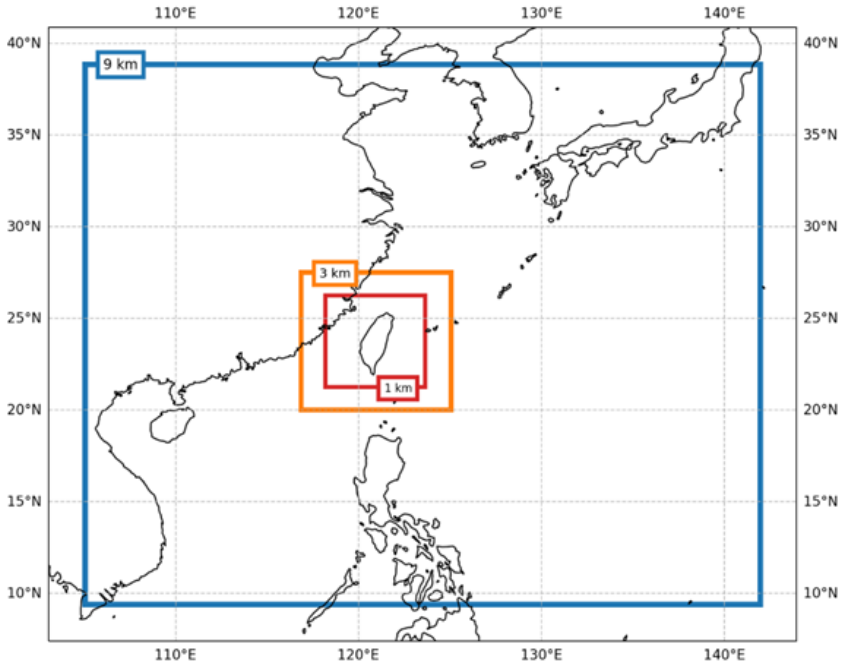

Figure 2.4: Horizontal extent of the three WRF domains. The blue, orange, and red boxes represent the 9, 3, and 1 km grids, respectively.

Table 2.1: Parameterization schemes used in WRF model.

Microphysics	Aerosol-aware Thompson Microphysics (Thompson and Eidhammer 2014)
Longwave and Shortwave Radiation	Rapid Radiative Transfer Model for General Circulation Models (Iacono et al. 2008)
Surface Layer	Monin-Obukhov Surface Layer Scheme (Janić 2001)
Land Surface Interaction	Unified Noah Land Surface Model (Tewari et al. 2004)
Boundary Layer	Yonsei University Boundary Layer Scheme (Hong et al. 2006)

Chapter 3

Case Overview

3.1 Prior to Mei-yu Landfall

Mei-yu fronts are an impactful weather phenomenon that frequently occur in Taiwan, leading to forecasters at CWB employing a checklist to determine when to issue elevated warnings for front-associated extreme rainfall (Table 3.1) (Wang et al. 2012). The checklist involves multiple categories ranging from near-surface to synoptic-scale conditions, each with their own set of objective and subjective criteria. Should any 14 of the 20 criteria be met, CWB will begin to issue warnings for an impending Mei-yu front. Leading up to the landfall of the 1-3 June 2017 Mei-yu front, many of these criteria were met to issue rainfall warnings in advance (Wang et al. 2022).

Synoptically, Taiwan was situated in the right entrance region of a 300 hPa jet streak, a common indicator of synoptic scale lift at 1200 UTC 1 June 2017 (Fig. 3.1a). An upper-level low pressure system is vertically stacked between the 300 hPa (Fig. 3.1a) and 500 hPa (Fig. 3.1b) levels just north of the Korean peninsula in Siberia with the 850 hPa low pressure system situated downstream of the upper-level trough in the Sea of Japan (Fig. 3.1c). To the southeast of these low-pressure systems sits the subtropical anticyclone found at both 500 hPa and 850 hPa, a common feature for Mei-yu front formation (Zhao et al. 2004). With both the Siberian low-pressure system and subtropical high-pressure system situated downstream of Taiwan at 850 hPa, a SLLJ (Chen et al. 2022) forms producing

monsoonal southwesterly flow extending from the Indochinese peninsula to the central Pacific. The Mei-yu trough that often extends from the Siberian low-pressure system and denotes the Mei-yu front is missing in this case. Nevertheless, a horizontal wind shift at 850 hPa north of the SLLJ in central China indicates the front is just north of Taiwan (Fig. 3.1c).

With the ensuing front just north of Taiwan, the monsoonal flow has already contributed to precipitation in Taiwan. Himawari-8 True Color imagery at 0000 UTC 1 June 2017 (Fig. 3.2a) and channel 10 IR brightness temperatures at 1200 UTC 1 June 2017 (Fig. 3.3a) indicate clouds ahead of the Mei-yu rain band with strong correlation to topography (Fig. 1.2). As those moist monsoonal southwesterly winds encounter the steep topography, orographic lift forces adiabatic cooling to form condensation which rains out over the high terrain and lee side of the CMR. Near the surface at 925 hPa (Fig. 3.4a), southwesterly flow is seen encountering the steep terrain of southwestern Taiwan and orographically deforming into southerlies in northern Taiwan. The lack of a sharp equivalent potential temperature gradient and wind shift near Taiwan at 1200 UTC 1 June 2017 indicates that Taiwan is still in the prefrontal environment. Mean sea level pressure is at a minimum of 1001 hPa to the northwest of Taiwan, fulfilling another criteria of the CWB forecasting checklist (Table 2.1). A radiosonde launched in Taipei basin at 1200 UTC 1 June 2017 shows an unstable profile with plenty of moisture in this prefrontal environment (Fig. 3.5a). Approximately 1000 J/kg of convective available potential energy (CAPE) and 30 J/kg of convective inhibition (CIN) indicates an environment primed for convection. The precipitable water of 67.3 mm highlights the potential for extreme rainfall. For context, a climatology of GPS precipitable water found that the average precipitable water vapor for Taiwan during the Mei-yu season was approximately 50 mm (Lien et al. 2022). A slightly veering wind profile from the surface to 500 hPa indicates warm air advection consistent with synoptic scale, prefrontal monsoonal flow.

Previous studies also have found external factors that made this event anomalously strong. Arakane et al. (2019) noted a strengthening of both postfrontal and prefrontal

wind speeds along with enhanced low-level moisture transport to Taiwan due to the influence of tropical cyclone Mora which formed in the Bay of Bengal on 28 May 2017 and dissipated on 31 May 2017. The strengthening of prefrontal and postfrontal winds acted together to strengthen the frontal system while the enhanced low-level moisture transport strengthened precipitation. Tu et al. (2020) also found that the bulk of moisture transport was found within the marine boundary layer and carried through an enhanced marine boundary layer jet. The presence of both the MBLJ and SLLJ acted in tandem to strengthen moisture transport and frontal trough development.

3.2 Landfall in Northern Taiwan

The Mei-yu front makes landfall on the northern coast of Taiwan at 0000 UTC 2 June 2017 (Fig. 3.6a). The associated rain band is quasi-zonal extending at least $\pm 2^\circ$ longitude from Taiwan. The leading edge of the rain band has reflectivity values as high as 60 dBZ indicative of heavy rainfall. Trailing behind the leading edge of the front is a broader stratiform region with reflectivity values around 30 dBZ. Using True Color imagery from Himawari-8, the entirety of the island is engulfed in clouds with additional deep clouds south of the Mei-yu front extending upstream of the topography off the southwestern coast parallel to the prefrontal southwest flow (Fig. 3.2b). The satellite imagery shows that the linear cloud structure associated with the Mei-yu front extends far beyond Taiwan with an approximate longitudinal extent of 105° E to 135° E. A sounding taken in Taipei at 0000 UTC 2 June 2017 reveals an enhanced moisture profile compared to 12 hours prior with precipitable water of 74.2 mm coincident with enhanced low level moisture convergence along the nearby front (Fig. 3.5b). Mid to low level (800 hPa – 700 hPa) wind speeds have increased by approximately 15-20 knots in 12 hours, but surface winds have weakened with the passing of the front.

It takes 6 hours for the Mei-yu front to pass Taipei and move south toward the CMR (Fig. 3.6b,c). The leading edge of the front is near zonal on the western coastline, but tilts southwest to northeast on the eastern coastline. This tilt lags the front on the

eastern coastline relative to the front on the western coastline, a trend that becomes more prominent as time progresses from 0300 UTC to 0600 UTC. The trailing stratiform precipitation behind the leading edge of the Mei-yu front decreases in area but persists downstream and parallel to the tilted eastern leading edge of the eastern coastline. Despite the front progressing further south, the stratiform cloud shield remains extended far north beyond the coastline (Fig. 3.2c).

3.3 Central Taiwan

At 1200 UTC 2 June 2017, the Mei-yu rain band has moved farther south (Fig. 3.7a). A more exaggerated north-south tilt in the leading edge is seen with the rain band not reaching into the higher terrain. Unlike 6 hours prior, the trailing stratiform rainfall reappears behind the leading edge of intense convection. Disconnected from the convection associated with the front, there are zonal bands of isolated convection along the windward slopes of the CMR that are indicative of rainfall produced by prefrontal flow impinging on steep topography. Himawari-8 channel 10 shows this deep convection associated with the rain band and trailing stratiform region and weaker leeside convection not seen in the ground-based radar data due to blocking by the CMR(Fig. 3.3b). The 925 hPa equivalent potential temperature and wind barbs from ERA5 (Fig. 3.4c) poorly represent frontal placement with it being approximately one full degree north of the rain band captured on radar. If we consider the equivalent potential temperature gradient to be accurate, there is an approximate 20 K difference across the front, far larger than fronts observed during TAMEX (Hor et al. 1998). Another sounding from Taipei at 1200 UTC 2 June 2017 reveals weak near-surface flow and a return to pre-landfall precipitable water (Fig. 3.4c). CAPE has diminished from 24 hours prior indicating northern Taiwan is unlikely to receive additional intense precipitation.

By 1800 UTC 2 June 2017, the rain band on the western coast returns to quasi-zonal orientation, but has not proceeded farther south relative to 6 hours prior (Fig. 3.7b). Convection south of the rain band on the windward slopes continues. With the lack of a

defined leading edge of intense convection near the terrain, there is also a lack of trailing stratiform rainfall. The front has become stationary with convection forming upstream in the South China Sea (SCS) and being advected downstream into the terrain. Channel 10 from Himawari-8 shows that much of the convection upstream of Taiwan has died out with small cells forming in the South China Sea and the deepest convection forming close to the Taiwanese west coast (Fig. 3.3c). By 0000 UTC 3 June 2017, the rain band begins to lose linear continuity with a short rain band extending from the high terrain to the coastline with a gap to another rain band off the coastline indicating the end of the event and the regression of the front northward (Fig. 3.7c).

3.4 Rainfall Accumulation

The period of analysis for this study will be focused between 1200 UTC 1 June 2017 to 1200 UTC 3 June 2017, capturing prefrontal periods, landfall of the front at 0000 UTC 2 June,the quasi-stationary nature of the front over central Taiwan, and the northward receding of the front at 0000 UTC 3 June. To account for strong orographic precipitation not associated with the front, the 12 hours prior and after the front are included to fill out the intensity-duration spectrum in this analysis. Within that 48-hour period, maximum rainfall accumulation neared 1500 mm in the CMR (Fig. 3.8a). Noticeable bands of high precipitation are collocated with the initial landfall of the front on the northern coastline and where the front became stationary in central Taiwan. Although not associated with these bands, there are multiple regions with 500+ mm rainfall on the windward slopes of the SMR and CMR hinting at the prominence of orographic precipitation induced by the monsoonal southwest flow not associated with the front.

To understand the temporal progression of the front associated rainfall, a Hovmöller diagram of 1-hour rainfall accumulation from A to A' in Fig. 3.7c is shown in Fig. 3.9a. Intense rainfall begins in Taipei just before 0600 UTC 2 June 2017 and reaches its southernmost extent of 23.25°N at 1800 UTC 2 June 2017. The rain band is stationary between 23.25°N and 23.5°N for approximately 6 hours then recedes north at 0000 UTC 3 June

2017. Although intense rainfall in northern Taiwan is only associated with the Mei-yu front, there are multiple regions where rainfall is persistent throughout the entire 48-hour period such as 23.5°N indicative of conditions favorable for orographic precipitation independent of the Mei-yu front.

3.5 Forecasts

This extreme Mei-yu rainfall event was a forecasting challenge for numerical weather prediction models and human forecasters. While many of the CWB's criteria for extreme Mei-yu rainfall were fulfilled leading up to this event, rainfall accumulation totals were severely under predicted. Figure 10 was provided by the CWB and shows the forecasted rainfall accumulation from the WRF Ensemble Prediction System (WEPS) mean and ECMWF compared to QPESUMS for 2 June 2017 using multiple model initialization times. The WEPS system with a grid spacing of 15 km is used operationally by the CWB and is a mesoscale ensemble centered on Taiwan with parameterizations chosen to best model Mei-yu and typhoon events near Taiwan (Li et al. 2020). The locations of maximum rainfall on land are similar between models and QPESUMS, but the stationary rain band in central Taiwan is missing in all model outputs and rainfall accumulation totals are severely underrepresented in the models. The maximum 24-hour rainfall from all the models were approximately 250 mm whereas QPESUMS recorded just over 1000 mm. Total water is a measure of total precipitation over the entire QPESUMS domain. All models under predicted total water by a factor of $1.5 - 2$ times compared with QPESUMS, with a more concerning notion that model runs initialized closer to analysis time predicted less rainfall than model runs initialized 12 hours prior.

To contextualize this event, CWB uses a broader system for issuing rainfall warnings outside of Mei-yu fronts (Table 3.2). If QPESUMS was treated as the forecasted rainfall accumulation, the maximum potential warning between 1200 UTC 1 June 2017 and 1200 UTC 3 June 2017 are seen in Figure 3.11a. Should WEPS and ECMWF be the forecasts that CWB followed for issuing warnings, all torrential and extremely torrential warnings

would be missed since these forecasts only have maximum rainfall near 250 mm. What is more is that the criteria for extremely torrential is 500 mm in 24 hours while the maximum accumulation for 2 June 2017 was double that near 1000 mm.

3.6 WRF Control

While the forecast models did not perform well in replicating the rainfall, the 1-km resolution WRF Control run did better (Fig. 3.8b). A key feature of this event, the Mei-yu rain band extending off the western coast, was missing in the forecast models, but was well replicated in the WRF model. The Control run did have a few differences from QPESUMS, however. The rain band was shifted north approximately a quarter of a degree in latitude, the location of rain maximum in northern Taiwan is moved farther inland, and the Control run lacks the heavier leeside precipitation east of the CMR. A Hovmöller diagram of precipitation also highlights that the timing of the Mei-yu rain band is different from QPESUMS, with the front becoming quasi-stationary briefly in central Taiwan before progressing south, as well as missing the receding portion of this event (Fig. 3.9b).

In determining if the model replicated intensity and duration well, Figure 3.12 uses the same methodology as Figure 2.3, but expanding to Control and Half-T for multiple terrain elevation bins. The choice of bin sizes was meant to encapsulate low, medium, and high terrain relative to the maximum height in observations, Control, and Half-T. In comparing the lower terrain bin (0-500 m), the Control run performs well in replicating the tapering intensity with increasing duration as well as a secondary maximum in intensity near 12-hr duration (Fig. 3.12a, d). It could not capture the low duration, high intensity rainfall found in QPESUMS. The medium terrain bin (500-2000 m) is also simulated well in the Control with a drop off in low duration, high intensity rainfall and an increase in the intensity of maximum duration rainfall (Fig. 3.12b, e). The high terrain bin (2000-4000 m) is not perfectly captured with QPESUMS having a maximum in intensity between 12-24 hours, while Control generally increases in intensity with increasing duration (Fig. 3.12c, f). That being said, the spread in density to higher durations is well replicated by

the model.

For each grid point, the rain period with the highest rainfall accumulation can be placed on a color matrix and mapped out to create a bi-variate choropleth of intensity and duration (Fig. 3.13). Northern Taiwan exhibits scattered durations between 0-24 hours in both QPESUMS and WRF Control, but the northeastern coastline in the Control run is higher in duration than QPESUMS with rainfall between 24-36 hours. Higher intensities on the northwestern coastline are similar between QPESUMS and the Control Run. In central Taiwan, the Mei-yu rain band is associated with higher intensities and increasing terrain height is associated with higher rainfall durations. Both characteristics are shared between QPESUMS and WRF Control regardless of the positioning of the Mei-yu rain band. Smaller details such as the low duration, high intensity rainfall in southern Taiwan and low intensity rainfall on the leeside of the CMR is captured well by the model. With how well the Control run replicates QPESUMS, this gives confidence for using this WRF run for isolating topographic influences on precipitation at a high resolution.

3.7 Figures and Tables

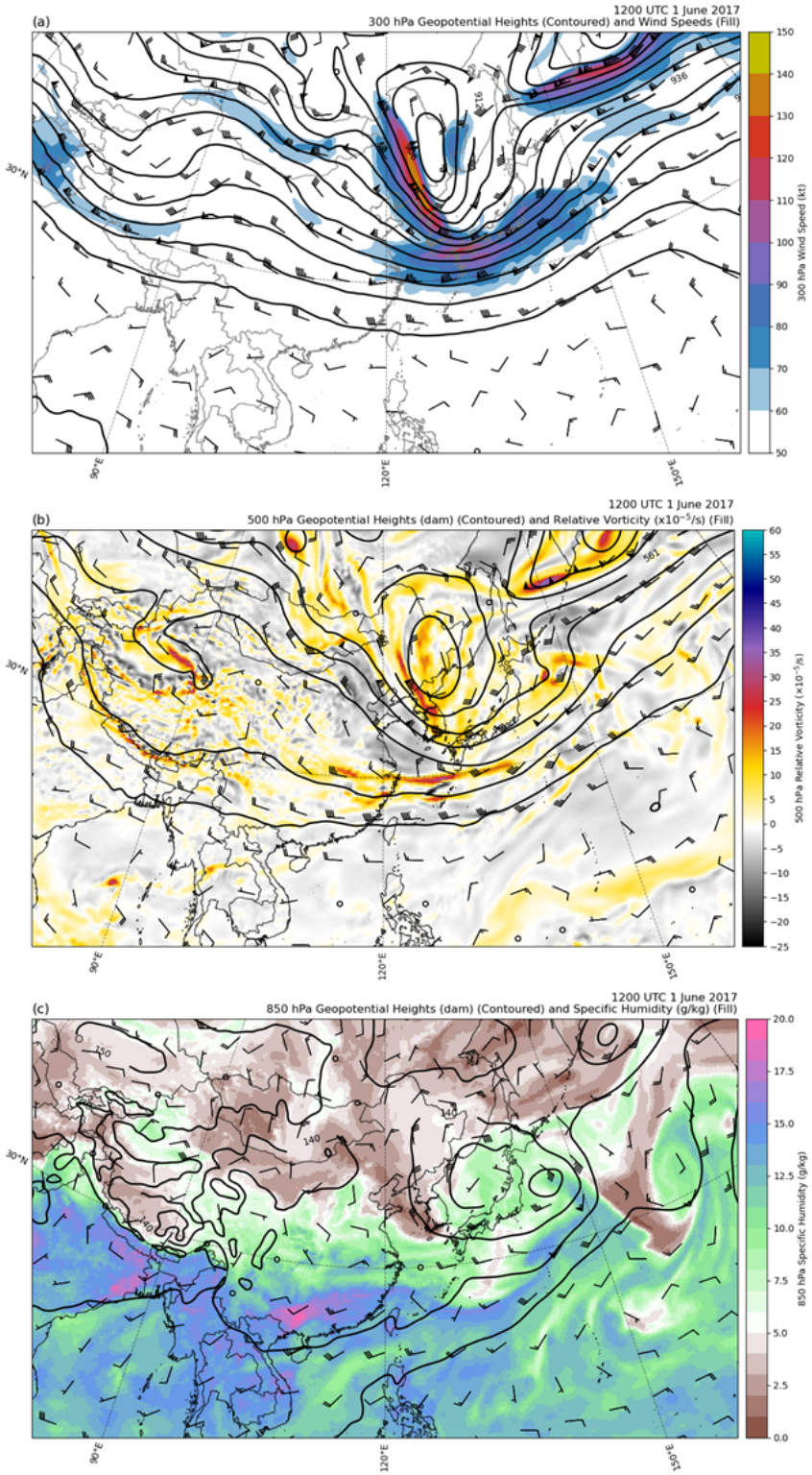

Figure 3.1: Synoptic conditions at 1200 UTC 1 June 2017 using ERA5. (a) 300 hPa wind speed in knots (fill), geopotential height in dam (contoured), and wind barbs. (b) 500 hPa relative vorticity (fill), geopotential height in dam (contoured), and wind barbs. (c) 850 hPa specific humidity in g/kg (fill), geopotential height in dam (contoured), and wind barbs.

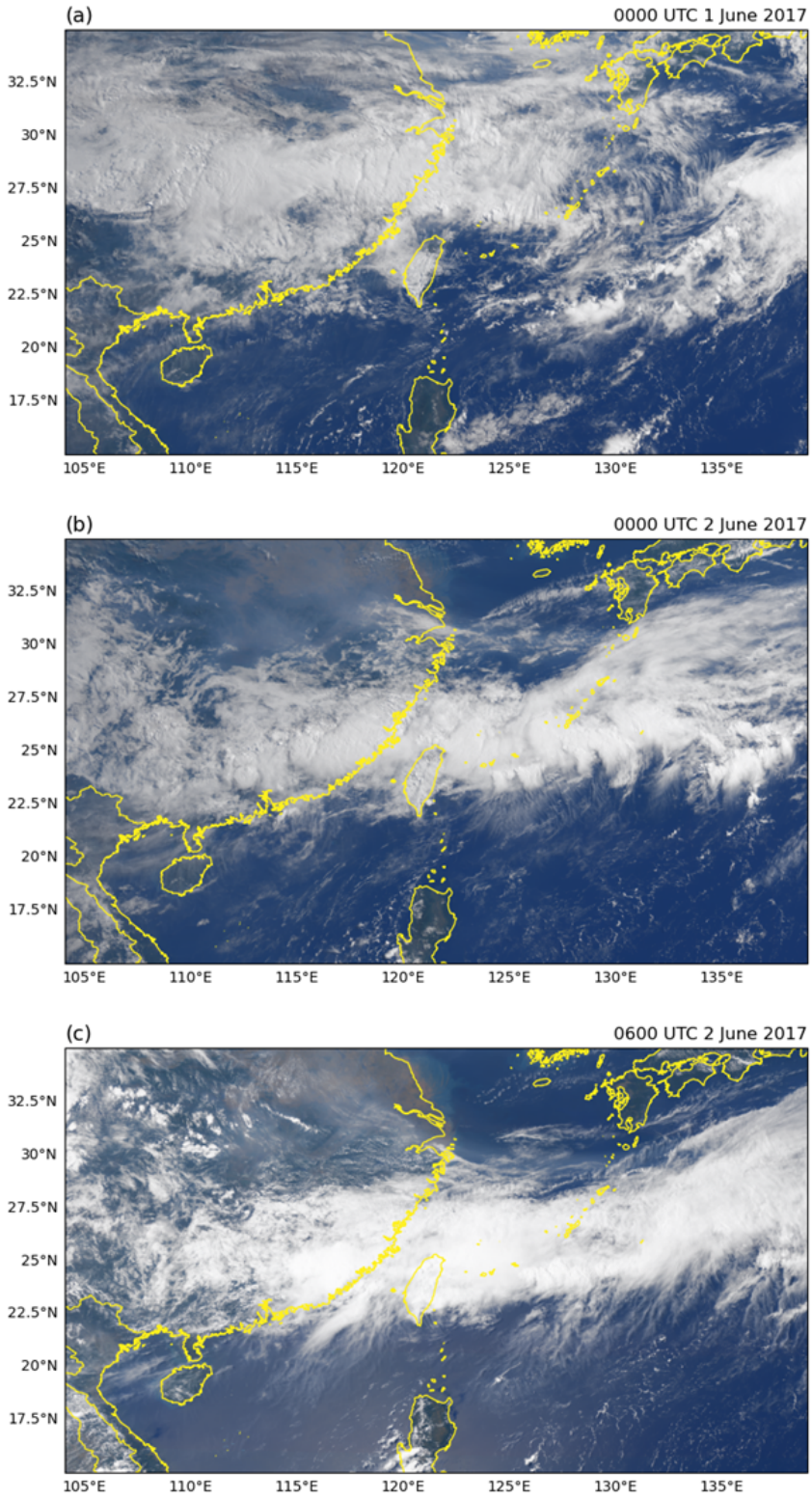

Figure 3.2: Himawari-8 corrected True Color for (a) 0000 UTC 1 June 2017, (b) 0000 UTC 2 June 2017, and (c) 0600 UTC 2 June 2017.

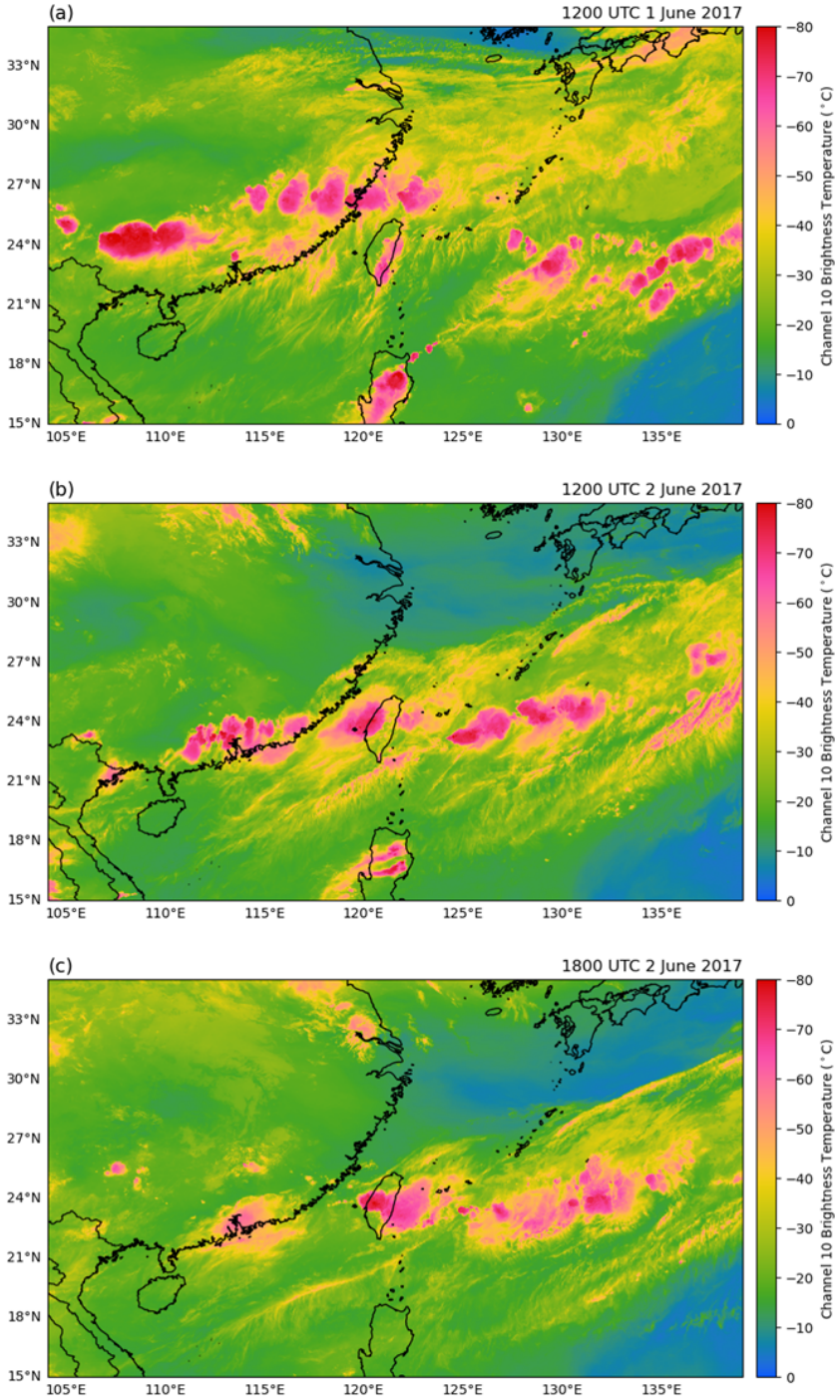

Figure 3.3: Himawari-8 channel 10 brightness temperature for (a) 1200 UTC 1 June 2017, (b) 1200 UTC 2 June 2017, and (c) 1800 UTC 2 June 2017.

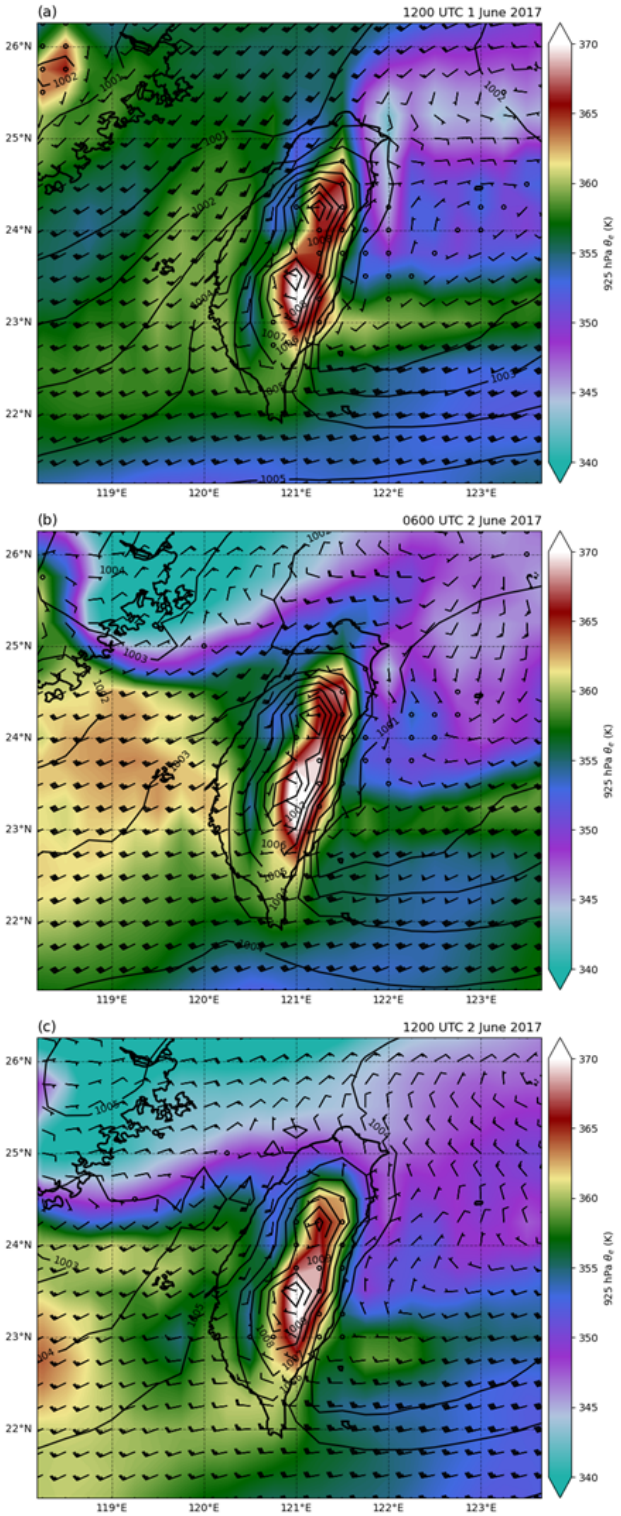

Figure 3.4: 925 hPa equivalent potential temperature and wind barbs with mean sea level pressure (contoured) using ERA5 at (a) 1200 UTC 1 June 2017, (b) 0600 UTC 2 June 2017, and (c) 1200 UTC 2 June 2017.

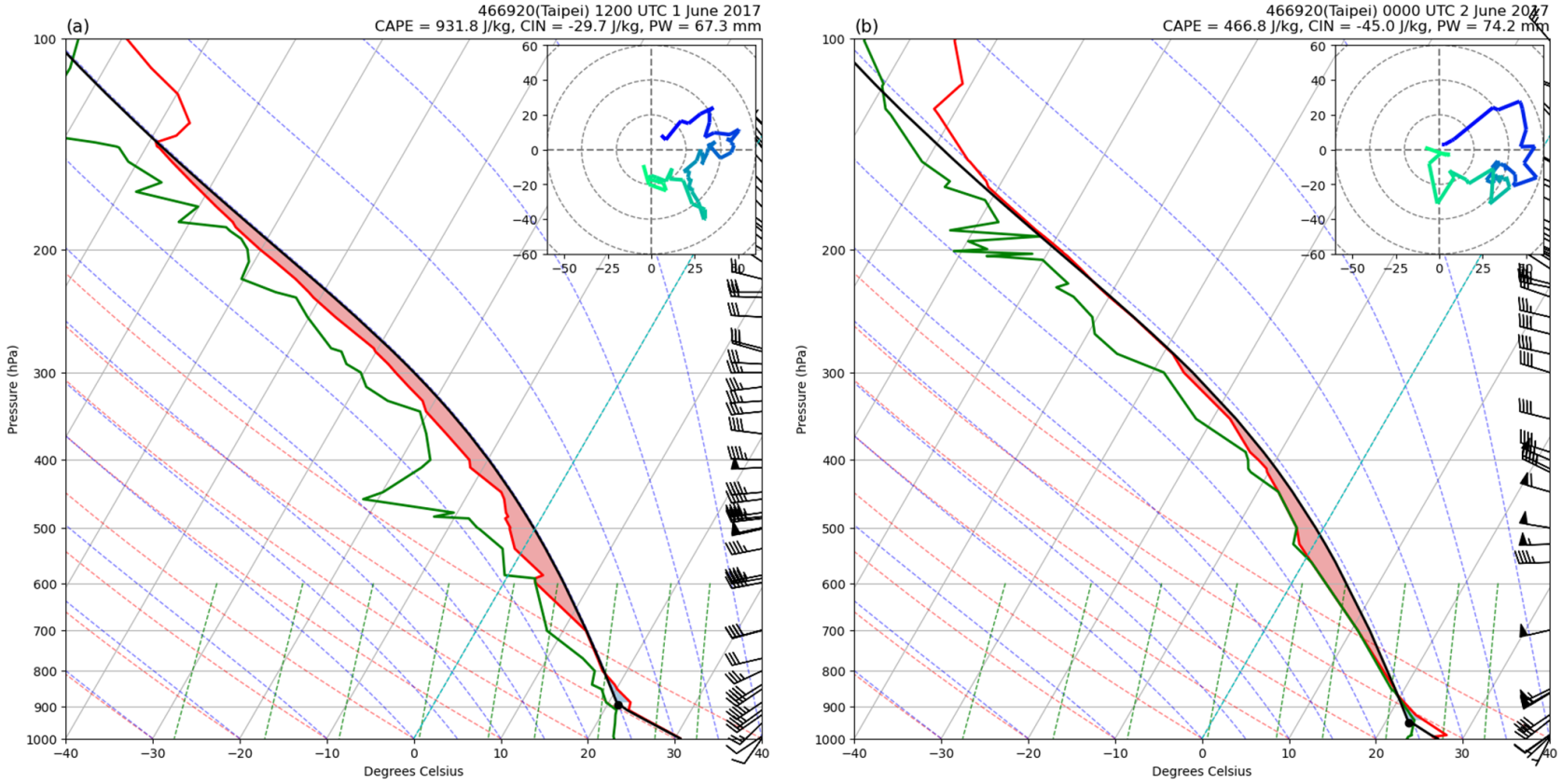

Figure 3.5: Skew-T diagrams and hodographs of radiosondes launched in Taipei at (a) 1200 UTC 1 June 2017, (b) 0000 UTC 2 June 2017

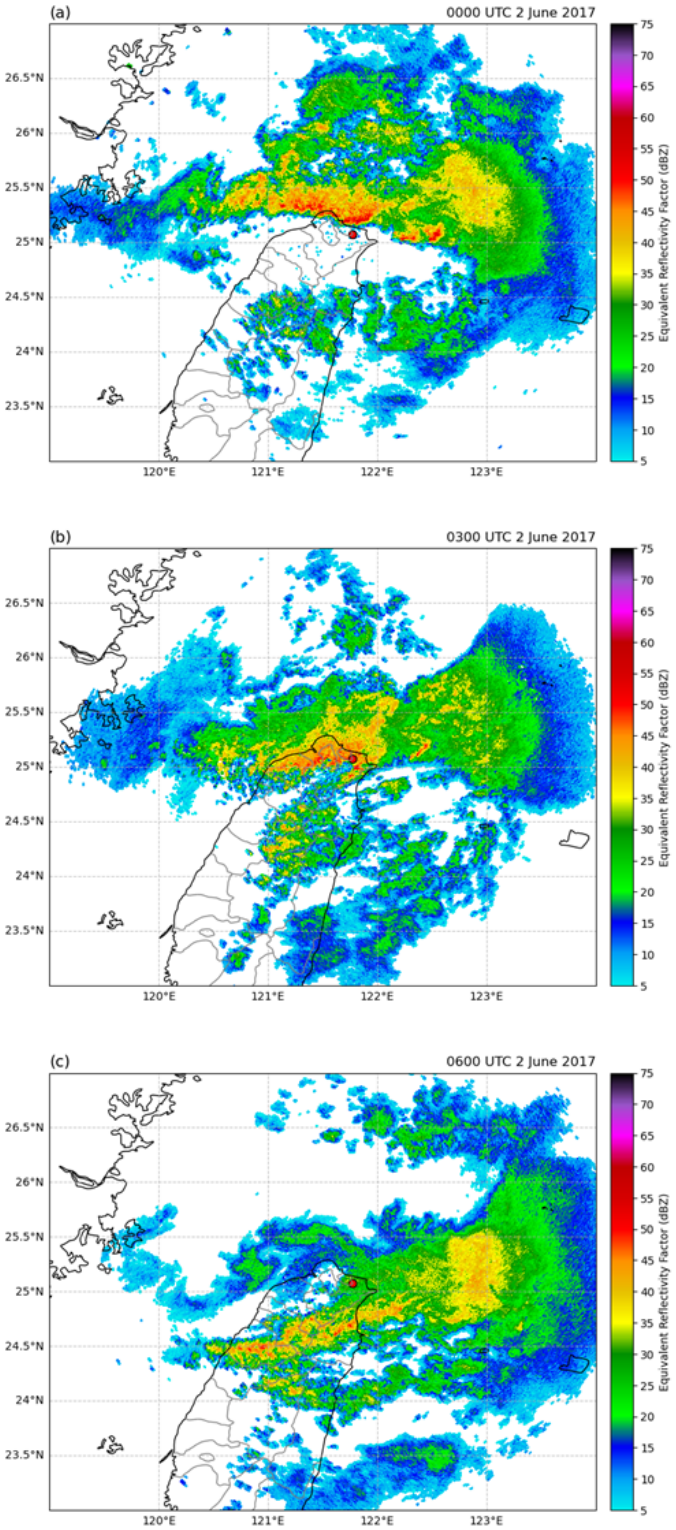

Figure 3.6: Equivalent reflectivity factor in dBZ from RCWF at 1.5o elevation angle for (a) 0000 UTC, (b) 0300 UTC, and (c) 0600 UTC 2 June 2017. The red point indicates the location of the radar.

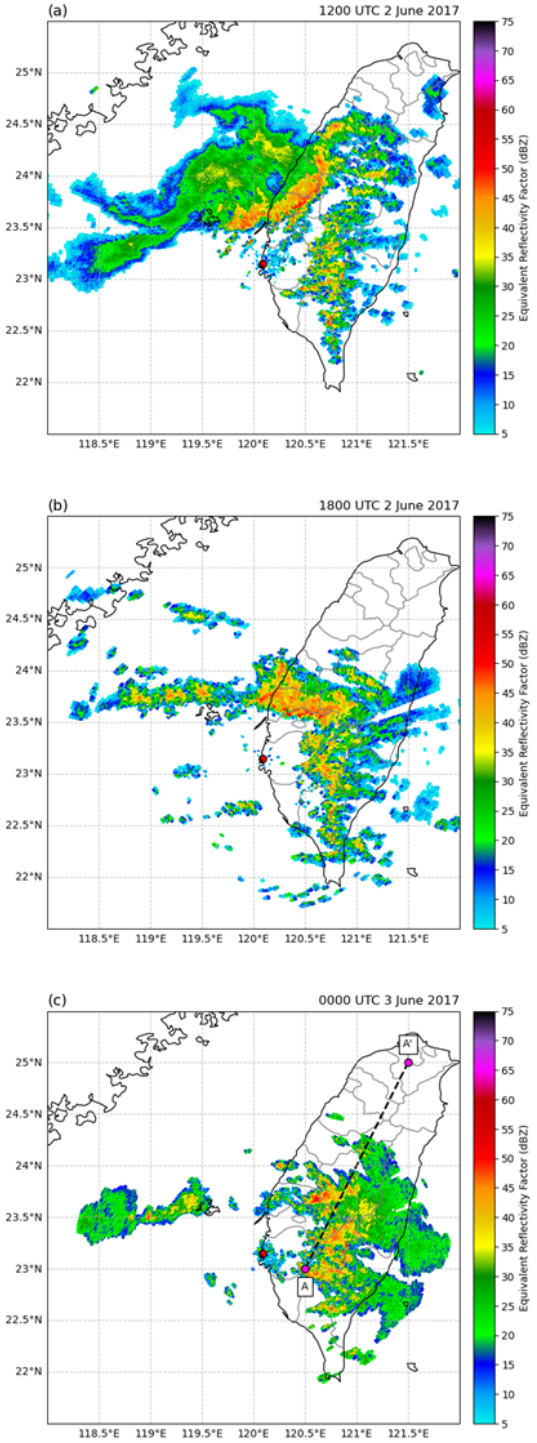

Figure 3.7: As in Figure 3.6 but using RCCG as the radar for (a) 1200 UTC 2 June 2017, (b) 1800 UTC 2 June 2017, and (c) 0000 UTC 3 June 2017. The dashed line in (c) represents the cross section in Figure 3.9.

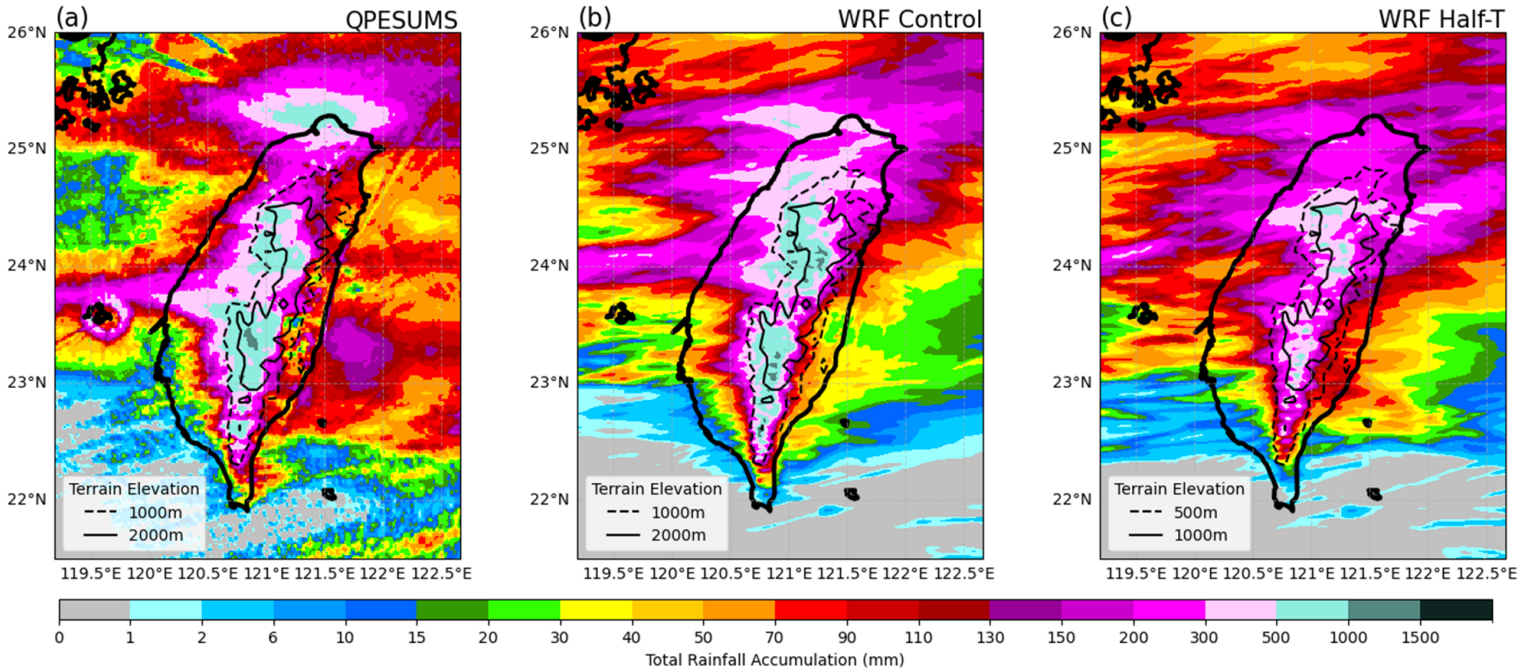

Figure 3.8: Rainfall accumulation from 1200 UTC 1 June 2017 to 1200 UTC 3 June 2017 for (a) QPESUMS, (b) WRF Control, and (c) WRF Half-T.

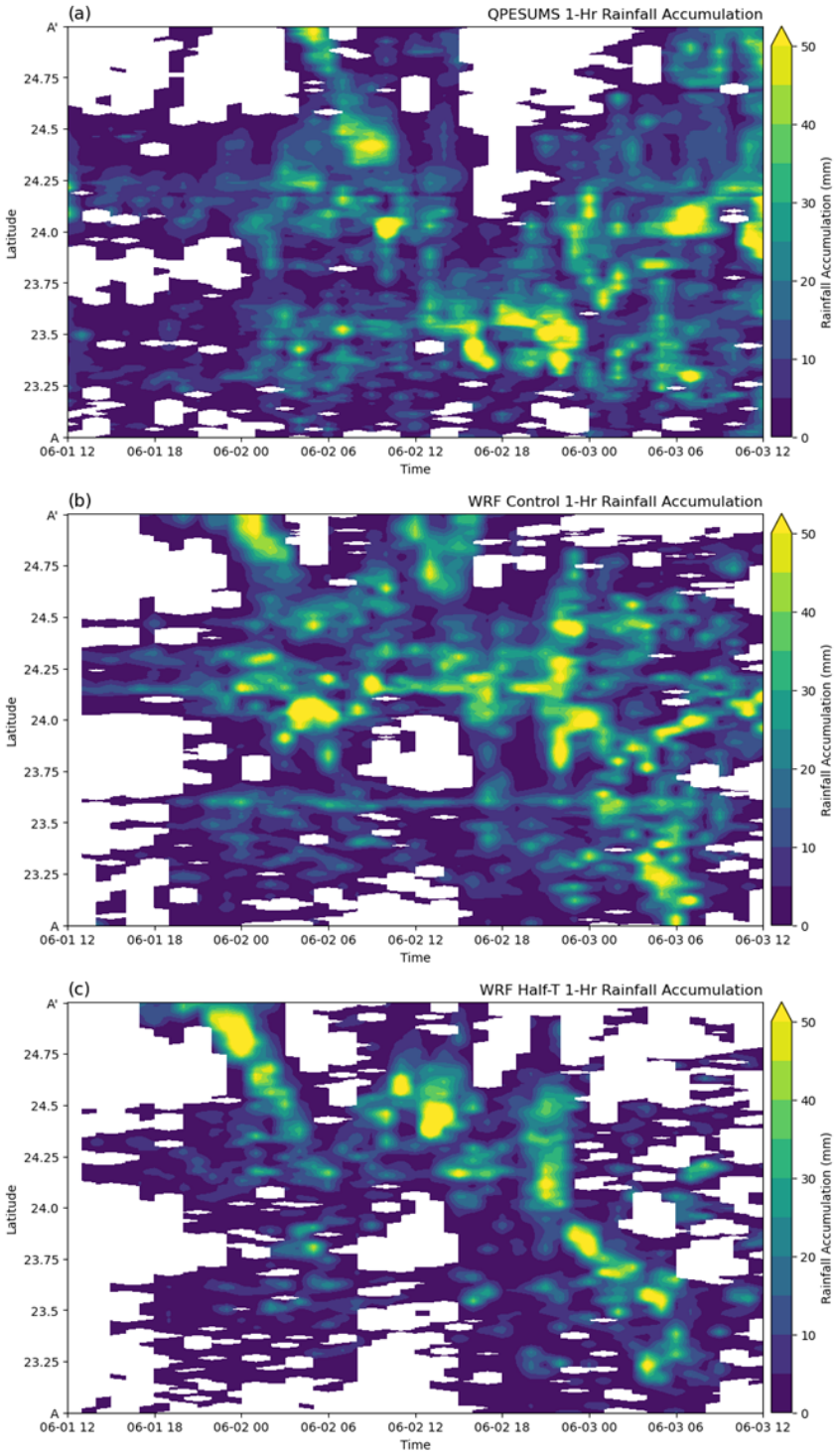

Figure 3.9: Hovmöller Diagram of 1-hour rainfall accumulation along the line AA' denoted in Fig. 3.7c using (a) QPESUMS, (b) WRF Control, and (c) WRF Half-T.

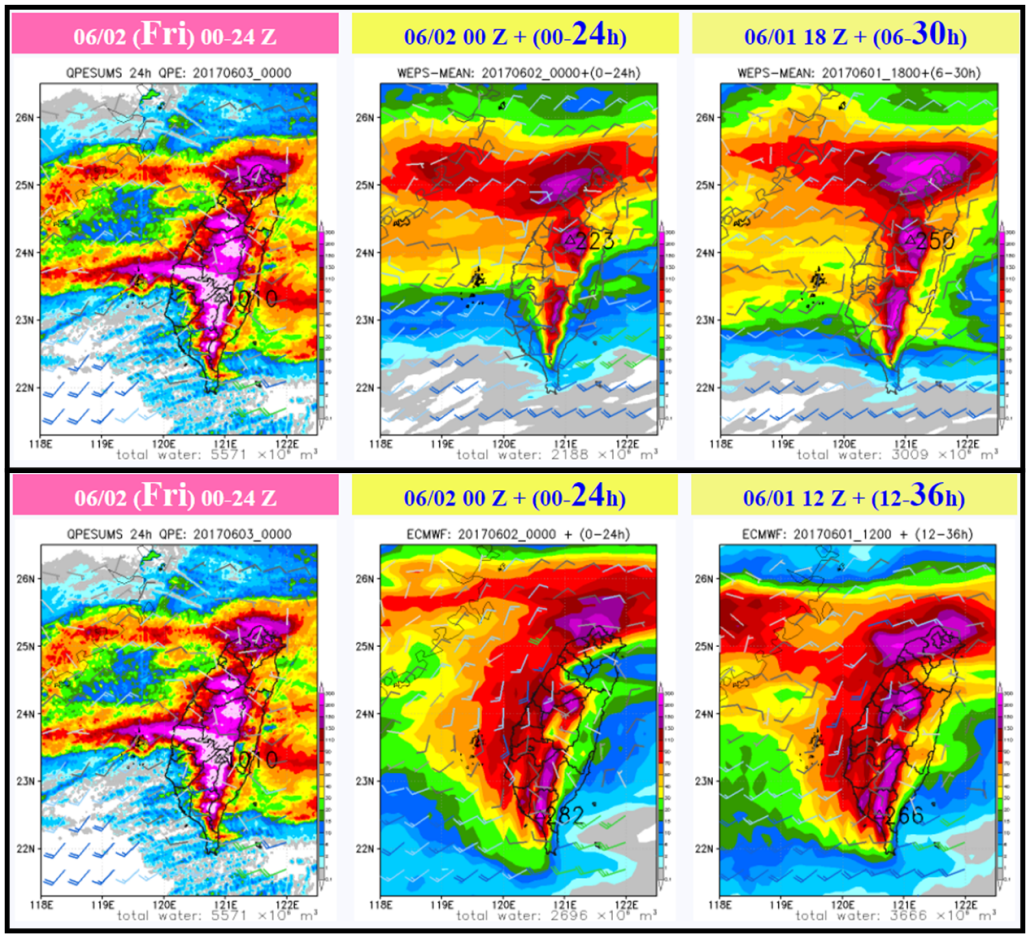

Figure 3.10: Rainfall accumulation for 2 June 2017 for (a, d) QPESUMS, (b, c) WEPS-Mean, and (e, f) ECMWF. (b) and (e) are forecasted rainfall accumulation with models initialized at 0000 UTC 2 June 2017. (c) and (f) are forecasted rainfall accumulation with models initialized at 1200 UTC 1 June 2017. Wind barbs from (a, d) are from radar dual doppler synthesis at 2.5 km AGL and wind barbs for (b, c, e, f) are for 10m AGL from their respective models. Triangles represent area of maximum rainfall. Total water indicates the total rainfall for the QPESUMS domain.

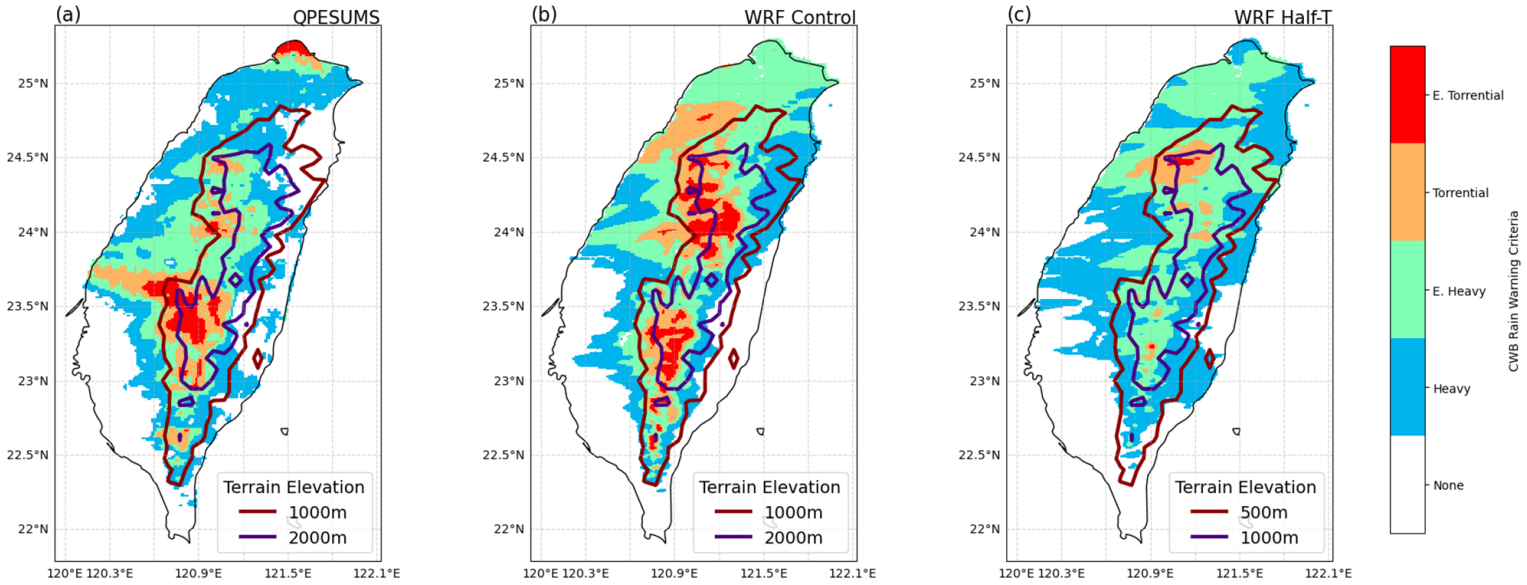

Figure 3.11: Highest theoretical CWB Warning issued based on rainfall accumulation between 1200 UTC 1 June 2017 and 1200 UTC 3 June 2017 for (a) QPESUMS, (b) WRF Control, and (c) WRF Half-T.

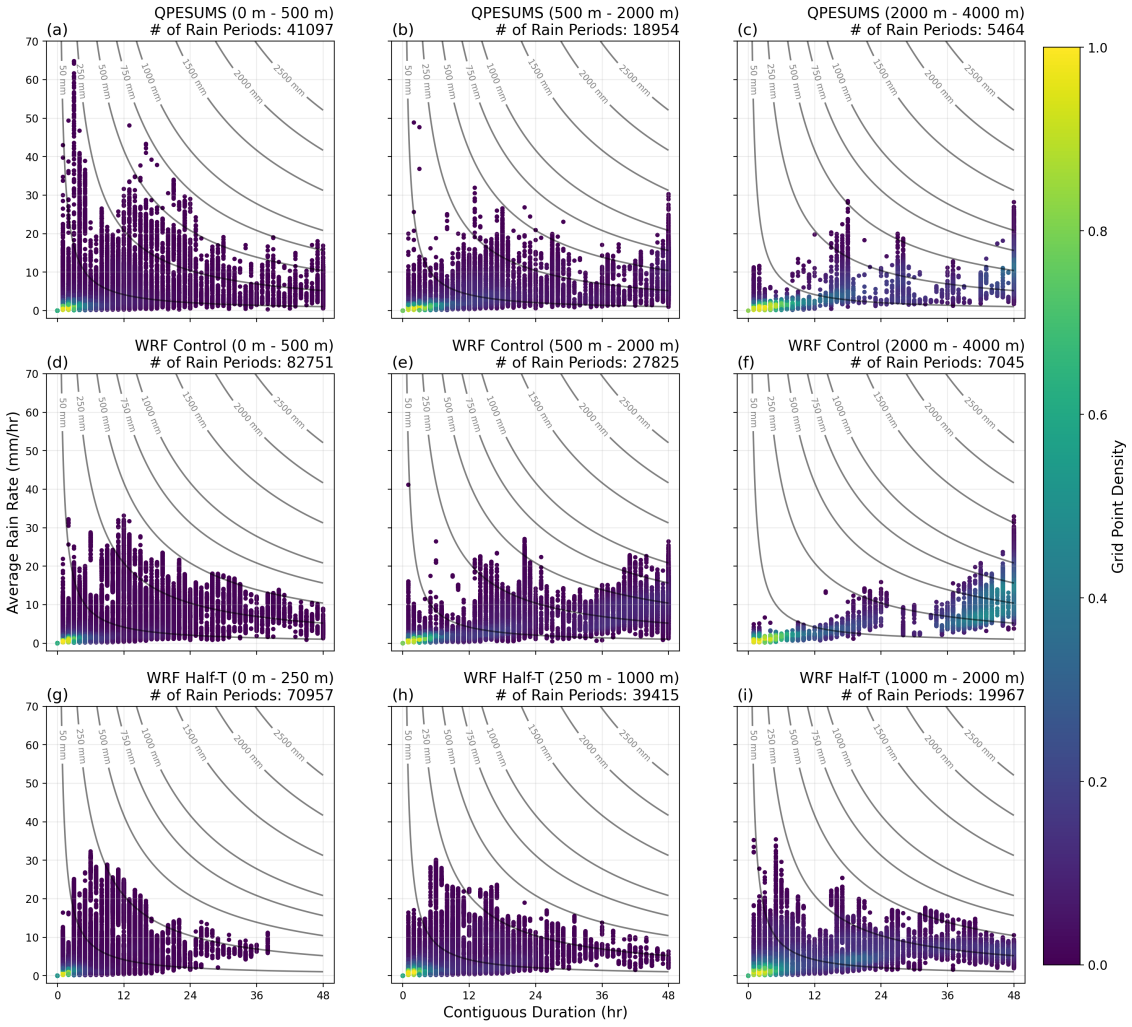

Figure 3.12: Intensity and duration scatterplots for all (a, b, c) QPESUMS, (d, e, f) WRF Control, and (g, h, i) WRF Half-T rain periods over land (a, d, g) between 0 – 500 m (0-250 m), (b, e, h) between 500 – 2000 m (250 – 1000 m), and between 2000 – 4000 m (1000 – 2000 m) terrain height for WRF Control (WRF Half-T) using contiguous duration with 1-hour gap allowance in rainfall. Grey contours represent lines of constant rainfall accumulation in mm.

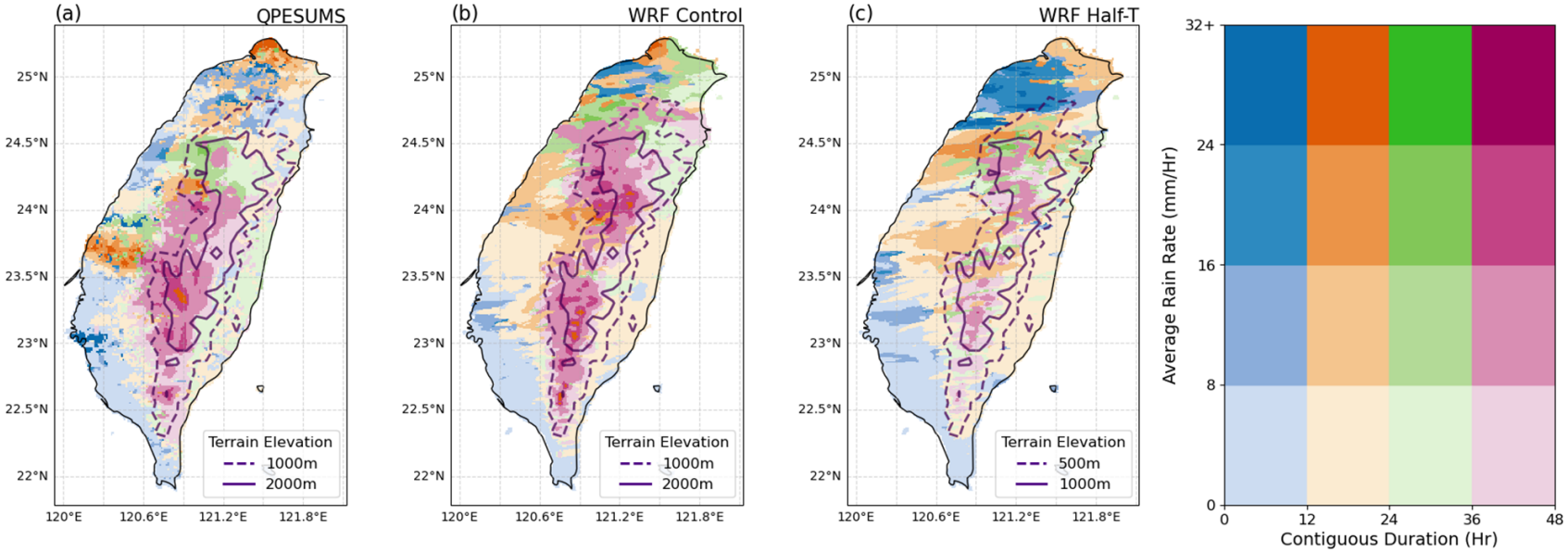

Figure 3.13: Bi-variate choropleth of contiguous duration and average rain rate of the highest rainfall accumulating rain period for each grid point for (a) QPESUMS, (b) WRF Control, and (c) WRF Half-T. (d) is the reference color matrix.

Table 3.1: CWB forecasting checklist for issuing extreme rainfall warnings for Mei-yu fronts (Wang et al. 2012).

(a) Surface Mei-yu front

1) Inside 20°-28°N, 118°-124°E
2) Taipei (25.03°N, 121.63°E) within 200 km south and 100 km north of the front
3) Kaohsiung (22.58°N, 120.42°E) within 200 km south of the front

(b) Humidity

4) 850 hPa dewpoint temperature (T_d) $\geq$ 15°C
5) 850 hPa equivalent potential temperature (θ_e) axis point toward Taiwan
6) 700 hPa dewpoint depression ($T - T_d$) $\leq$ 3°C

(c) LLJ (inside 18°-26°N, 115°-125°E)

7) Surface southwesterly flow of 10-20 kt
8) 850 hPa southwesterly flow > 25 kt
9) 700 hPa southwesterly flow > 30 kt
10) 850 hPa southerly-southwesterly flow $\geq$ 10 kt over northern SCS (north of 15°N)

(d) Temperature

11) 850-700 hPa cold tongue north of the wind-shift line
12) Taiwan in diffluent area of the 1000-500 hPa thickness field

(e) Wind shift line (inside 22°-28°N, 114°-127°E)

13) 850-700 hPa wind shift line

(f) Subsynoptic system (in southeastern China or northern SCS, east of 114°E

14) Surface or 850 hPa mesolow
15) 700-50 short-wave trough

(g) Pressure (over the proximity of Taiwan)

16) Taiwan in low pressure zone
17) Surface pressure < 1005 hPa

(h) Upper-level wind

18) 300-200 hPa diffluent flow with angle > 45°
19) Taiwan under 300-200 hPa right quadrant entrance to the jet streak

(i) Stability

20) K index > 35

Table 3.2: CWB severe weather advisory criteria.

	1-Hour Accumulation (mm)	3-Hour Accumulation (mm)	24-hour Accumulation (mm)
Heavy Rain	40		80
Extremely Heavy Rain		100	200
Torrential Rain		200	350
Extremely Torrential Rain			500

Chapter 4

Results

4.1 WRF Half-T

4.1.1 Rainfall Accumulation

The decrease in terrain height in the WRF Half-T run led to a broad decrease in precipitation in high terrain and northern Taiwan (Fig. 3.8). The rainfall maximum accumulation in the Control run was 1581 mm whereas the maximum in the Half-T run was 788 mm, both relative maxima found above the 2 km terrain height contour. Median rainfall accumulation over Taiwan was 232 mm for the Control run while the median for Half-T was 183 mm. Much of southern and eastern Taiwan experience similar rainfall totals in both the Control and Half-T runs for elevations below 1 km. A local maximum in rainfall accumulation is found in northwestern Taiwan in the Control run that is missing in the Half-T run. The Mei-yu rain band off the western coast has also shifted north in the Half-T run with a leeside band of precipitation that is missing in the Control run. Despite differences in rainfall accumulation, timing of the Mei-yu rain band in the Hovmöller diagrams is similar with both model runs making landfall at approximately 0000 UTC 2 June 2017, progressing south, and becoming quasi-stationary near 24.25°N, then progressing south again (Fig. 3.9b, c). The Hovmöller plots also highlight that in central and southern Taiwan, the reduction in terrain height reduces the amount of persistent rainfall found

between 23.25°N and 23.75°N regardless of Mei-yu association.

It should be noted that while the reduction in terrain height has dramatically reduced maximum and median rainfall accumulation for this event, it still qualifies as extremely torrential based on the CWB rainfall criteria (Fig. 3.11b, c). The reduction in terrain height shifts the extremely torrential rain warning to the northwestern edge of the SMR. This is different than the Control run where both the CMR and a greater area of the SMR qualify for extremely torrential rainfall. Most regions that would have received a warning in the Control run would have received a warning in the Half-T run. With the apparent shift in rainfall warnings, there would be an accompanying shift in rainfall intensity and duration.

4.1.2 Intensity and Duration

In comparing WRF Control and Half-T through the intensity and duration framework, elevation bins were scaled to represent the same areas rather than the same elevations (Fig. 3.12d-i). For example, the low elevation bin for the Control run represents 0-500 m terrain height whereas the low elevation bin for the Half-T run represents 0-250 m terrain height. The reduction in terrain height had little effect on low duration rainfall in the low elevation terrain bin but decreased the maximum attainable rainfall duration from 48 hours to 38 hours (Fig. 3.12d, g). Within the medium terrain height bin, few Half-T rain periods are able to attain a maximum rainfall duration of 48 hours (Fig. 3.12h). The few rain periods that do are all low intensity with average rain rate below 10 mm/hr, whereas the Control run produces maximum rain duration rain periods with average rain rates upwards of 20 mm/hr (Fig. 3.12e). The Control run also experiences a slight shift in density to higher rainfall duration that is not seen in the Half-T run. Within the highest elevation bin, the distributions of rainfall intensity and duration are most dissimilar (Fig. 3.12f, i). The Control run continues the shift in density toward high duration rainfall as well as an increase in rainfall intensity at maximum rainfall duration. The Half-T run continues to have low intensity at high duration and higher intensity at low duration. The

Half-T run also has a slight increase in density toward higher duration rainfall, indicating that regardless of model run, areas of increased terrain height are likely to experience greater rainfall duration. Rainfall intensity does not seem to increase with terrain height except in the case of maximum duration rain periods in the Control run.

When mapped using the bi-variate choropleth (Fig. 3.13b, c), spatial trends emerge to bolster the results of the intensity and duration scatterplots. At high altitudes found within the CMR, rainfall intensity decreases in the Half-T run. Within the Control run, much of the western sides of the CMR and SMR are within the 36-48-hour rainfall duration bin, but the Half-T run drops to durations between 12-36 hours. The most striking drop in intensity and duration can be found where the Mei-yu rain band becomes quasi-stationary in the Control run. Within central Taiwan (23.5°-24.25°N), some of the most intense and highest duration rainfall is found within the Control run, but a stark drop off in intensity from the western coastline to the CMR and a drop in rainfall duration above the 500 m terrain height contour in the Half-T run highlights a region of interest for further analysis. Another region of interest for investigating orographic controls on rainfall intensity and duration is northern Taiwan (>24.75°N). Whereas the Control run has a wide array of low and high durations and intensities in northern Taiwan, the Half-T run experiences overall lower duration with similar intensities. Understanding the link between reduced terrain and reductions in rainfall intensity and duration in these regions, Northern and Central Taiwan, will be the focus of the next two subsections.

4.2 Northern Taiwan

4.2.1 Barrier Jet Formation

Prior work by Tu et al. (2022) highlight the sensitivity of the 1-3 June 2017 Mei-Yu front propagation to slight modifications in topography with the removal of the Yang-Ming mountains (Fig. 4.1). While their study finds that the removal of the mountains increases the propagation speed of the front, they also placed the barrier jet as a key contributor to

lifting along the front and producing heavy rainfall along it. This barrier jet in their study was replicated well at 900 hPa within WRF in both the Control and Half-T run (Fig. 4.2). At 1800 UTC 1 June 2017, the Control run exhibits 900 hPa wind speeds above 50 knots along the northwestern coastline whereas the Half-T run is slightly weaker between 40-45 knots (Fig. 4.2a, b). Evidence of these barrier jets originating from upstream orographic blocking is found in southern Taiwan with southwesterly flow slowing down on approach toward the CMR. The degree of slow down is larger for the Control run with flow off the coast between 30-35 knots and dropping to 10 knots near the CMR in the Control run while the Half-T run drops to 20 knots. A common way of determining orographic blocking is through high perturbation heights upstream of orography (Pierrehumbert 1984). Figure 4.3 shows 900 hPa perturbation heights for both the Control and Half-T run at 1800 UTC 1 June 2017. Both model runs have a high perturbation height collocated with the slow down of flow with the Control run having a 5-10 m greater perturbation, giving confidence that while orographic blocking is evident in both runs, the strength of the blocking is stronger in the Control run.

A tool often used to diagnose the degree of orographic blocking is the Froude number defined as:

$$Fr = \frac{U}{Nh} \tag{4.1}$$

Where U is the wind speed orthogonal to a mountain, N is the Brunt-Väisälä frequency, and h is the mountain height. Froude number values larger than 1 are unblocked with inertial forces overtaking the stability of the atmosphere and allowing for orographic lifting of a parcel. Should the Froude number be less than 1, a parcel's inertia is not able to overcome the atmosphere's stability, pushing orographic lift upstream of the orography with a portion of the flow orographically deforming (Pierrehumbert 1984; Kirshbaum et al. 2018; Chen et al. 2008; Chen and Lin 2005).

An orographic deformation radius can thus be defined as:

$$L_d = \frac{Nh}{f} \tag{4.2}$$

Where N is the Brunt-Väisälä frequency, h is the mountain height, and f is the Coriolis parameter (Pierrehumbert and Wyman 1985). In the presence of orographic blocking due to a mesoscale mountain range, the orographic deformation radius is the distance upstream of the orography whereby orographic blocking extends. For an idealized mountain range with length L_y, the orographic deformation radius becomes L_y if the mountain range length is far less than that of the orographic deformation radius. These two tools in tandem, the Froude number and orographic deformation radius, can determine the degree and extent of orographic blocking. For example, for a Froude number less than 4/3, deceleration is found within the orographic deformation radius and for a Froude number less than 2/3, zones of near stagnant air will also exist within the orographic deformation radius. Lin (1993) provides simple measurements for estimating the orographic deformation radius with length of the CMR being approximately 300 km and the average height being 2 km. Assuming the Brunt-Väisälä frequency to be 0.1 s^{-1} and the Coriolis parameter is approximately $6\times10^{-}5$ s^{-1}, we find that the orographic deformation radius for Taiwan is approximately 333 km, slightly higher than the length of the CMR. With halved terrain height, the Half-T run will have an orographic deformation of 166.5 km, significantly less than the length of the CMR. For this reason alone, regardless of flow speed, differences in the orographic blocking extent should differ between model runs.

The extent and depth of the orographic blocking is analyzed through the cross sections as shown in Figure 4.2. Cross section BB' points from far off coast and ends at the peak of the Jade Mountain. Cross section CC' runs parallel to BB' but is shifted north ending at the northernmost peak of the CMR to capture downstream effects of the orographic blocking. A modification to the Froude number is such that it takes on a height relative form:

$$Fr(z) = \frac{U(z)}{N(z)[h-z]} \tag{4.3}$$

This modification better visualizes the horizontal and vertical extent of orographic blocking. Cross sections BB' and CC' (Figs. 4.4 and 4.5) contain a cross section-relative tangential wind speed that points toward the orography, a cross section-relative orthogo-

nal wind speed, and a height-relative Froude number using the peak terrain height of the cross section and the tangential wind speed.

For both BB' and CC' in the Control run, orographic blocking runs nearly the full extent of the cross sections with Froude number values under 1 below 2 km height (Fig. 4.4a, b). The lowest Froude numbers in each cross section are collocated with stagnant zones with near zero tangential wind flow situated near the terrain (Fig. 4.4c, d). Tangential wind speeds below the 2 km blocking height slow down when crossing the coastline for both BB' and CC', but for BB' this slow down is greater in magnitude. A partial reason why is found in the orthogonal wind speeds and vertical velocity (Fig. 4.4e, f). While both BB' and CC' have predominantly southeastward orthogonal flow off the coast, CC' is found to have northwestward orthogonal flow on land and near topography, indicating that flow has turned counterclockwise relative to BB' on land. Tangential flow along BB' is being orographically blocked and transported to northern Taiwan as evidenced by the southerly flow found in CC' in the Control run.

Within the Half-T run, orographic blocking is reduced along BB' and CC' (Fig. 4.5a, b). The only regions with Froude number less than 1 along BB' are found within 10 km of the topography. There is a corresponding slow down of tangential flow on land in BB' similar to the Control run with near stagnant zones collocated with Froude numbers less than 1; overall, however, the tangential winds are stronger below 2 km height in the Half-T run compared to the Control run (Fig. 4.5c). Orthogonal winds along BB' are similar in strength to those found in the Control run (Fig. 4.5e). Updrafts indicated by positive vertical velocity are found closer to the peak of the Jade Mountain. The result of this weaker orographic blocking in the Half-T run is seen downstream along CC' where the positive orthogonal winds near the terrain are significantly weaker relative to CC' in the Control run (Fig. 4.5f). Therefore, as southwest flow in both model runs encounter the Jade Mountain, the weaker orographic blocking in the Half-T run leads to less diversion of flow from southern Taiwan to northern Taiwan, reducing the strength of the barrier jet.

4.2.2 Effects of Barrier Jet on Rainfall

The effect of the barrier jet on the Mei-yu front and rainfall associated with it is most prominent upon landfall of the Mei-yu front in this case. To track the Mei-yu front over both ocean and land, a modified form of the Parfitt et al. (2017) frontal diagnostic will be used at 900 hPa:

$$F = \frac{F^*}{f|\nabla T|_0} \tag{4.4}$$

with

$$F^* = \zeta_p|\nabla(\theta_e)| \tag{4.5}$$

$$|\nabla T|_0 = \frac{0.45K}{100km} \tag{4.6}$$

The modification made is changing the thermal variable from temperature in F^* to equivalent potential temperature as the Mei-yu front has a less defined thermal gradient compared to midlatitude fronts. Should the frontal diagnostic go above a value of 1, there is confidence of there being a Mei-yu front present with increasing confidence as the value increases over 1. There are numerous methods of tracking the Mei-yu front (Ninomiya 1984; Cho and Chen 1995), most of which are modified forms of frontogenesis. Unfortunately, since these frontogenetic equations often rely on deformation of flow along the front, orographic deformation can be misconstrued as a front as well. Therefore, a modified form of the Parfitt et al. (2017) method works best for this study.

The Mei-yu front makes landfall at approximately 1900 UTC 1 June 2017 in both model runs (Fig. 4.6). The front is aligned on top of the northwest coastline and extends west into the Taiwan Strait in both model runs with heavy rainfall in the next hour spatially correlated with the location of the front. The eastern edge of the Mei-yu front is coincident with a mesolow on the northernmost coastlines near Yangmingshan National Park. Wind barbs at 900 hPa reveal that at this time, the barrier jet is approximately 5-10 knots stronger in the Control run pointing toward the northeast. Downstream of the barrier jet, lighter rainfall is present over the next few hours.

Two hours later at 2100 UTC 1 June 2017, the Mei-yu front on land remains at the

same location along the northwestern coastline in the Control run whereas the Half-T front has begun to progress south (Fig. 4.7). Both model runs have the fronts off the western coast progressing south, however. Despite the Half-T front progressing south on land, there is a small portion that is still present to the north of the Yangmingshan National Park, consistent with the findings of Tu et al. (2022). Heavy rainfall remains linked with the locations of the fronts as well as lighter rainfall downstream of the barrier jets. The barrier jet in the Control run has not changed in strength or size relative to two hours prior, but the barrier jet in the Half-T run has diminished in both respects in proximity to the Mei-yu front.

At 2300 UTC 1 June 2017, the Control Mei-yu front is still anchored to the northwestern coastline on land whereas the Half-T front has progressed even farther south (Fig. 4.8). Similar to two hours prior, the fronts over the ocean continue to progress south. Unlike prior hours, the location of heavy rainfall in the Control run is only collocated with the off-coast front. On land, the heavy rainfall is not collocated with the front, but forms downstream of the off-coast front. In the Half-T run, the heavy rainfall is linked to both the on-land and off-coast fronts, with the mesolow situated on the eastern edge of the front intensifying postfrontal northeasterlies enough to reorient the front on land to west-northwest to east-southeast. The Control barrier jet has not diminished in strength, but the Half-T jet has regained some strength similar to 4 hours prior, producing heavier rainfall behind the Mei-yu front. The lighter precipitation downstream of the barrier jets has remained the same for the Control run, but the Half-T run has the downstream precipitation shifted south with the progression of the Mei-yu front. Precipitation along the northern most coastlines have subsided for the Half-T run.

For most of the Mei-yu front's period in northern Taiwan, the heaviest rainfall remains linked with the location of the Mei-yu front. Despite modifying the terrain height, the rainfall intensity over this 4-hour period has not shown much difference. Therefore, the decrease in rainfall duration in the Half-T run can be attributed to the Mei-yu front's faster progression on land. Although the differences in barrier jet strength may be the

cause of the varying Mei-yu front propagation speeds, there is also a possibility the SMR was the cause. There is a wealth of literature on the effects of topography upstream of midlatitude fronts slowing their propagation (Blumen 1992; Dickinson and Knight 1999; Egger 1992). The first obstacle the Mei-yu fronts encounter is the SMR and with the reduced terrain height in the Half-T run, it is possible the speed up in frontal progression is due to that rather than the barrier jet.

4.2.3 Northern Taiwan Trajectory Analysis

To determine if the barrier jet contributes to frontal progression, a RIP trajectory analysis was performed on the Control and Half-T runs. Parcels were released from three different locations upstream of the barrier jet with each release group aligned along the same latitude but with differing proximities to the CMR (Fig. 4.9, 4.10, 4.11). Within each parcel release group, parcels were released every hour starting at model forecast hour 0 (1200 UTC 1 June 2017) and ending at model forecast 12 (0000 UTC 2 June 2017) each terminating at 0200 UTC 2 June 2017. While the barrier jet is predominantly found at the 900 hPa level, this does not account for parcels lifting or descending to that level on route to the barrier jet. To try and account for these parcels, the trajectories were also released at 875 hPa and 925 hPa. In total, each model run will have 117 parcels.

If the barrier jet plays a role in slowing down the Mei-yu front, parcels originating from the third release group should enter northern Taiwan more in the Control run than in the Half-T run because that release location is closest to where upstream orographic deformation should form. Release group 2 should have less of a difference between models and release group 1 should have even less of a difference given their increasing distance to the CMR. For the purposes of overall impact in northern Taiwan, northern Taiwan will be denoted as the region bound between the northern coastline and 24.75°N (gray shading in Fig. 4.12).

Control parcels in release group 1 overwhelmingly enter northern Taiwan (Fig. 4.12a, Table 4.1) whereas approximately half the number of parcels in the Half-T run make it

to northern Taiwan (Figure 12b, Table 4.2). Instead, parcels in the Half-T run opt to summit the SMR and CMR rather than orographically deform. The northward deflection found in the Control run is strong enough that some parcels do not register as entering northern Taiwan but surpassing the northern coastline. These trends continue into release group 2 (Fig. 4.12c, d) with a larger portion of parcels entering northern Taiwan in the Control run in comparison to the Half-T run. That being said, the number of parcels entering northern Taiwan, regardless of model run, has decreased relative to release group 1 (Tables 4.1, 4.2). The degree of decrease is different however with the Control run dropping from 25 parcels to 21 parcels whereas the Half-T run drops from 12 parcels to 3 parcels indicative of a decrease in orographic blocking in proximity to the mountain ranges. Release group 3 sees another drop off in the number of parcels entering northern Taiwan within both model runs (Fig. 4.12e, f). While the Control run has more parcels summiting the CMR in release group 3 than release group 1, the number of parcels that enters northern Taiwan is still larger than that of release group 1 in the Half-T run (Tables 4.1, 4.2). As each release group moves closer to the topography, there is a reduction in parcels reaching northern Taiwan indicating that greater deflection of flow is found farther upstream of topography. In the Control run, parcels originating from the 900 hPa and 925 hPa levels are most likely to enter northern Taiwan whereas the Half-T run mostly has parcels originating from the 925 hPa level entering northern Taiwan.

The reduction in terrain height found in the Half-T run resulted in a weaker barrier jet manifesting from weaker upstream orographic deformation in comparison to the Control run. This modification to the barrier jet increased the southern propagation speed of the Mei-yu front and with it, a decrease in duration of heavy rainfall collocated with front. While the orography was indirectly modifying the front through the barrier jet, the orography did not directly modify the rainfall. As the front progresses south into central Taiwan, these expectations aren't expected to hold as the front comes in direct contact with the orography.

4.3 Central Taiwan

4.3.1 Mei-yu Frontal Positioning in Central Taiwan

Although the highest rainfall totals of the June 2017 Mei-yu front event occur in central Taiwan, there are no studies that have explored this front as it progresses south past Taipei Basin. Furthermore, Mei-yu front progression in central Taiwan outside of this event is seldom studied with previous efforts only focusing off the western coast (Wang et al. 2012). One of the main reasons for this lack of research is in the difficulty of tracking the front on land and near topography.

The conventional dichotomy of prefrontal southwesterlies and postfrontal northeasterlies found in a Mei-yu front breaks down when the front is oriented perpendicular to the CMR. 900 hPa winds averaged over a 6-hour period reveal that while the front is in central Taiwan, typical postfrontal northeasterlies are missing from central to northern Taiwan for both model runs (Fig. 4.13). In both model runs a leeside cyclone forms to the northeast of Taiwan blocking possible postfrontal northeasterly winds from reaching the Mei-yu front situated on the western slopes of the CMR. This cyclone forms as a result of southwest winds curving around the southern end of the CMR, as well as leeside troughing of southwest winds. Even if the cyclone was not present, postfrontal northeasterlies would likely be orographically blocked by the SMR on approach to central Taiwan. This potential blocking of postfrontal winds would be due to their weaker magnitude compared to prefrontal southwesterlies which were found to be blocked in northern Taiwan (Fig. 4.4b, 4.5b). As such, identifying the Mei-yu front over land is a challenge, especially in west central Taiwan.

Figures 4.14 and 4.15 step through 3 hours for both model runs zooming in on west central Taiwan showing wind direction, the modified Parfitt et al. (2017) frontal diagnostic, and wind barbs at 950 hPa. Differences in timing between model runs captures similar starting positions of the fronts identified off the west coast. The frontal diagnostic shows a front extending over land at 950 hPa, more so than at 900 hPa (not shown).

At the start of analysis for each model run, there is a clear Mei-yu front extending

off the western coast of central Taiwan between 23.75°N and 24°N (Figure 4.14a, 4.15a). While relatively similar in positioning over the Taiwan Strait, frontal locations are dissimilar on land between model runs. Prefrontal winds are similar between model runs with southwesterly winds blowing between 30-35 knots. The postfrontal sectors are drastically different, however. Far to the north of the fronts, there are north-northeasterly winds. Closer to the Mei-yu front, they turn counterclockwise, becoming westerlies. The degree of turning is sharper for the Control run in comparison to the Half-T run, which is hypothesized to be the result of frontal deformation.

Thereafter in the Half-T run, postfrontal westerlies run parallel to the Mei-yu front, identified by the frontal diagnostic between 24°N and 24.5°N, but is increasingly difficult to pinpoint exactly where the front is located on land. The Control run has a more complex postfrontal sector on land where the postfrontal westerlies encounter the steeper SMR and appear to orographically deform, splitting into south-southwesterly winds to the north and northwesterly winds to the south. These northwest winds collide with the prefrontal southwesterly winds to create a front on land that is not only more easily identifiable than the Half-T run, but is pushed south more than the Half-T run closer to 23.75°N.

An hour later,postfrontal northwesterlies begin to emerge in the Half-T run (Fig. 4.15b), with a more recognizable front on land that is located farther south between 23.75°N and 24°N. This front is mostly linear in orientation which contrasts the Control front (Fig. 4.15b) which has become distorted on land. A similar postfrontal pattern exists from an hour prior for the Control run. Since the suspected orographic deformation is only found close to the topography based on wind direction shifts, however, the front is only pushed south where we find the postfrontal northwesterlies. This effect creates a deviated pattern in the Control front where it is less identifiable and pushed north at the coastline, but more identifiable and pushed south in proximity to the topography. Despite the emergence of postfrontal northwesterlies in the Half-T run, the Control front on land and near the terrain is still farther south by comparison.

One more hour later and the Control front near the terrain has not moved much on land despite the front over the ocean progressing south (Fig. 4.14c). The postfrontal sector of the Half-T run has become almost entirely northwesterly, maintaining a linearly oriented front on land which has progressed more south than the Control front in the past hour (Fig. 4.15c). Although the postfrontal sector is likely the cause of frontal progression speed, there is likely another contribution from the prefrontal sector with some evidence of stronger orographic deformation in the Control run leading to more southerly winds near the terrain compared to the more westerly winds in the Half-T run. This observation supports a slower southern progression of the Control front on land in comparison to the Half-T front. Although the strength of the postfrontal northwesterlies that form from suspected orographic deformation in the Control run are comparable to that of the Half-T run's postfrontal northwesterlies, the area that the postfrontal northwesterlies cover is different with the Control run only exhibiting northwesterlies close to the topography and the Half-T run having northwesterlies extending far beyond the coastline. The existence of the postfrontal northwesterlies is likely important for maintaining the front and their strength and spatial extent affects frontal progression south.

Many of these trends at 950 hPa are observed at other levels. By looking at the 925 hPa level for the Control run, there is a shift from west-southwest winds to southwest winds in the prefrontal sector on land indicative of orographic deformation (Fig. 4.16a). This feature is not as prominent in the Half-T run at the same level (Fig. 4.17a). Similarly, the only postfrontal northwesterlies that collide with the prefrontal flow in the Control run are those formed through what appears to be orographic deformation to the north of the front. The Half-T run exhibits postfrontal northwesterlies originating from cyclonic rotation. Closer to the surface at 975 hPa, flow is less westerly in direction in the Control postfrontal sector and both model runs exhibit more northerly postfrontal sectors with a more contiguous fronts as opposed to higher levels (Fig. 4.16b, 4.17b).

4.3.2 Effects of Frontal Positioning on Rainfall

Extreme rainfall in central Taiwan is predominantly focused on higher terrain (Fig. 3.8) and as such will be the focus of this section in the context of frontal placement. Figures 4.18 and 4.19 show rainfall accumulation over the next hour for the times discussed in section 4.3.1. At the start of analysis, a trait found in northern Taiwan, collocation of extreme rainfall and Mei-yu front, is captured by the Control run (Fig. 4.18a). The link is separated in central Taiwan, however, with rainfall exceeding 60 mm/hr directly east of the Mei-yu front in the CMR. The Half-T run does not have heavy rainfall in the high terrain, but rather upstream of the topography and south of the Mei-yu front (Fig. 4.19a). The rainfall may not be collocated with the front possibly owing to how difficult it is to track the front or due to rapid southern propagation of the front.

An hour later and the Half-T run now has heavy rainfall collocated with the Mei-yu front, though the rainfall is still shifted upstream of the topography (Fig. 4.19b). The Control run has extreme rainfall in the CMR to the east of the Mei-yu front at 23.8°N, but curiously, the Control front is not linear and is not contained at a single latitude (Fig. 4.18b). It appears the location of the heavier rainfall is determined by the location of the front in direct contact with the topography. This assertion is only consistent for the most extreme rainfall as lighter rainfall is spread out in location regardless of frontal placement.

In the last hour, similar characteristics remain. In the Control run, despite the front appearing to be located along 23.6°N off the western coast, closer to the terrain, the front is located just north of 23.8°N (Fig. 4.18c). In turn, not only is extreme rainfall in the next hour aligned with 23.8°N, but little to no rainfall is observed along 23.6°N, further supporting that the placement of the front off the coast is not directly controlling rainfall location and intensity in the terrain. In the Half-T run, the same observation can be made, but because the front is near zonally oriented, rainfall aligns along a single latitude (Fig. 4.19c).

At each hour, a common thread remains with extreme rainfall being found to the east of the Mei-yu front's location in direct contact with the CMR. As such, the implications

this has on intensity and duration of rainfall are similar to findings in northern Taiwan. The intensity of rainfall is linked with steep topography and frontal location. Although the strength of the fronts may be similar between the model runs, the steeper topography in the Control run will lead to greater orographic lift than the Half-T run. Duration is tied to the propagation speed of the Mei-yu front. In the Half-T run, the strong postfrontal northwesterlies with a more westerly prefrontal sector acts to increase frontal propagation speed, thereby decreasing rainfall duration in a given location. The Control run experiences the opposite with the weak postfrontal northwesterlies formed through suspected orographic deformation colliding with a more southerly prefrontal sector, slowing frontal propagation and increasing rainfall duration at a given location.

4.3.3 Verification of Orographic Deformation

To validate assumptions of orographic deformation in the prefrontal and postfrontal sector, cross sections are taken from off the coast toward the CMR on both sides of the Mei-yu front (Fig. 4.20, 4.21). The utility of using the cross sections is that orographic blocking can occur at different levels, at different distances upstream of the topography, and these levels and distances may differ depending on what side of the front is being analyzed. The cross-front difference in orographic blocking is most apparent due to the different maximum terrain heights of the SMR in the postfrontal sector and the CMR in the prefrontal sector. In viewing the zonal wind of the prefrontal sector, both model runs exhibits similar wind speeds under 0.5 km ASL, but above that level, the Half-T run is approximately 10 ms^{-1} faster than the control run (Fig. 4.20c, d). A consequence of this difference, along with the differences in terrain height, is that the blocking height, as viewed through the zonal, altitude relative Froude number, is significantly higher in the prefrontal sector of the Control run relative to the Half-T run (Fig. 4.20a, b). For much of the Control prefrontal sector, the blocking height is near 2.5 km whereas much of the Half-T sector is only blocked up to 0.5 km with regions close to the terrain being unblocked.

Zonal wind speeds in the prefrontal and postfrontal sectors are similar above 1 km ASL,

but beneath that level, both model runs have postfrontal easterly flow in the west turning into westerly flow in the east indicative of the counterclockwise turning (Fig. 4.21c, d). The wind speeds in this level are not all that dissimilar between the Half-T and Control run; therefore, the differences in Froude number are likely attributed to the differences in terrain height. In comparing the blocking heights in the prefrontal and postfrontal sectors, the Control run has a higher blocking height in the prefrontal sector whereas the Half-T run has a higher blocking height in the postfrontal sector. Therefore, a reason why the Control front has a slower propagation speed is because of stronger conversion of westerly flow to northerly flow via orographic blocking in the prefrontal sector.

When viewing the Mei-yu front along a meridian, differences in the prefrontal and postfrontal sectors are more striking (Fig. 4.22). The gradient in zonal and meridional wind speeds found near 23.85°N indicates the approximate location of the Mei-yu front. Differences in these gradients among model runs also manifests in how sharp of a cross-front isentropic gradient exists given the Control gradient is much sharper than the Half-T gradient at low levels. In the prefrontal sectors, zonal winds are approximately 10 ms^{-1} weaker in the Control run compared to the Half-T run throughout all levels, consistent with stronger orographic blocking (Fig. 4.22a, b). For comparison, the postfrontal sectors only differ by 5 ms^{-1} in comparison, but the Control run has near stagnant flow near the surface that is absent the Half-T run. The steeper terrain in the Control run leads to more complex meridional winds along this cross section relative to the Half-T run (Fig. 4.22c, d). The wind speeds of the prefrontal southerlies in direct contact with the front are relatively similar, however. Winds in the Control run's postfrontal sector clearly illuminate orographic deformation near 24.15°N (Fig. 4.22c). This relationship can be assumed because of northerlies to the south, southerlies in the north, and positive vertical velocity found at the gradient between the two. In contrast, the entirety of the Half-T postfrontal sector is weakly northerly (Fig. 4.22d). Interestingly, there is a strong postfrontal northerly flow relative to the other northerlies in the postfrontal sectors just north of the Control front that seems to be not connected to northerlies that form from

orographic deformation.

A limitation of the cross sections are the limited spatial context they give. The post-frontal sector of the Control run alone is complex with winds flowing in multiple directions prior to converging along the front. A component that is left out when using cross sections outside of the front is propagation of parcels along the Mei-yu front. Some of the strongest frontal convergence is found off the western coast with westerly components on both sides of the front. It is possible that propagation of the Mei-yu front is controlled by westerly winds just at the frontal interface in proximity to the CMR. To determine if this is possible and if orographic deformation is found outside of the cross sections, a similar RIP trajectory analysis to that in northern Taiwan (Section 4.2.3) was performed. For this analysis, parcels were released along the 120.75°E meridian at the frontal interface in both the prefrontal and postfrontal sectors as represented by the black dots in Figure 4.22. The choice of 120.75°E was made due to it being the closest to the topography with an identifiable front in both model runs. Release heights varied from 400 – 800 m ASL. To capture the origin of parcels, a 6-hour backwards trajectory was run, and to determine if the origin of the parcels has an impact on lifting potential, a 4-hour forward trajectory was also run with the backward and forward trajectories stitched together at 120.75°N.

Starting with the lifting of parcels, it is difficult to discern differences in parcels released in the Control run compared to those released in the Half-T run (Fig. 4.23b, 4.24b). On approach to the release point within the backwards trajectories, parcels do not originate from higher levels nor do they encounter significant lifting or descent. After passing the release point, parcels lift via orographic lift along the CMR resulting in a spread in ending heights between 2-14 km ASL. The largest difference between model runs is the longitude at which they encounter the most lift with the Control run having most parcels lifting from the release point to 121.25°N whereas the Half-T run has most parcels lifting from the release point to 121°N. Another distinction is the difference in maximum lift achieved relative to release height. The Control run has the most lift achieved by parcels released below 800 m while the Half-T run has all parcels released at 800 m reaching altitudes above

7.5 km. Beyond those differences, trajectories in each model run have similar packets of origin heights and ending heights.

When viewing the horizontal paths that parcels take in the backwards trajectories, a few differences stand out (Fig. 4.23a, 4.24a). Parcels released in the prefrontal sector are inferred as originating southwest of the release point, far upstream. This pattern is shared among both model runs indicating that the prefrontal sectors are relatively the same between model runs. Parcels that are not clearly originating in the prefrontal sector, however, have different paths between the model runs. The parcels in the Control run originating to the northwest of the release point with predominantly eastward propagation (Fig. 11a) sharply clockwise turn occurs before reaching the release point, providing evidence of orographic deformation. Once at the release point, parcels become westerly along the front, lift above the CMR, and advect eastward. Somewhat like the Control run, a majority of these parcels in the Half-T run originate to the west northwest of the release point (Fig. 4.24a), though notably, significantly farther west than the Control run. The parcels also turn clockwise into the release point before becoming westerly, rising above the CMR, and propagating east.

Seeing as parcels not originating in the prefrontal sector turn clockwise to reach the release point regardless of model run, it can be difficult to determine if the turning is due to orographic deformation. Although previously it was determined that the postfrontal sector in the Control run is more suitable for orographic blocking as seen through the Froude number, the Half-T run was still blocked below 0.75 km when westerly wind was present (Fig. 4.21b). Therefore, modification of the Froude number to a Lagrangian form is developed to determine if a parcel experiences orographic blocking:

$$Fr(x, y, z, t) = \frac{\bar{U}(x, y, z, t)}{N(x, y, z, t)[H_{max}(t) - z(t)]} \tag{4.7}$$

At any given time and location, a parcel will have a characteristic Brunt–Väisälä frequency, height, wind speed, and wind direction. Using a cross section aligned with the wind direction, a maximum terrain height along the cross section can be used for the Froude

number calculations. These cross sections are made at every time step of a parcel's path prior to summiting the CMR to create a Lagrangian Froude number (Fig. 4.25).

The result of this framework is shown in Figure 4.26 where regardless of origin point, the Control parcels are almost always blocked as indicated by Froude numbers less than 1 whereas the Half-T parcels are almost always unblocked. This result indicates that in the Half-T run, any turning is not due to orographic blocking. The Control parcels are almost all blocked, therefore supporting that orographic deformation contributes to turning. For these reasons, it is likely that parcels originating north of the release point in the Control run are originating in the postfrontal sector. Non-prefrontal parcels in the Half-T run can not definitively be originating in the postfrontal sector, as they may be deforming along the front far upstream and being carried by strong westerly motion at the frontal interface as the front propagates south.

In summary, with a decrease in terrain height, the Half-T run exhibits less intense and lower duration rainfall in the steeper terrain of central Taiwan. The differences in intensity could be attributed to greater orographic lift in the Control run, but trying to understand the differences in duration are more complex. A proposed reason for higher duration of rainfall in the Control run is due to a slow down of the Mei-yu front's southern propagation. A parallel with northern Taiwan is that heavier rainfall is collocated with the front, but heavier rainfall is also correlated downstream of the front's location in proximity to the CMR. Therefore, by slowing the front in central Taiwan, the rainfall duration will increase where the front remains quasi-stationary. In trying to determine what causes a slower (faster) Mei-yu front in the Control (Half-T) run, two findings were made. The first being that the strength and areal coverage of northwesterly postfrontal flow pushes the front south. The second finding is that while the relative strength of prefrontal southwesterly flow is similar between model runs, the more southerly the flow is, the greater the southern propagation of the Mei-yu front. The Control run has weak northwesterly postfrontal flow that does not extend far from the CMR and is forced by orographic deformation of postfrontal westerlies. The Half-T run has stronger northwest-

erly flow in the postfrontal sector that spans beyond the coastline, acting to push the front south faster than the Control run. In the postfrontal sectors, the Control run experiences slightly greater orographic blocking which creates orographic deformation in proximity to the CMR. This deformation acts to create more southerly flow in the prefrontal sector that resists southern propagation in the Control run as opposed to the Half-T run, increasing rainfall duration.

4.4 Figures and Tables

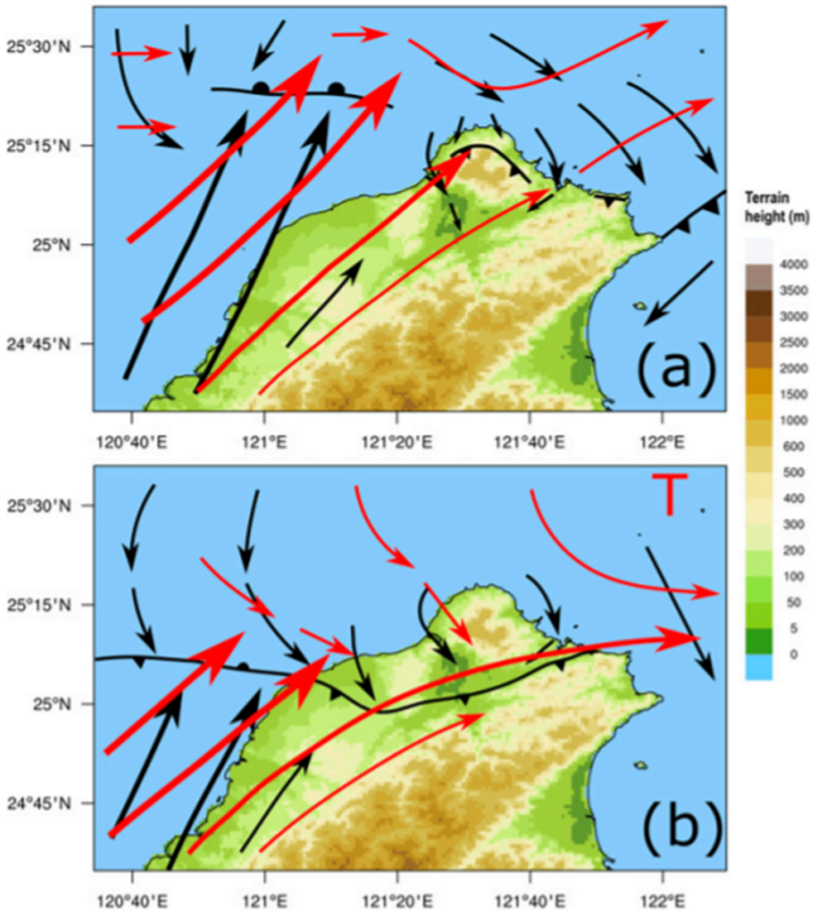

Figure 4.1: A schematic diagram shows the surface (black solid arrows) and 900 hPa (red solid arrows) flow patterns with the barrier jet (thick red solid arrows). (a) The shallow (<1 km) Mei-yu front is anchored over the northern side of the Yang-Ming Mountains for almost 8 h during the morning of 2 June 2017 (0200–1000 LST 2 June). At the 900 hPa level, the southwesterly barrier jet converges with the northwesterly flow in the southwestern flank of the Mei-yu frontal cyclone around the northern tip of Taiwan. (b) Around noontime, the Mei-yu front finally moves southward over the Yang-Ming Mountains into the Taipei basin and converges with the southwesterly barrier jet over the Taipei basin. From Tu et al. (2022).

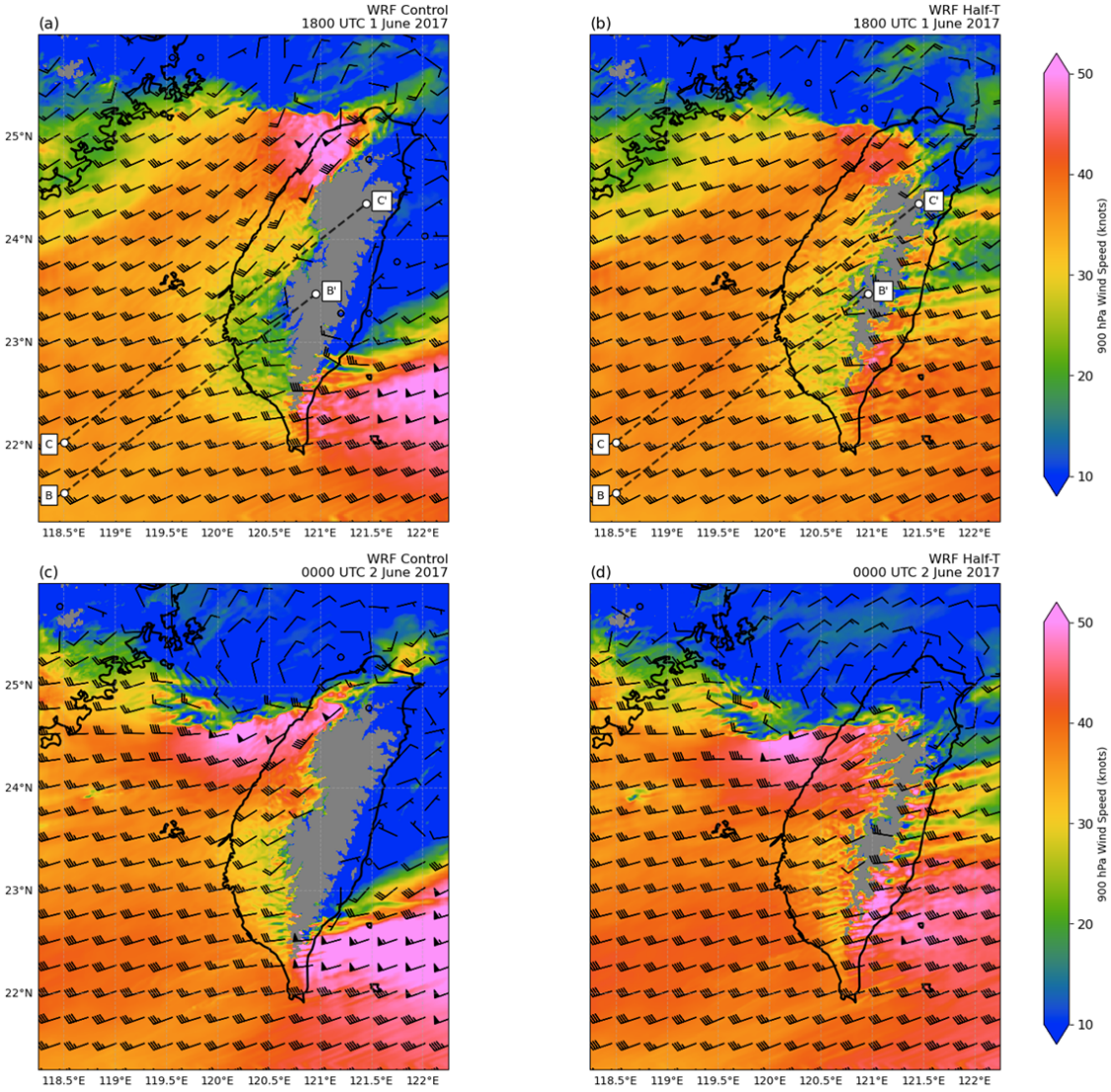

Figure 4.2: 900 hPa wind speed and wind barbs for (a, c) WRF Control and (b, d) WRF Half-T at (a, b) 1800 UTC 1 June 2017 and (c, d) 0000 UTC 2 June 2017. Cross sections are taken along lines BB' and CC' at 1800 UTC 1 June 2017.

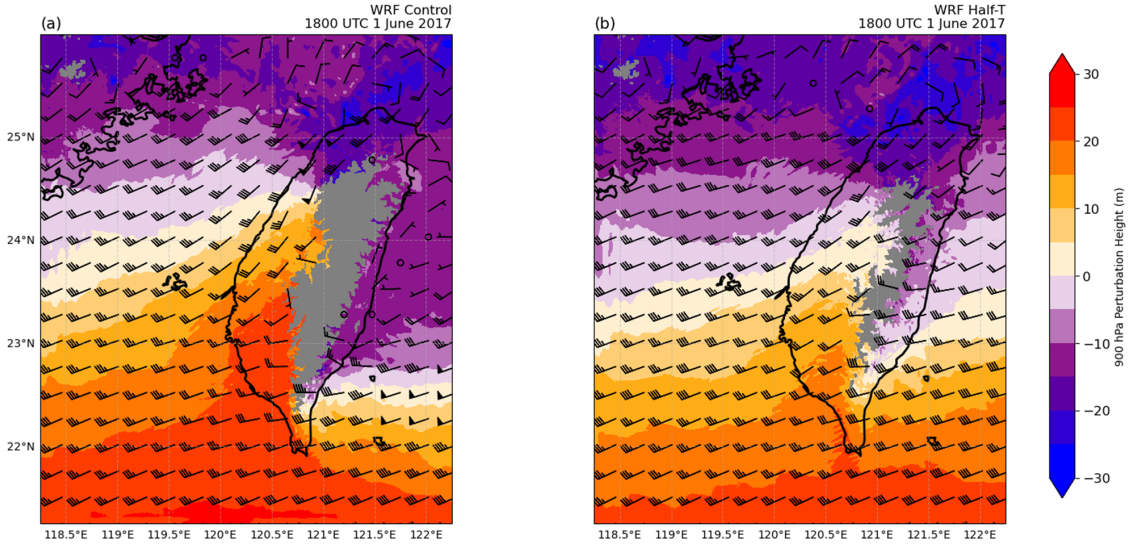

Figure 4.3: 900 hPa perturbation heights and wind barbs at 1800 UTC 1 June 2017 for (a) WRF Control and (b) WRF Half-T.

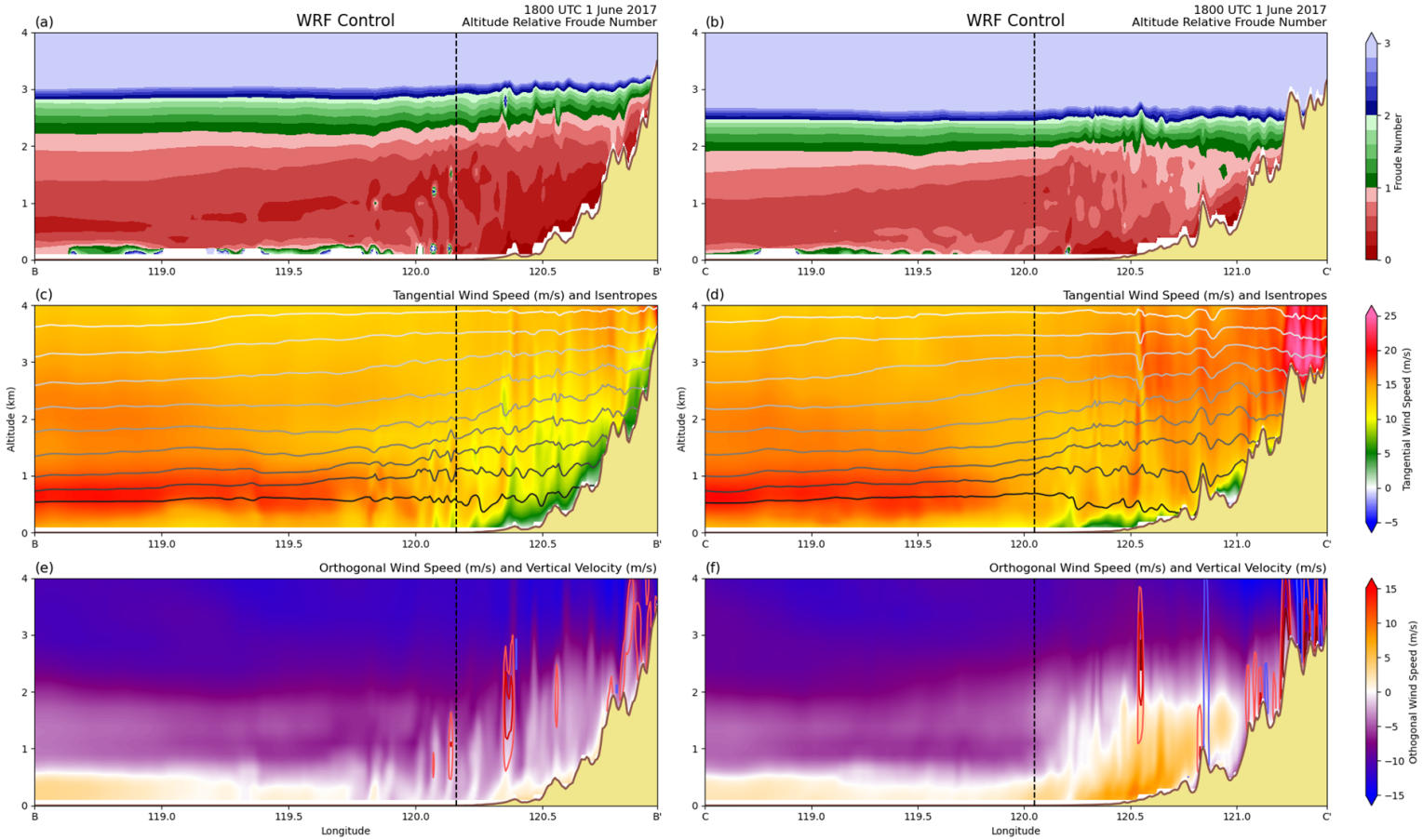

Figure 4.4: Cross sections (a, c, e) BB' and (b, d, f) CC' at 1800 UTC 1 June 2017 of (a, b) altitude relative Froude number, (c, d) tangential wind speed and dry isentropes, and (e, f) orthogonal wind speed and vertical velocity contours every 1 ms^{-1} for WRF Control. The black dashed line indicates the coastline.

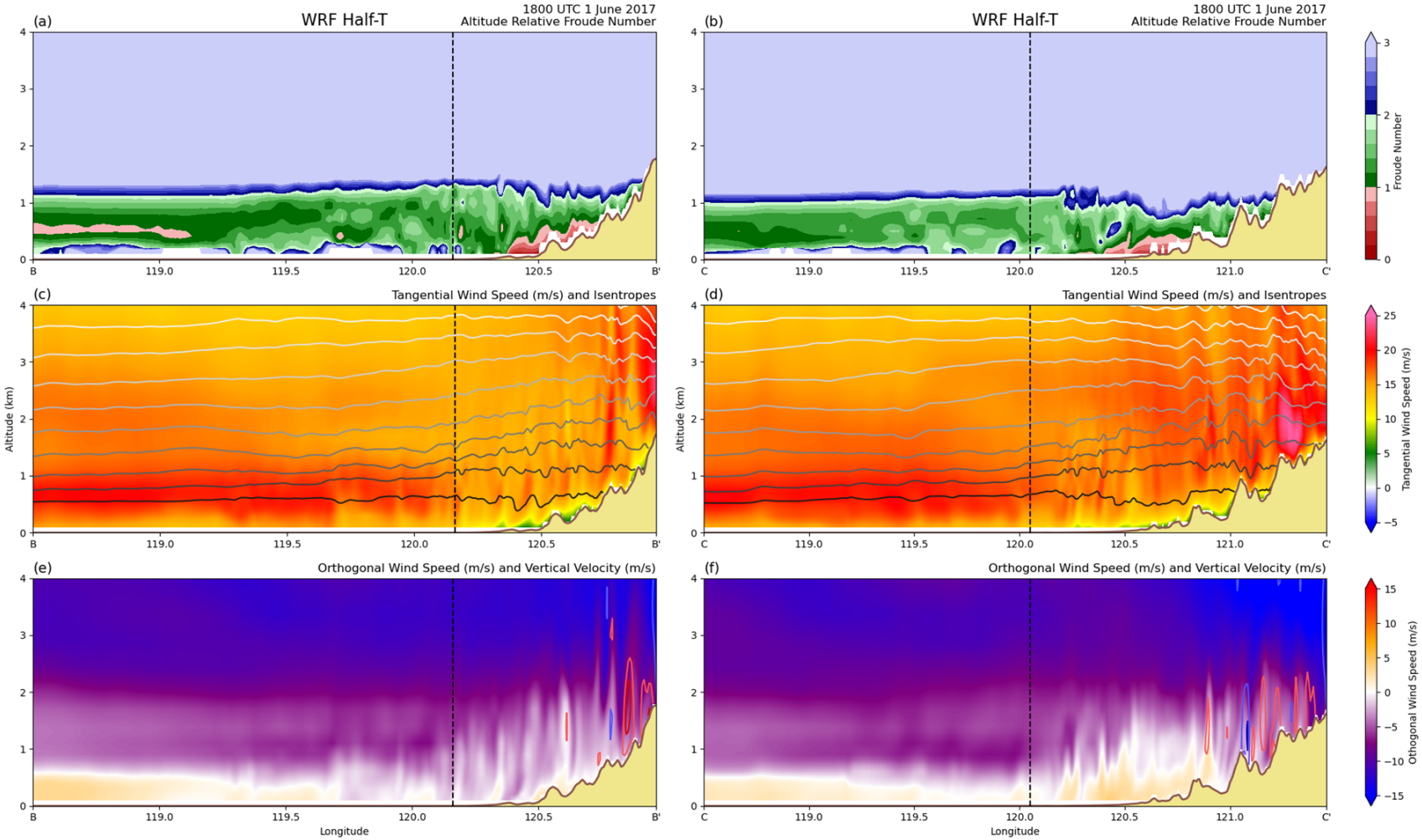

Figure 4.5: Same as Figure 4.4 but for WRF Half-T.

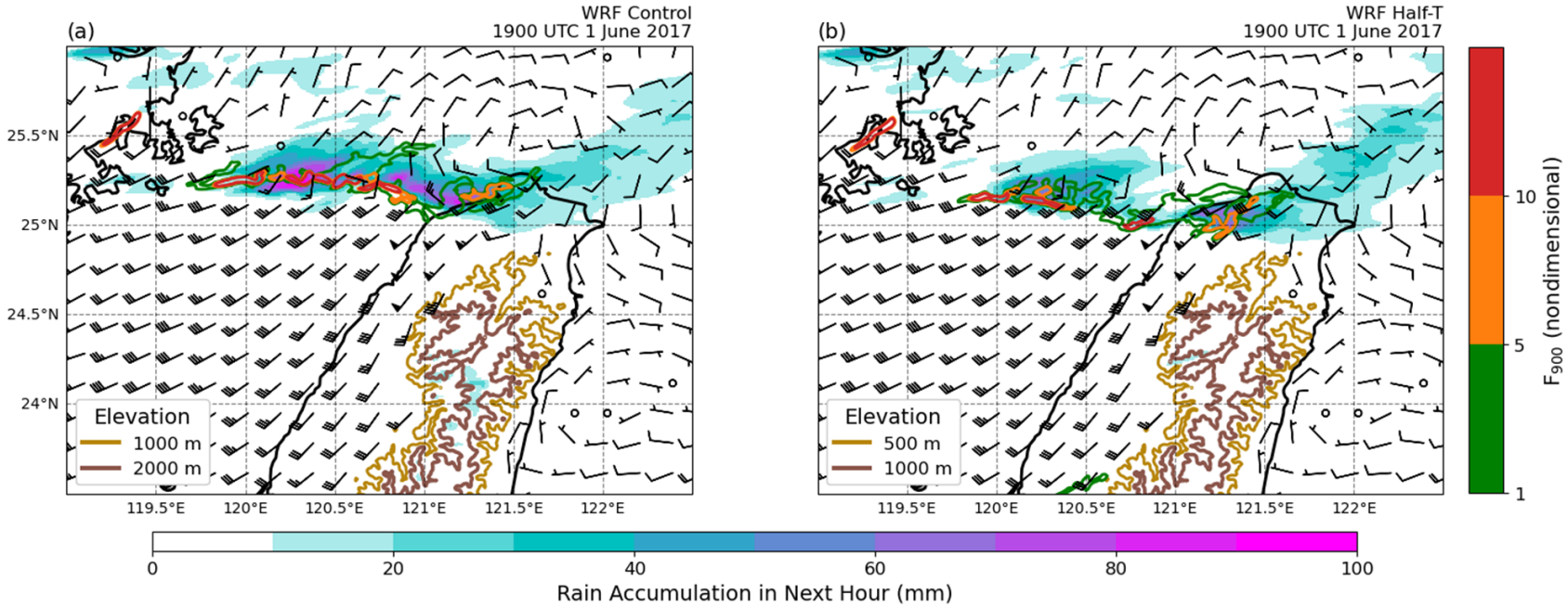

Figure 4.6: Wind barbs at 900 hPa, modified Parfitt et al. (2017) frontal diagnostic at 900 hPa, and rain accumulation over the next hour in mm at 1900 UTC 1 June 2017 for (a) WRF Control and (b) WRF Half-T.

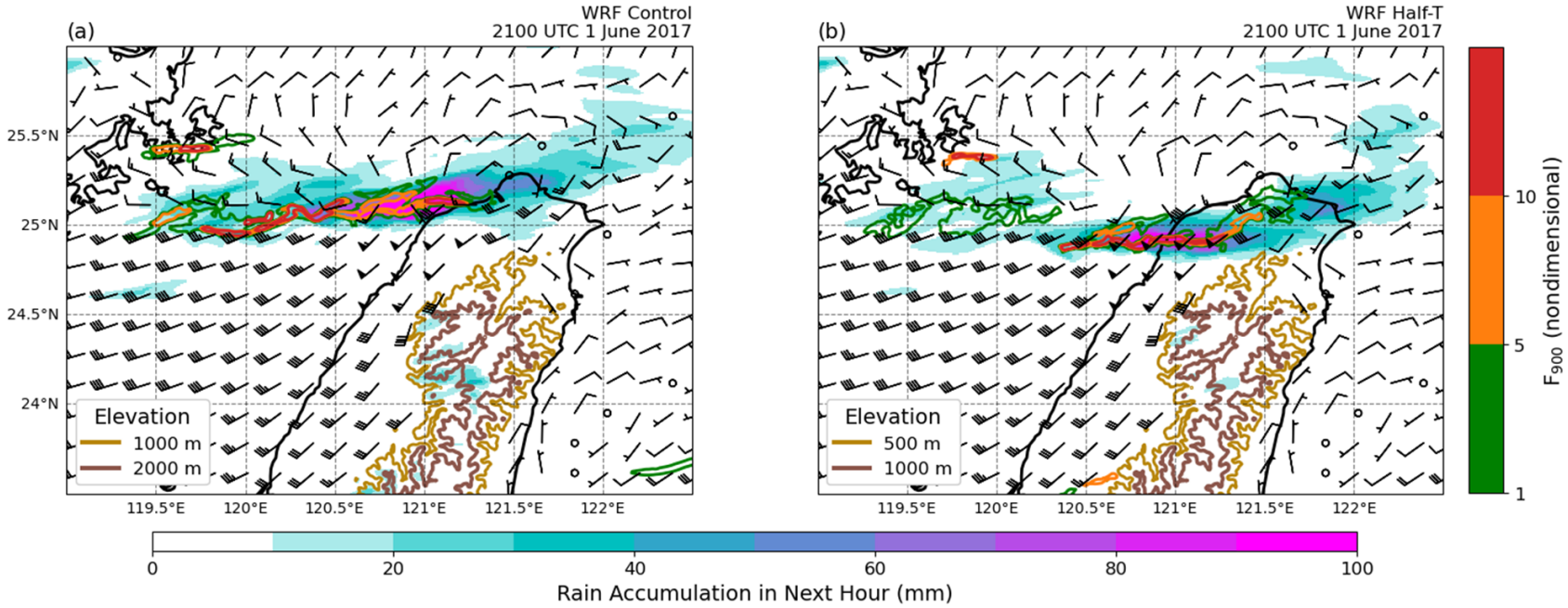

Figure 4.7: Same as Figure 4.6 but at 2100 UTC 1 June 2017.

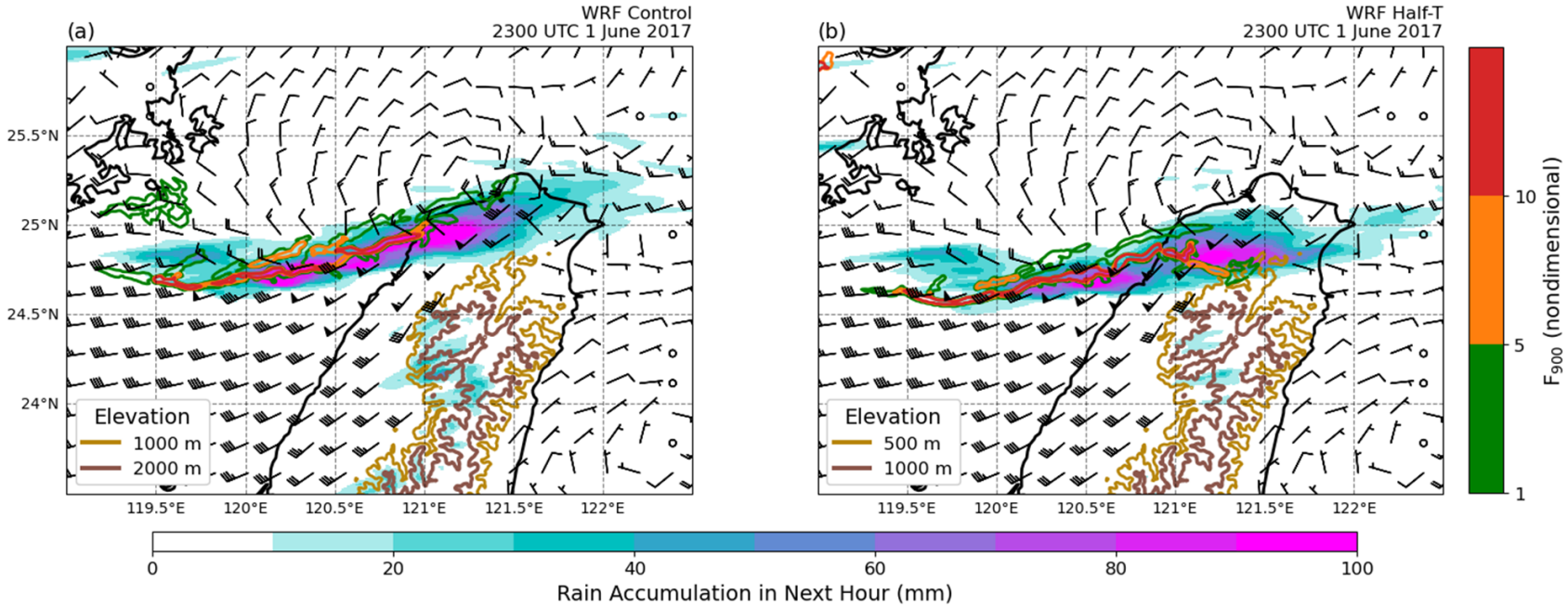

Figure 4.8: Same as Figure 4.6 but at 2300 UTC 1 June 2017.

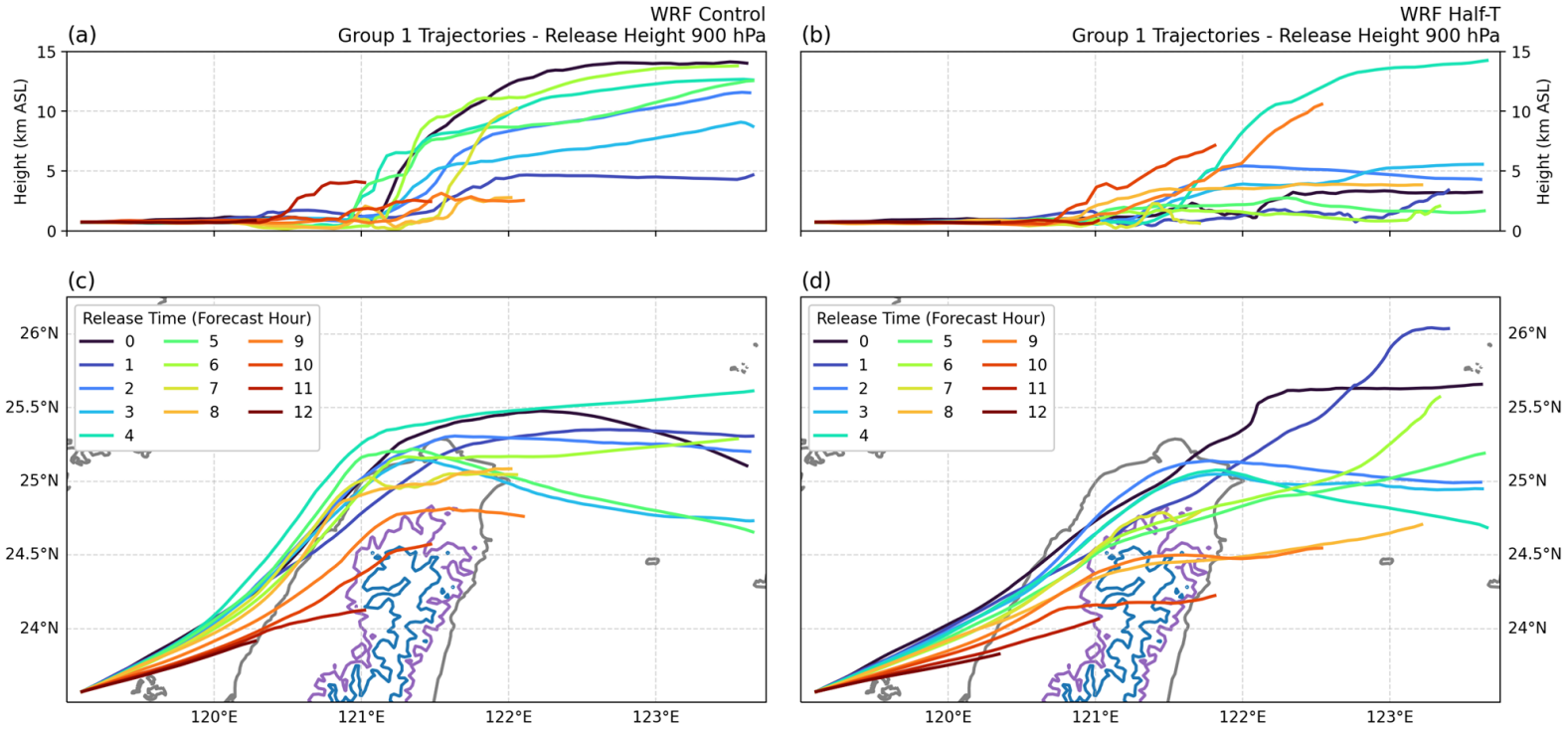

Figure 4.9: Trajectories of release group 1 released at 900 hPa for (a, c) WRF Control and (b, d) WRF Half-T. Colors correspond to the time at which trajectories were released relative to model forecast hour.

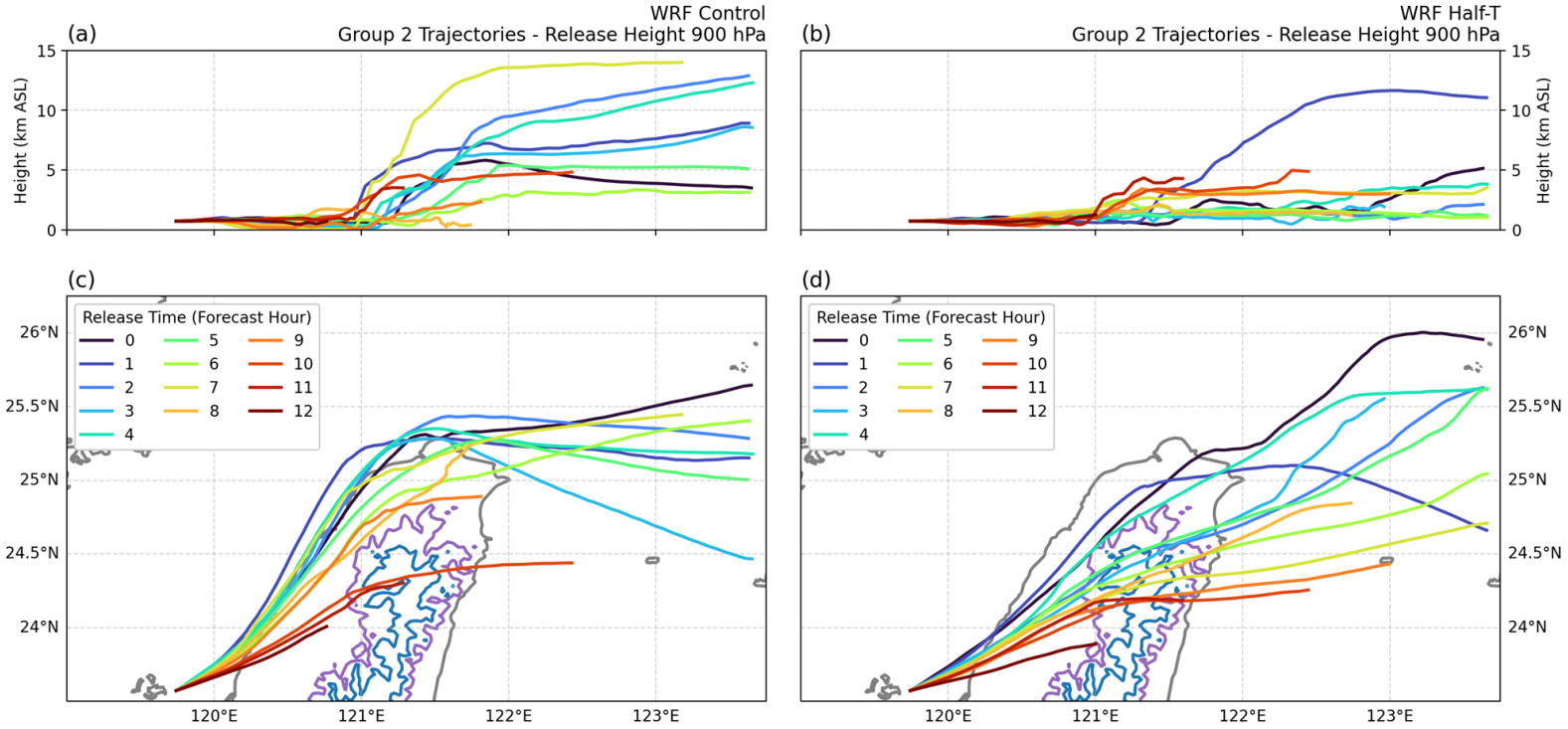

Figure 4.10: Same as Figure 4.9, but for release group 2.

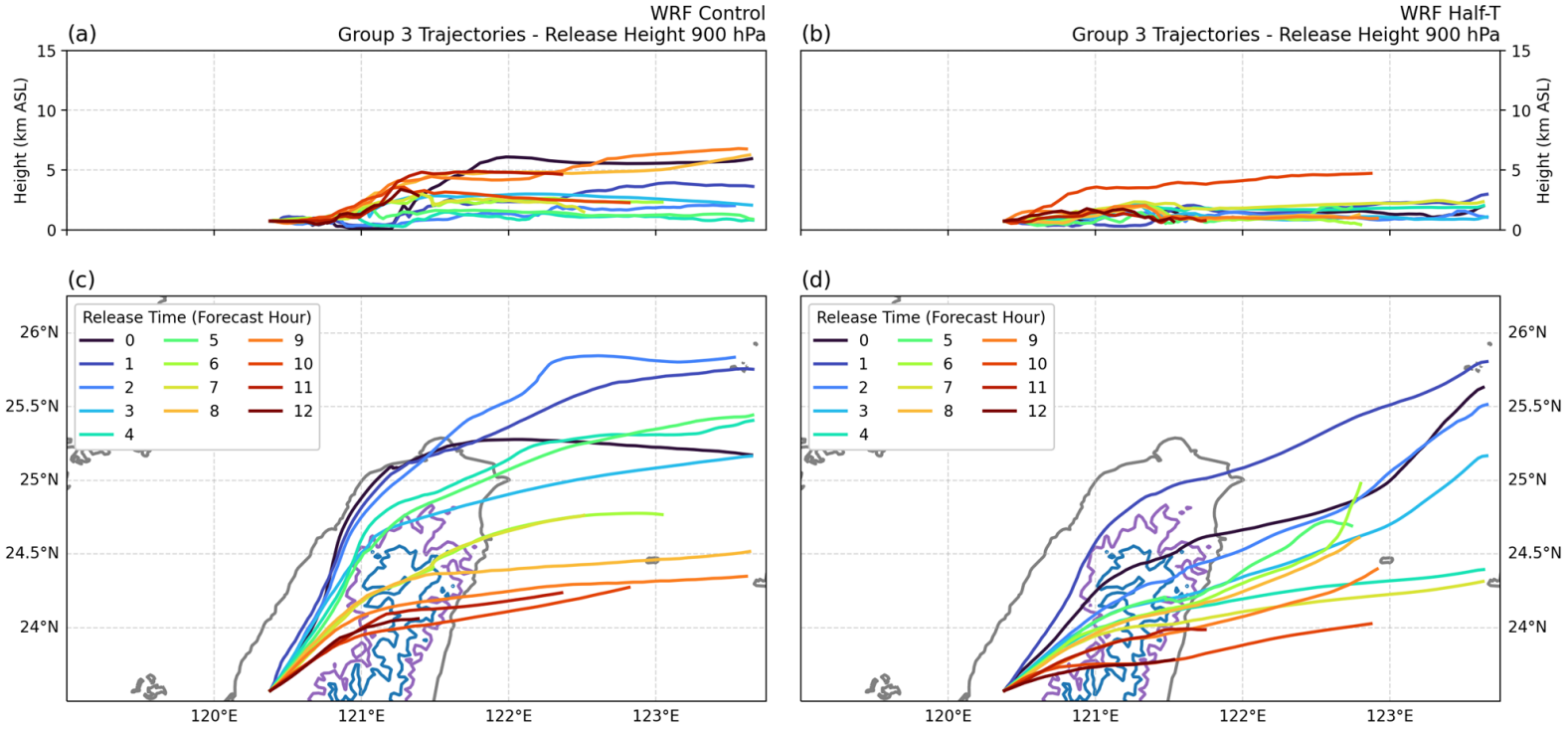

Figure 4.11: Same as Figure 4.9, but for release group 3.

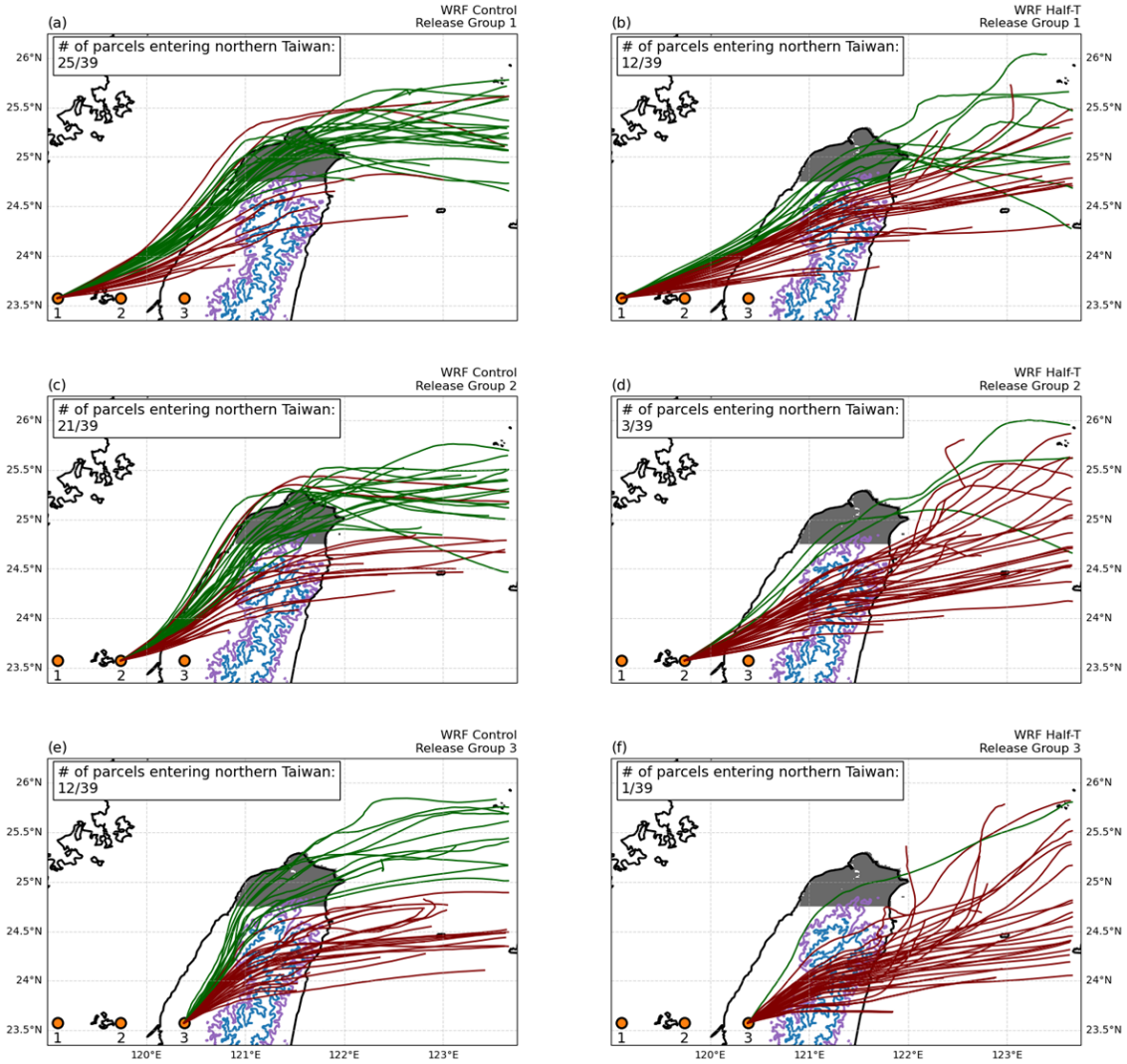

Figure 4.12: Trajectories released at 875, 900, and 925 hPa for (a, c, e) WRF Control and (b, d, f) WRF Half-T from (a, b) release location 1, (c, d) release location 2, and (e, f) release location 3. Green(red) trajectories indicate parcels that do (do not) enter northern Taiwan as indicated by the grey region bound between 24.75°N and the northern coastline.

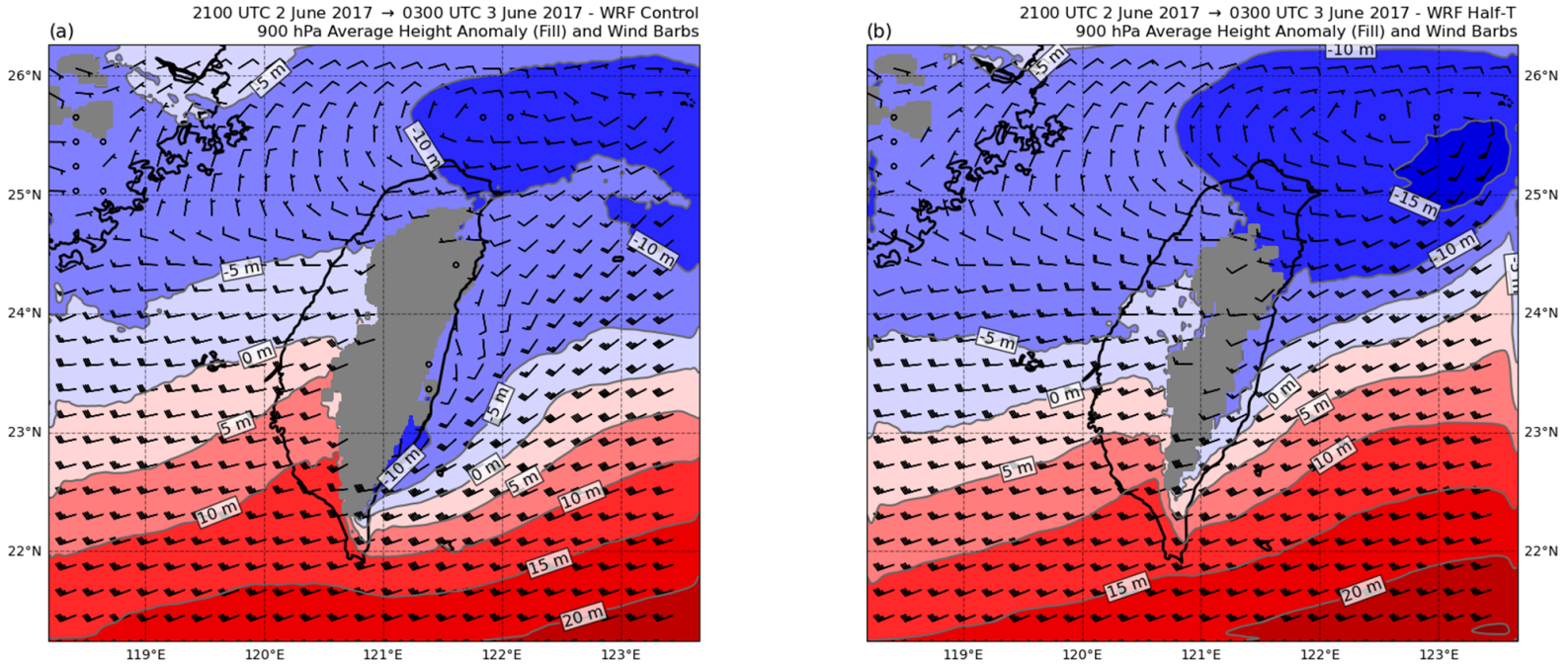

Figure 4.13: Average 900 hPa geopotential height anomaly and average wind barbs between 2100 UTC 1 June 2017 – 0300 UTC 2 June 2017 for (a) WRF Control and (b) WRF Half-T.

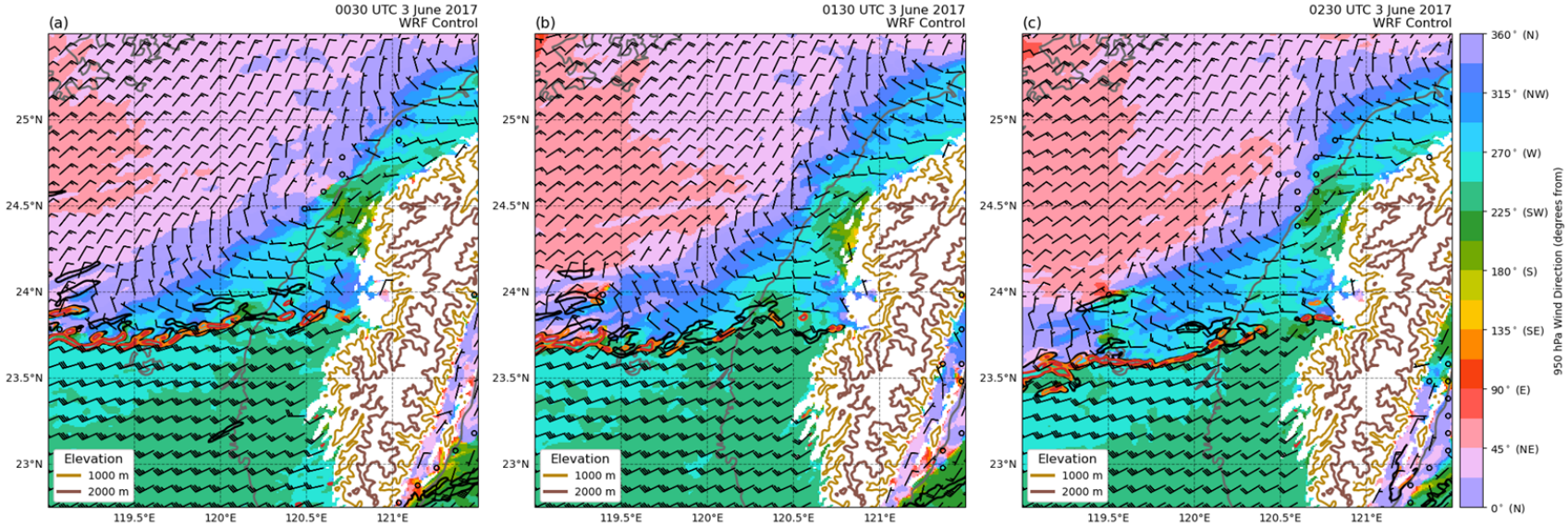

Figure 4.14: 950 hPa wind direction (Fill), Parfitt et al. (2017) frontal diagnostic (Contour), and wind barbs for WRF Control at (a) 0030 UTC 3 June 2017, (b) 0130 UTC 3 June 2017, and (c) 0230 UTC 3 June 2017.

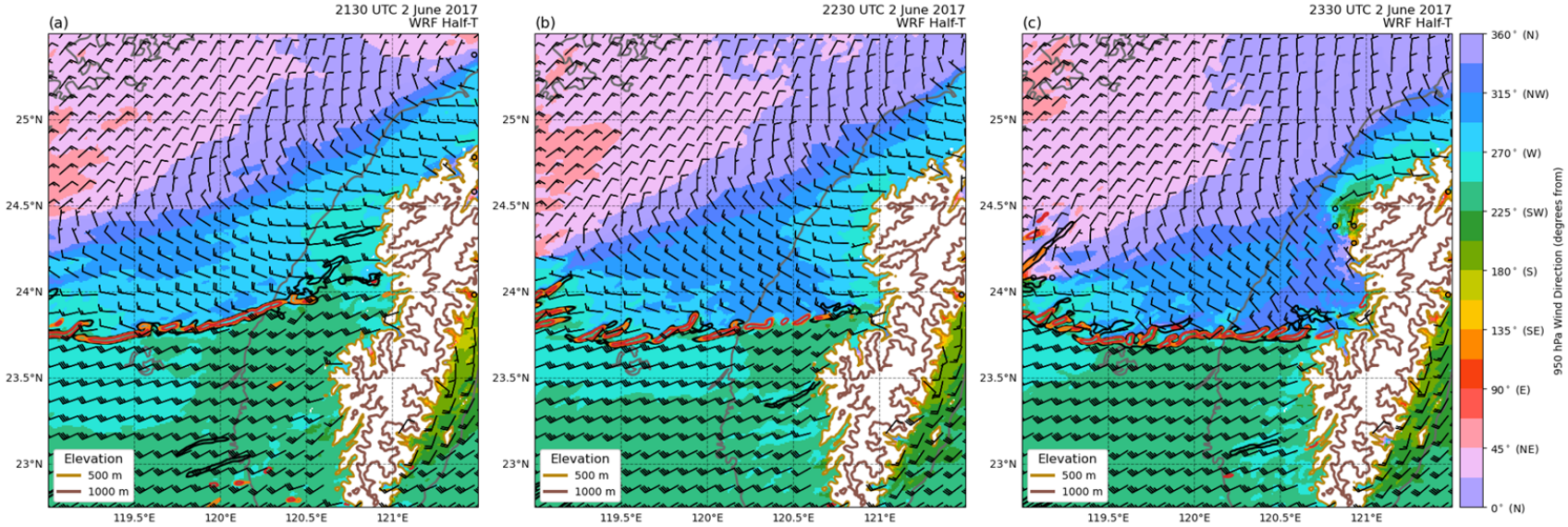

Figure 4.15: Same as Figure 4.14, but for WRF Half-T at (a) 2130 UTC 2 June 2017, (b) 2230 UTC 2 June 2017, and (c) 2330 UTC 2 June 2017.

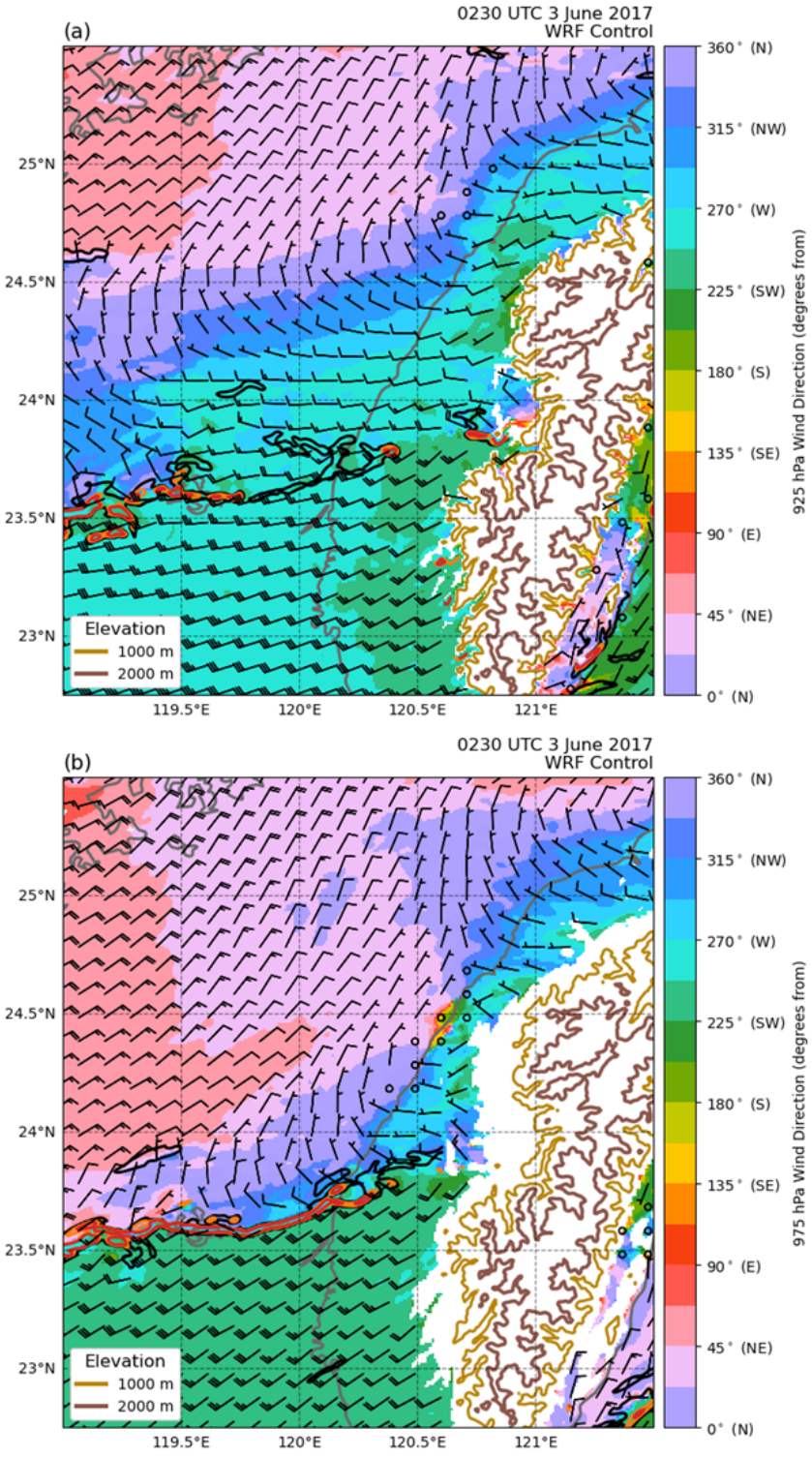

Figure 4.16: Same as Fig. 4.14c, but at (a) 925 hPa and (b) 975 hPa.

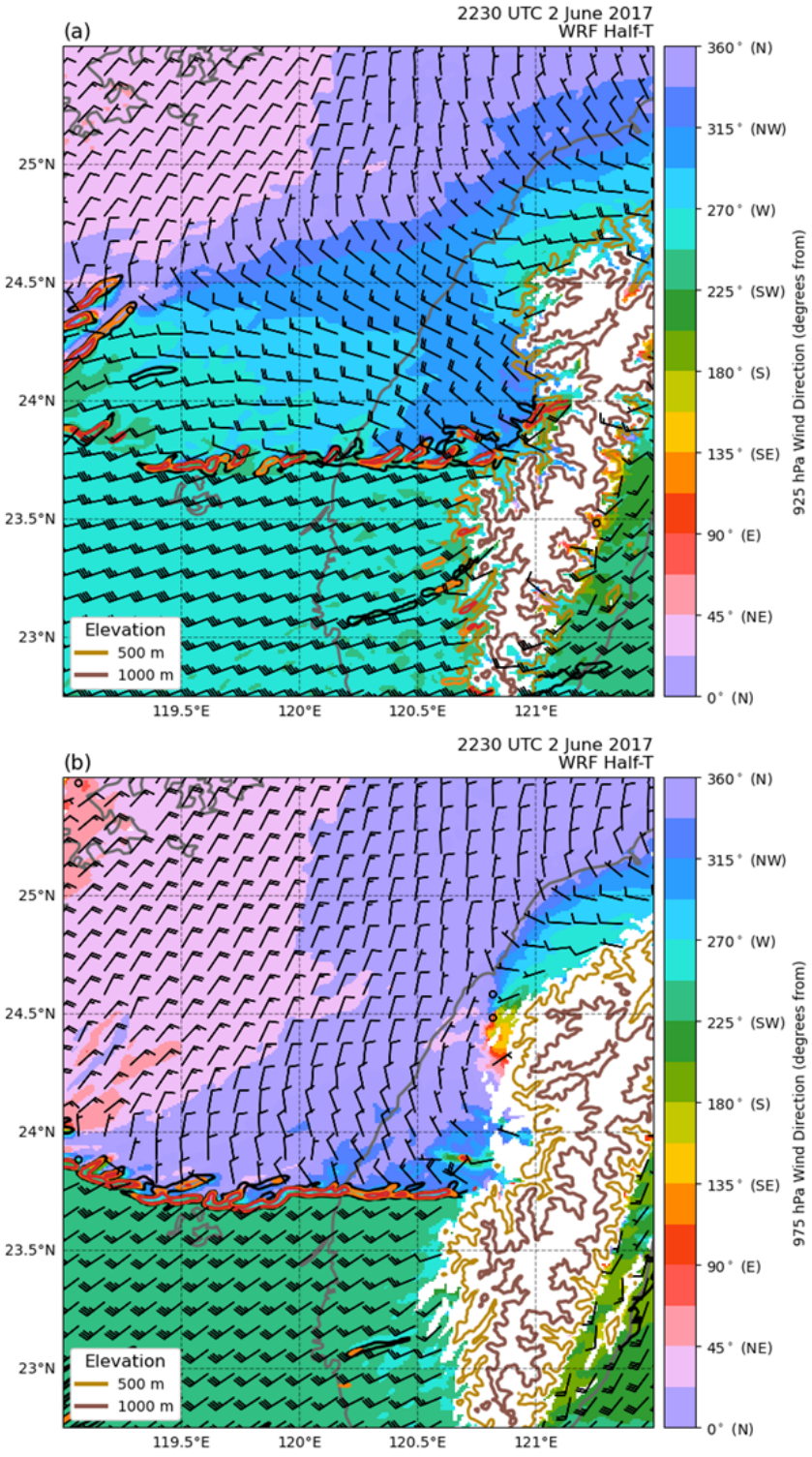

Figure 4.17: Same as Fig. 4.15c, but at (a) 925 hPa and (b) 975 hPa.

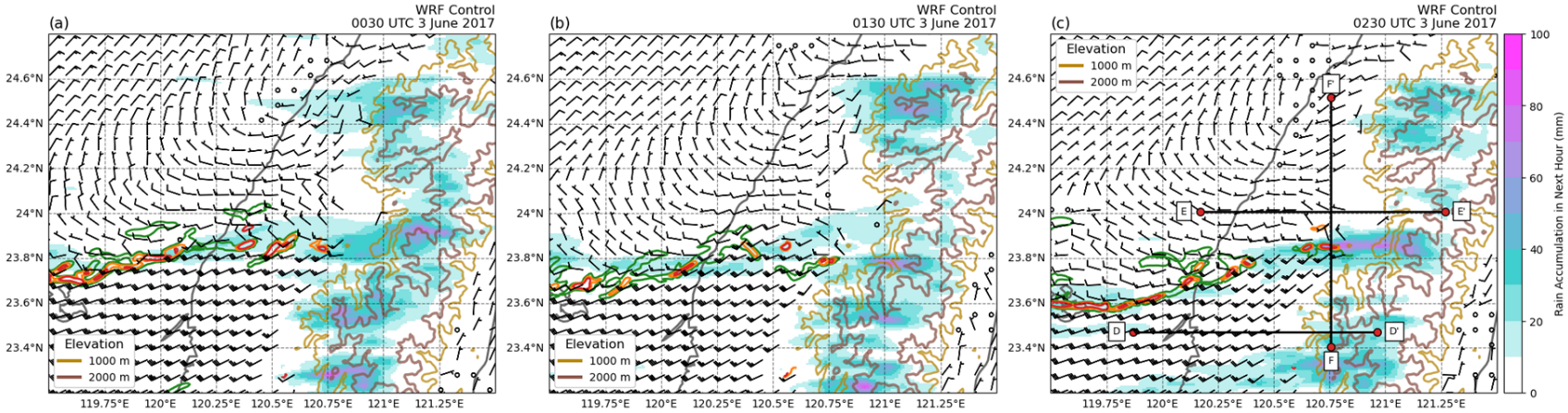

Figure 4.18: Same as Figure 4.14, but with rainfall accumulation in mm over the next hour (Fill). Lines in (c) represent cross sections used in Figures 4.20, 4.21, and 4.22.

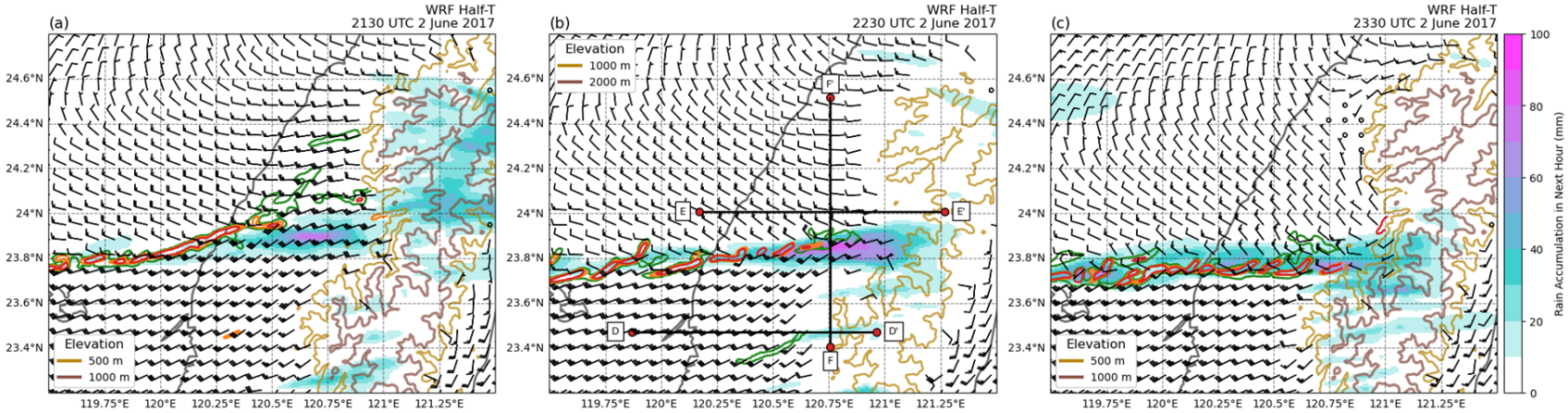

Figure 4.19: Same as Figure 4.15, but with rainfall accumulation in mm over the next hour (Fill). Lines in (b) represent cross sections used in Figures 4.20, 4.21, and 4.22.

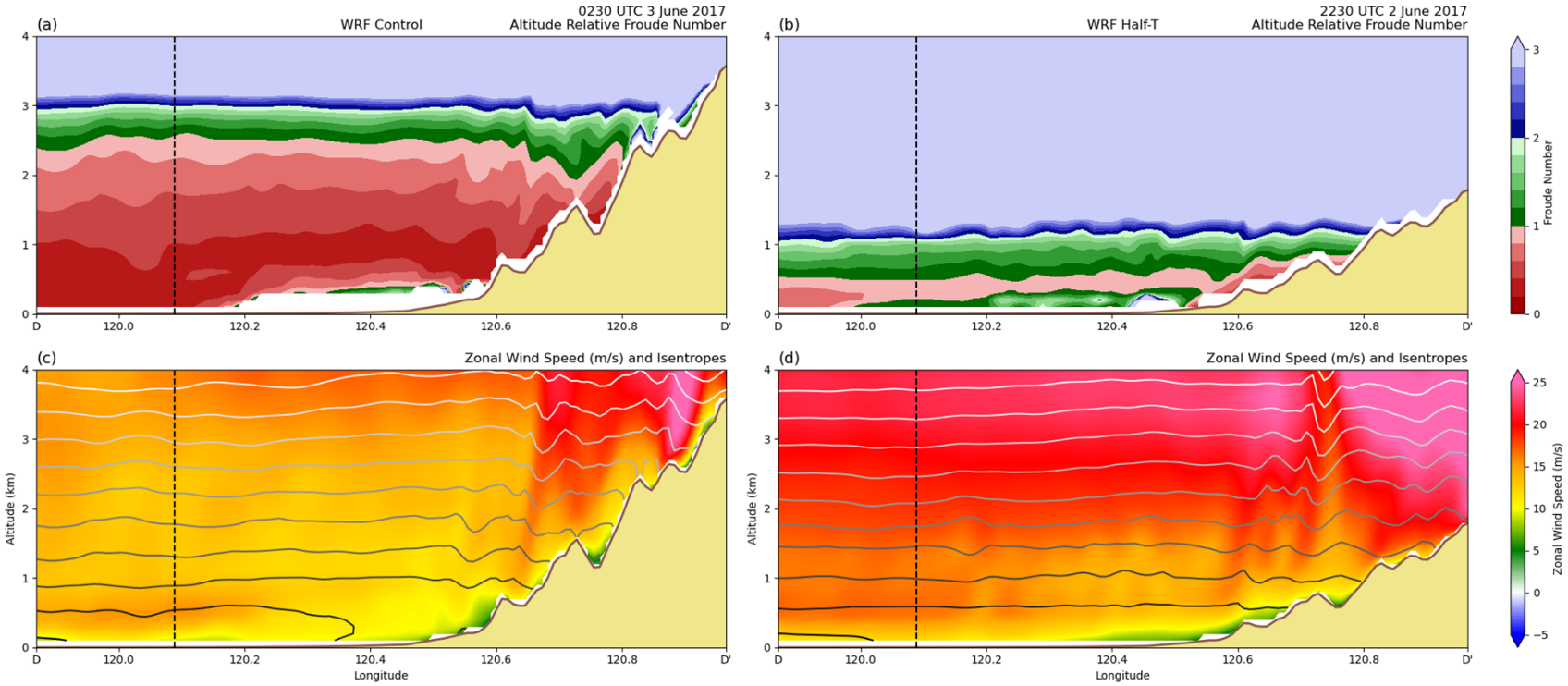

Figure 4.20: Zonal cross sections along DD' in (a, c) Figure 4.18 and (b, d) Figure 4.19. (a, b) represent zonal cross sections of height-relative Froude number and (c, d) represent zonal cross sections of zonal wind speed with dry isentropes. The dashed black line indicates the coastline.

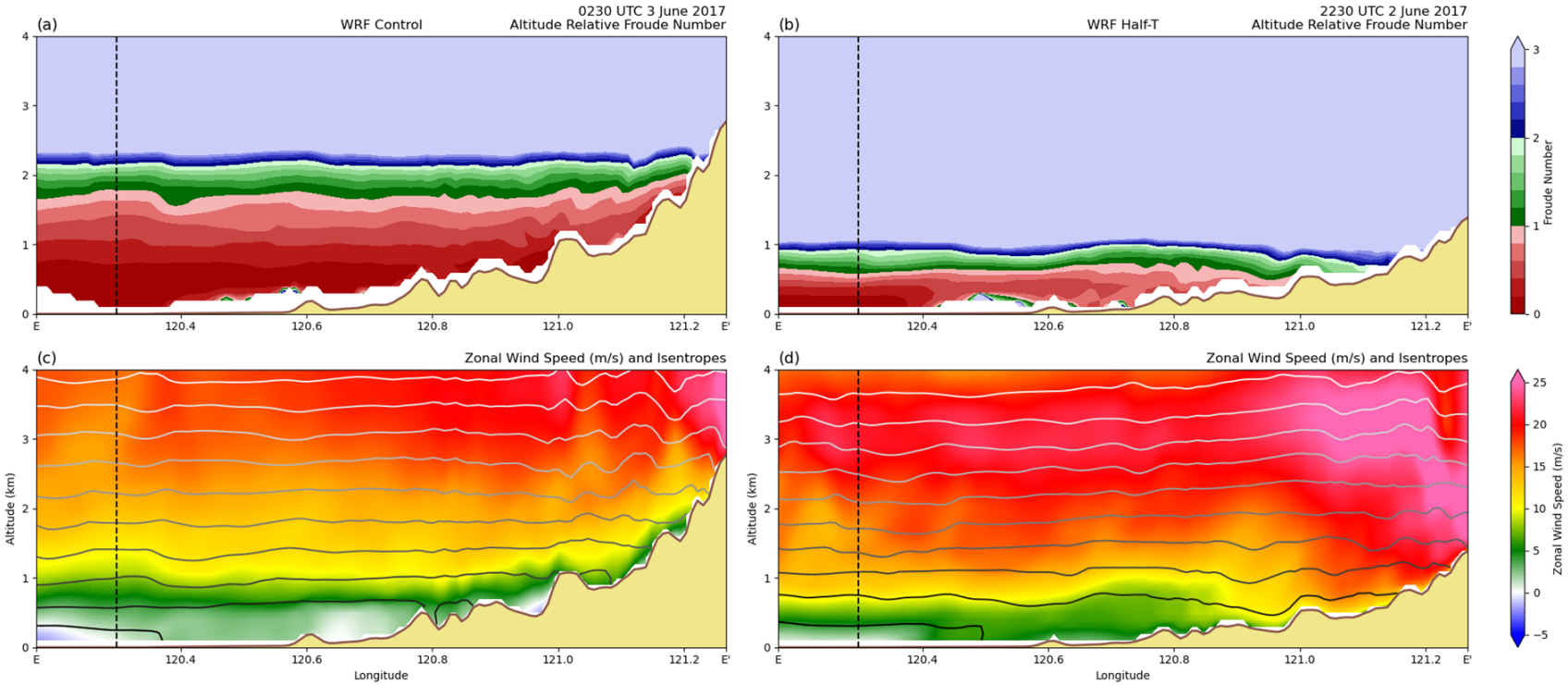

Figure 4.21: Same as Figure 4.20, but for cross section EE' in (a, c) Figure 4.18 and (b, d) Figure 4.19.

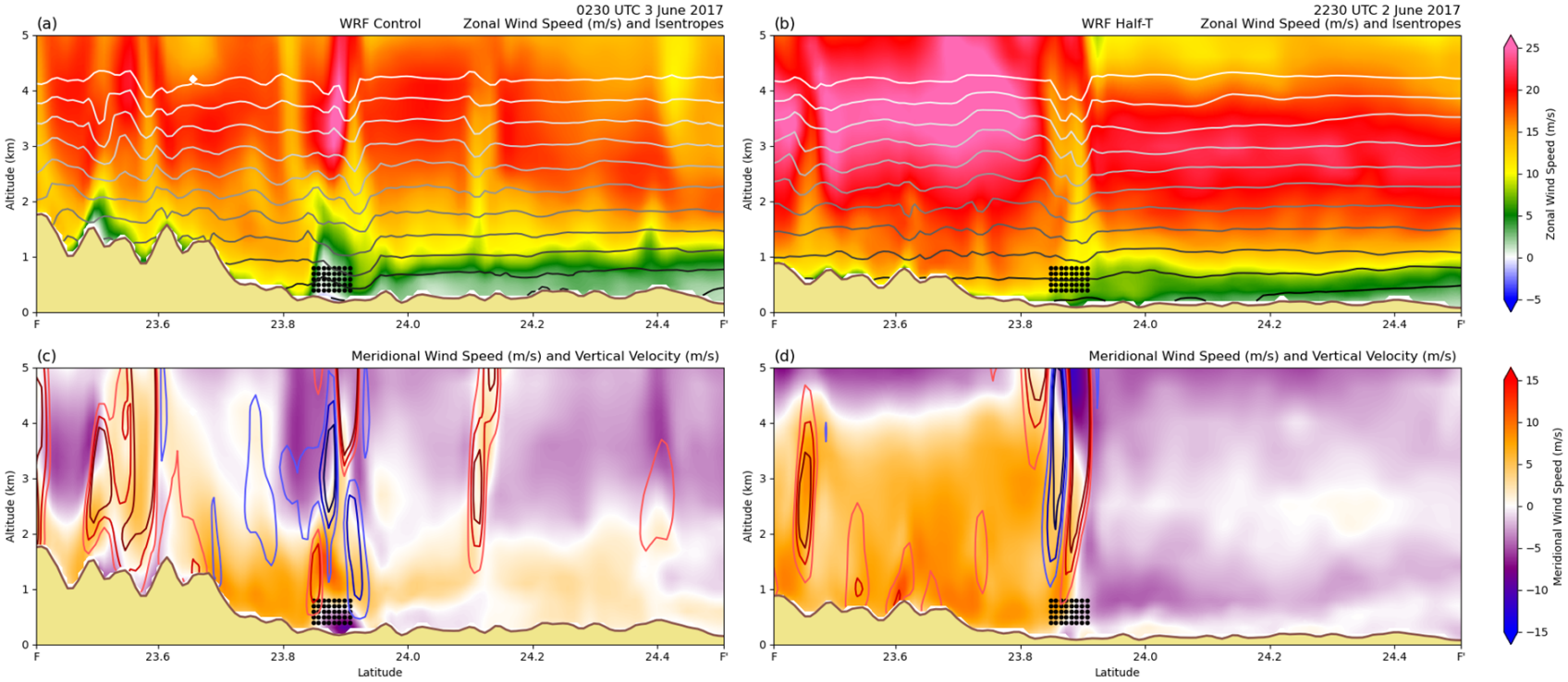

Figure 4.22: Meridional cross sections along FF' in (a, c) Figure 4.18 and (b, d) Figure 4.19. (a, b) represent meridional cross sections of zonal wind speed with dry isentropes and (c, d) represent meridional cross sections of meridional wind speed with vertical velocity. The array of dots represent the trajectory release locations in Fig. 4.23, 4.24, and 4.26

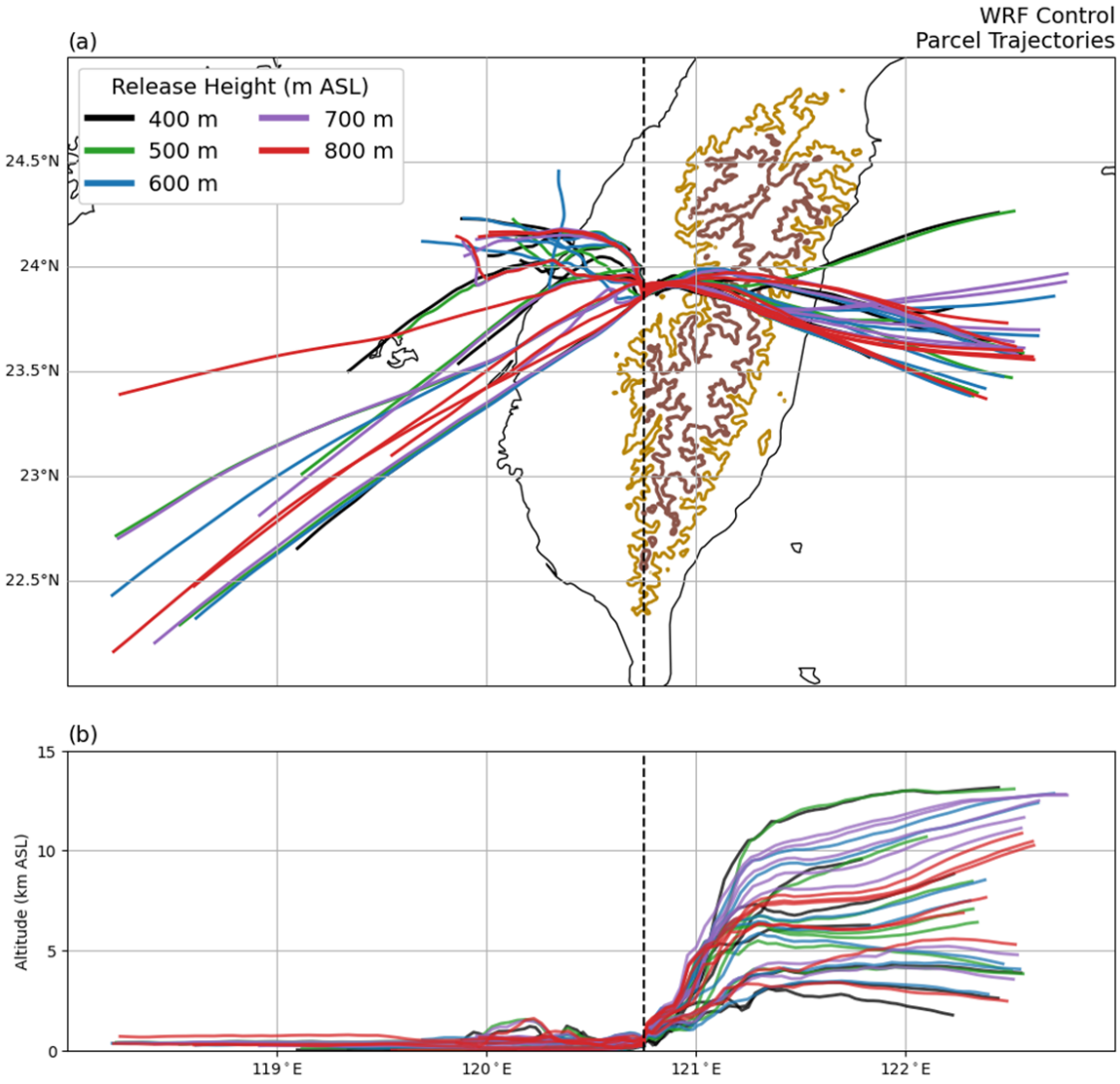

Figure 4.23: Trajectory paths for release locations in Figure 4.22 for WRF Control in the (a) X-Y plane and (b) X-Z plane. The dashed line indicates the "stitched" release points whereby lines to the west represent backwards trajectories and lines to the east represent forwards trajectories.

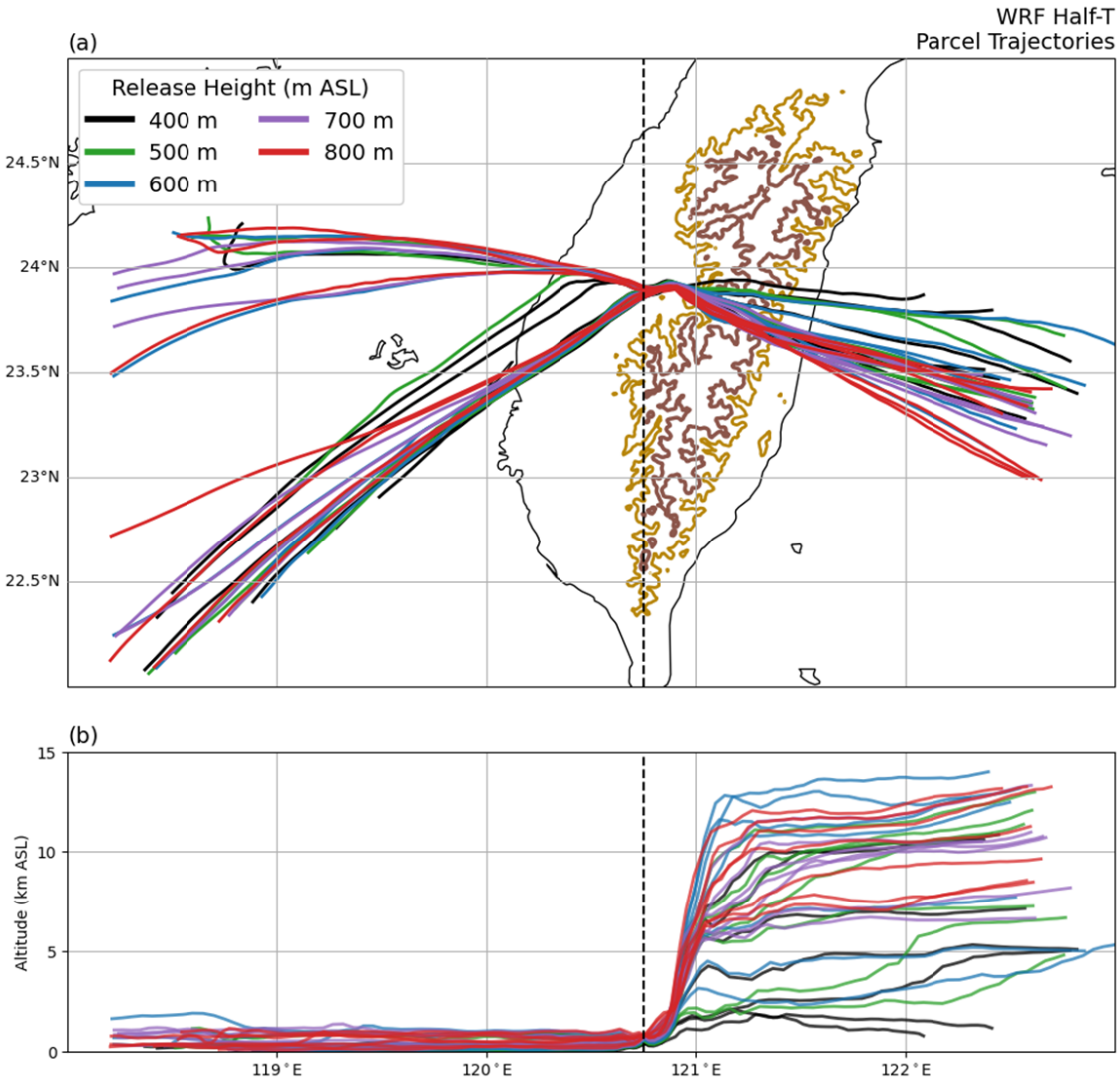

Figure 4.24: As in Fig. 4.23, but for WRF Half-T.

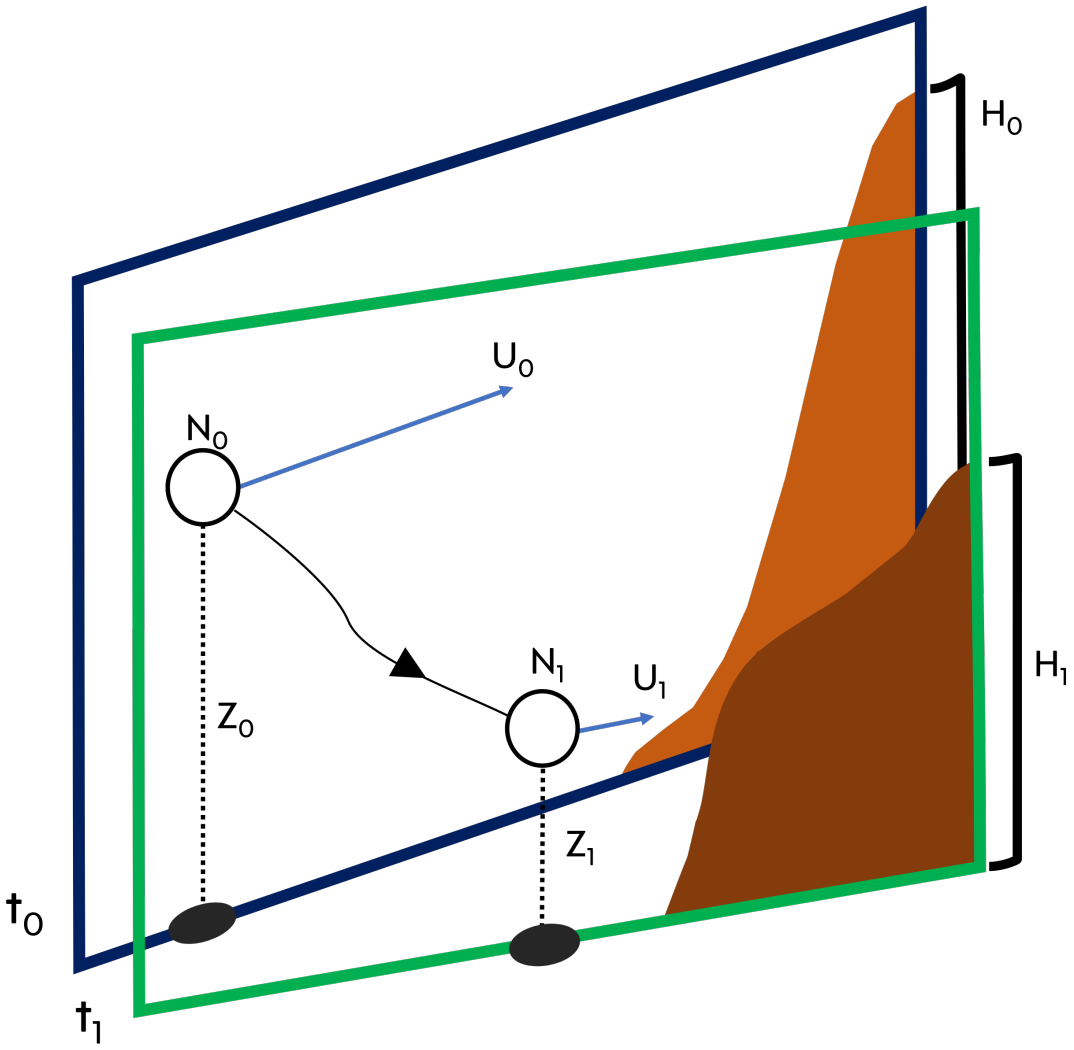

Figure 4.25: A schematic representing the Lagrangian Froude number. At initial time, t_0, a parcel with a characteristic wind speed, height, and Brunt-Väisälä frequency, has a wind direction facing terrain profile, H_0. With these variables, the Froude number can be calculated at t_0. At some time later, t_1, the Froude number can be calculated again using new wind speed, height, Brunt-Väisälä frequency, and terrain height profile, H_1.

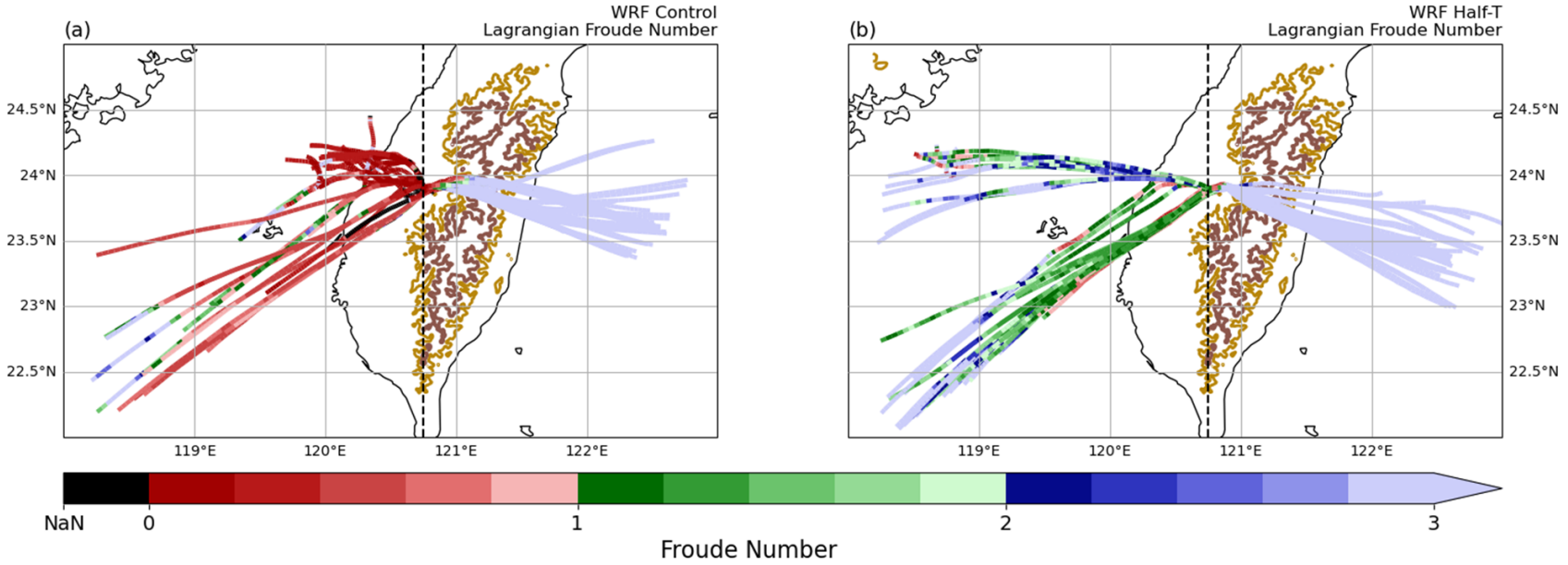

Figure 4.26: Lagrangian Froude number for trajectories found in (a) Fig. 4.23 for WRF Control and (b) Fig. 4.24 for WRF Half-T.

Table 4.1: Number of parcels that reach northern Taiwan for WRF Control.

Control		**Release Group**			
		Release Group 1	Release Group 2	Release Group 3	
Release Height	875 hPa	8/13	4/13	2/13	14/39
	900 hPa	9/13	9/13	4/13	22/39
	925 hPa	8/13	8/13	6/13	22/39
		25/39	21/39	12/39	58/117

Table 4.2: Same as Table 1, but for WRF Half-T.

Half-T		**Release Group**			
		Release Group 1	Release Group 2	Release Group 3	
Release Height	875 hPa	0/13	0/13	0/13	0/39
	900 hPa	4/13	0/13	0/13	4/39
	925 hPa	8/13	3/13	1/13	12/39
		12/39	3/39	1/39	16/117

Chapter 5

Discussion

5.1 Rainfall Duration

In exploring the role of terrain in this 1-3 June 2017 extreme rainfall event, both northern and central Taiwan experience a decrease in rainfall duration with a decrease in terrain height. Similar in both regions, this model-based analysis showed that rainfall duration was linked with slowing of the Mei-yu front. This finding supports and builds upon prior work on this event by Wang et al. (2021) whereby there is a strong negative correlation with rainfall accumulation in northern Taiwan with Mei-yu front speed; although their study did not explicitly separate rainfall duration from intensity. It would be slightly erroneous to state that rainfall forms along the front's wind shift line as in principle, the slight northern tilt of the Mei-yu front separates the heaviest rainfall from convective updrafts induced by low-level frontal convergence (Chen et al. 1998). The distance between rainfall and the wind shift line, however, is not great enough to disassociate the two. Therefore, the heaviest rainfall often forms near the leading edge of the Mei-yu front in general. Regardless of rainfall intensity, stalling the front in a location leads to an increase in rainfall duration.

In northern Taiwan, the method of stalling is through strengthening the low-level prefrontal flow. The prefrontal sector has multiple mechanisms at play that can modify the already moist, monsoonal flow. These mechanisms include, but are not limited to,

the synoptic, marine boundary layer, and barrier jets (Chen et al. 2022). Of these, the barrier jet is the most directly tied to orography and shows evidence in this study of halting the front in northern Taiwan in the Control front at the 900 hPa level (Chen et al. 2022). Although the synoptic and marine boundary layer jets are influenced by large scale mechanisms (Chen et al. 2022), it would be an oversight to rule out modification of their influence given a change in terrain height. Marine boundary layer jets are commonly found below barrier jets near 925 hPa and the synoptic low-level jet core is found between 850-700 hPa, each having potential to become orographically blocked by the CMR (Fig. 4 of Section 4.2). Studying these jets and their relation to orographically induced rainfall are outside the scope of this study and require a larger domain for analysis, but a prior study by Tu et al. (2020) suggests that the marine boundary layer jet induces heavy rainfall in northern Taiwan when in contact with the terrain and the Mei-yu front for this case.

No previous studies have explored the Mei-yu front and influence on rainfall in Central Taiwan for this extreme rainfall case. Furthermore, there are no studies that explore the front near the CMR or more generally, the dynamics of any front whose orientation is perpendicular to a mountain range. Therefore, the results of this case study focusing on central Taiwan are a first step in addressing this gap in the literature.

Whereas the front was halted by the barrier jet found in the prefrontal sector in northern Taiwan, the slowing of the Control front in central Taiwan for this case is attributed to weaker postfrontal flow and possibly stronger prefrontal flow. Determining which relationship is more dominant in this region of steep topography will be a future research topic with additional case studies. Regardless, there is evidence of a wind shift line near the CMR which has not been closely examined prior to this study. Even with a reduction in terrain height, a wind shift line is prominent near the CMR. A somewhat analogous study by Xu et al. (2010) found that when Mei-yu fronts are situated east of the Tibetan Plateau, there is little evidence of the front in proximity to the Plateau due to the suppression of convection by downsloping westerlies. By this logic, with the Mei-yu front situated to the west of the CMR, frontal development on the slopes is aided by orographic

lift on both sides of the front. However, the June 2017 case study shows substantial differences in frontal placement between the Control and Half-T runs near the CMR that has implications on rainfall location and duration.

A challenge in determining frontal progression in central Taiwan is determining under what circumstances postfrontal winds curve counterclockwise to form westerlies, as seen in the Control run, compared to northwesterlies, as seen in the Half-T run. One hypothesis is a Kármán vortex forming in northwest Taiwan from diverted postfrontal winds originating in northeast Taiwan (Schär and Smith 1993; Schär and Durran 1997), which is also a common feature of track discontinuities of tropical cyclones in southeast Taiwan forming leeside cyclones in the northwest (Lin et al. 2002; Lin et al. 2005). In theory, an increase in Froude number, as seen throughout the results of the Half-T run, results in a larger Kármán vortex radius (Heinze et al. 2012). As such, the larger vortex radius, as seen in the Half-T postfrontal sector results in northwesterlies impinging on the front rather than the westerlies in the Control run resulting from a smaller vortex. A limitation of this reasoning is the seemingly incomplete cyclone in the Half-T run with no southerly branch near the CMR, as well as it does not address how the curving postfrontal winds in the Half-T run are stronger than those in the Control run, warranting future analysis with additional case studies.

Another possible explanation for these postfrontal wind differences between runs is found in the northern branch of the postfrontal orographic deformation in the Control run. The northern branch forms southerlies upon colliding with the CMR which flows opposite to north-northeasterly winds in northern Taiwan, creating a small cyclone that forms clockwise rotation in the vicinity (Fig. 2a of Section 4.3). This pattern creates a bit of a dilemma, however, since the orographic deformation seen in the postfrontal sector of the Control run relies on turning of postfrontal winds into westerlies. This scenario could be considered a "chicken or the egg" situation whereby the westerlies leading to orographic deformation are attributed to a cyclone, but the cyclone is induced by the orographic deformation. In all possibility, both theories could be present in the model runs, though it

may not be important as the results from the Half-T trajectory analysis show that parcels originate far west of the coastline and propagate along the front. Regardless, explaining how these postfrontal and prefrontal flows converge determines frontal propagation speed and in turn, contributes to the duration of rainfall in central Taiwan.

A mechanism not addressed in the results of this study is that regardless of where the front is placed, there is nearly constant precipitation in the SMR and CMR for the Control run. Although relatively light, it contributes to increasing rainfall duration in the high terrain. A reason why this precipitation is not as predominant in the Half-T run is due to the decrease in orographic lift seen in the run. This orographic precipitation does also modify intensity, but it will be discussed in the next section.

5.2 Rainfall Intensity

While frontal placement is linked to duration, as heavy rainfall was found to be collocated with the front, light rainfall also was nearly constantly observed in the SMR and CMR in the Control run, contributing to the overall rainfall accumulation. This rainfall was not as predominant in the Half-T run, likely owing to the decrease in orographic lift, which overall can influence rainfall intensity. In this case study, a noticeable change in rainfall intensity was only notable in central Taiwan. Despite the 5-10-knot difference in the prefrontal flow attributed to the barrier jet strengths in northern Taiwan, that presumably would lead to stronger convergence in the Control run and in turn, stronger lift and precipitation, but intensity differences in northern Taiwan between runs were minimal. For much of northern Taiwan, modeled rainfall totals match QPESUMS. The Control run slightly overproduces rainfall suggesting that the lift along the front is sufficiently large such that strengthening prefrontal flow is limited in its ability to increase lift. Thus, rainfall intensity along the front does not change noticeably. Therefore, the terrain modification of rainfall is most pronounced through the aforementioned influence on rainfall duration.

In central Taiwan, there is a more substantial change in intensity between model runs. With a decrease in terrain height, there is a decrease in rainfall intensity. The strength

of the front is likely not responsible for this difference especially when considering the heaviest rainfall is likely associated with the MCSes forming far upstream from the CMR in the Taiwan Strait and propagating east. These MCSes can be seen on a larger scale through the channel 10 brightness temperatures of Himawari-8 (Fig. 3.3). Therefore, the speculated difference could be due to orographic lift. Conventional knowledge states that the updraft induced by topography is dependent on the gradient of the terrain and the wind speed incident upon it (Lin et al. 2001). If the wind speed increases or if a mountain becomes steeper (i.e. aspect ratio increase), the lift will increase. Within our model runs, the reduced terrain height simply acts to deter orographic lift and coincidentally orographically enhanced precipitation.

Idealized studies define mountain aspect ratios as:

$$A = \frac{h}{w} \tag{5.1}$$

Where h is the mountain height and w is the mountain halfwidth (Chen and Lin 2005; Chen et al. 2008). By reducing mountain aspect ratio, idealized flows produced precipitation farther upstream from the mountain peak and thus has an influence on rainfall location. Those studies, however, are idealized and thus do not account for frontal structures with prefrontal and postfrontal flows as well as a 3-dimensional mountain range. However, this study's model runs do show that precipitation occurred farther west on the slopes of the CMR for the Half-T run, suggesting a future application of the idealized aspect ratio framework to investigating terrain-influenced rainfall in additional Mei-yu front studies in this region.

Chapter 6

Summary and Conclusions

On 2 June 2017, a strong Mei-yu front made landfall on the northern coastline of Taiwan. Over the next two days, the front progressed south through the island, leading to extreme amounts of rainfall that produced widespread damage to infrastructure and endangered the populace. Notable regions of impact were Taipei Basin in northern Taiwan receiving upwards of 600 mm of rainfall in a 12-hour span and central Taiwan where the maximum 48 hour rainfall recorded was found in the CMR with approximately 1500 mm of rainfall. This event captured both aspects of extreme rainfall, high duration and high intensity, and acts as an ideal case to study orographic influences on extreme precipitation.

This event was simulated using the WRF model creating a Control run and an experimental run (Half-T) where the terrain height was halved to determine orographic influences on rainfall intensity, duration, and location during this event. The findings are as follows:

1. In decreasing the terrain height, the strength of the orographically induced barrier jet was decreased. This weakened barrier jet was not able to resist southern propagation of the Mei-yu front in northern Taiwan compared to the stronger barrier jet in the Control run.

2. In central Taiwan, orographic deformation on both sides of the Control front acted to slow southern propagation of the Mei-yu front while the stronger postfrontal winds

of the Half-T run pushed the front south.

3. In both northern and central Taiwan, slowing the propagation of the Mei-yu front acted to the increase rainfall duration, therefore rainfall duration was lower in the Half-T run.

4. Rainfall intensity was found to not differ significantly between model runs in northern Taiwan, but was greater in central Taiwan for the Control run due to stronger orographic lift. Orographic precipitation in the Half-T run is weaker due to less orographic lift and a shift in rainfall location due to a change in mountain aspect ratio.

It was found that regardless of model run, increasing terrain height results in greater rainfall duration. A difference between model runs is that the Control run sees an increase in rainfall intensity at high rainfall duration as terrain height increases whereas rainfall intensity distributions in the Half-T run are mostly similar regardless of terrain height. By using a bi-variate choropleth of intensity and duration, with a decrease in terrain height, rainfall duration decreases in both northern and central Taiwan and rainfall intensity decreases in central Taiwan only.

The decrease in rainfall duration in northern Taiwan with a decrease in rainfall duration is attributed to a decrease in the barrier jet strength. Orographic blocking of monsoonal, southwesterly flow in central and southern Taiwan, diverts flow downstream to northwestern Taiwan where it converges with the mean flow to induce a jet at low levels (Fig. 6.1). With a reduction in terrain height, the orographic blocking in central and southern Taiwan is weakened, resulting in weaker diversion of flow to northern Taiwan, manifesting in a barrier jet that is 5-10 knots weaker than the Control run. With a weaker barrier jet, the prefrontal flow is less resistant to the Mei-yu front's southern advancement, thus the front's propagation speed is faster than in the Control run. The most intense rainfall is collocated with the location of the front. Therefore, by speeding up the propagation speed of the front, rainfall duration drops in the Half-T run while in

northern Taiwan.

In central Taiwan, this work represents a first effort to study the dynamics of a front perpendicular to a mesoscale mountain range. The decrease in terrain height results in a decrease in rainfall duration and intensity in central Taiwan. Much like northern Taiwan, extreme rainfall is tethered to the location of the Mei-yu front and rainfall duration is inversely correlated to the Mei-yu front's propagation speed. While there are slight changes to prefrontal orographic deformation between model runs, the postfrontal sectors are what determines frontal propagation speed. Whereas most of the Half-T postfrontal sector converges with prefrontal flow, the only portion of the Control run's postfrontal sector that converges with the prefrontal sector is flow that orographically deforms (Fig. 6.2). All of these assertions are in proximity to the CMR and rainfall in the CMR is linked to the location of the front near the terrain regardless of where the front is over the ocean. Rainfall intensity is linked to orographic lift which is predominantly altered by the gradient of the terrain. Therefore, with a decrease in terrain height, orographic lift is decreased in the Half-T run and with it, a decrease in rainfall intensity.

Future work acts to address shortcomings of this work as well as expanding upon it. A limitation in this study is that while the mesoscale aspects of this event were faithfully reproduced, the microscale was not, with exaggerated amounts of ice hydrometeors produced in WRF when compared to radar-inferred hydrometeors. A possible byproduct of this misrepresentation of the microphysics is a lack of postfrontal stratiform precipitation in northern Taiwan that is observed in the operational radars. This lack of stratiform precipitation has implications for rainfall duration and intensity. As such, next steps will compare microphysics schemes to address this problem and begin assessing how altering the terrain height modifies the microphysical structure of precipitation in and outside of the Mei-yu front in proximity to terrain.

Expanding outside of this event, the findings of this study will be compared with radar observations and model results of IOPs 1 and 3 of PRECIP 2022, which are both Mei-yu fronts that exhibited high rainfall accumulations but with varying intensities and

durations. Each IOP produced upwards of 300 mm of rainfall in northwestern Taiwan, but IOP 1 lasted 2 days whereas IOP 3 lasted 6.5 days. The advantage to studying these events from the PRECIP 2022 campaign is that their peak rainfall was well captured by the S-band dual-polarization radar, S-Pol. This radar allowed for high vertical resolution observations of the hydrometeor profiles within the Mei-yu fronts in proximity to the terrain. By utilizing this tool, the effects of different microphysical processes and how they modify intensity and duration of extreme rainfall in complex terrain can be explored.

6.1 Figures

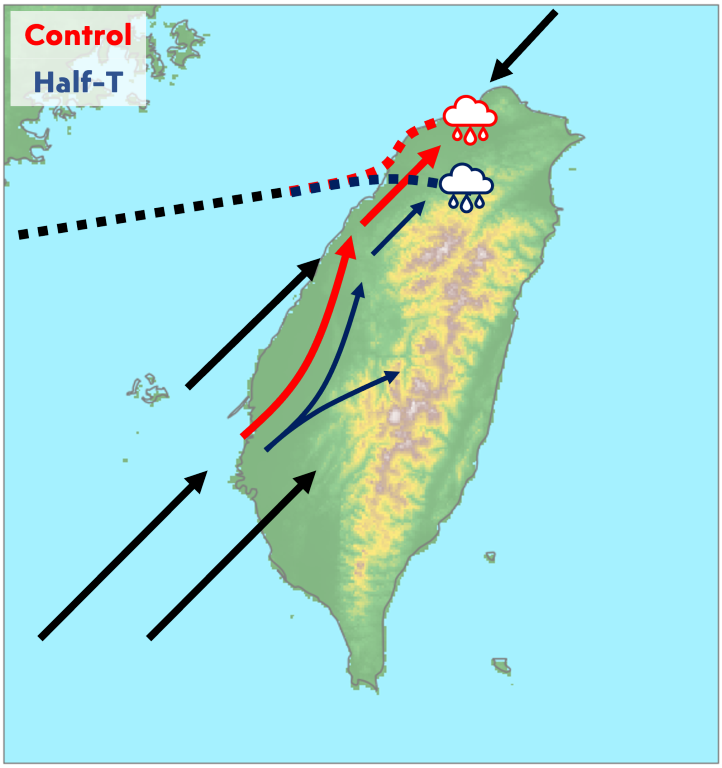

Figure 6.1: A schematic representing the effect of halving terrain height on the barrier jet strength. The common prefrontal and postfrontal winds are represented by the black arrows. Placement of the Mei-yu Front is represented by the dashed line. Prefrontal southwesterly flow encounters the CMR and becomes orographically blocked. In both model runs, this flow is diverted to northern Taiwan, but since orographic blocking is weaker for the Half-T run, a portion is orographically lifted over the CMR (blue). Flow that is diverted converges with the mean southwesterly flow to form a barrier jet over northwestern Taiwan with the barrier jet in the Control run (red) being stronger than the barrier jet found in the Half-T run. This difference in barrier jet strength between model runs causes a division in Mei-yu frontal progression speed with the Control front progressing south slower than that of the Half-T front. In both model runs, extreme rainfall occurs along the front.

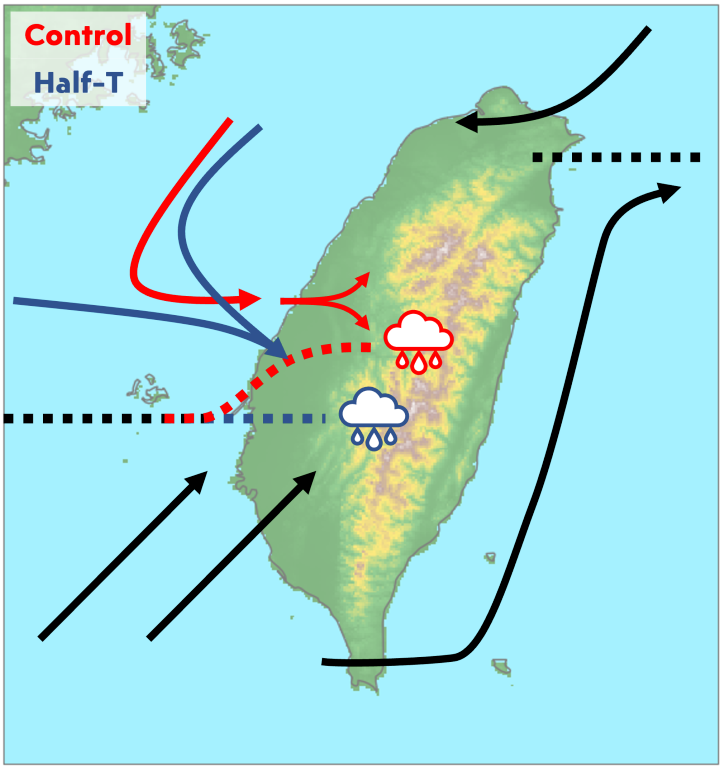

Figure 6.2: A schematic representing the effect of halving terrain height on the Mei-yu front positioning in central Taiwan. The common prefrontal and postfrontal winds are represented by the black arrows. Placement of the Mei-yu Front is represented by the dashed line. Prefrontal southwesterly flow is split by the CMR with a portion reaching toward west central Taiwan and another portion wrapping around the CMR to converge with postfrontal northwesterlies. In the Control run (red), postfrontal winds curve from northeasterlies into westerlies. These westerlies become orographically blocked by the SMR and northern CMR, deforming into weak southwesterlies and northeasterlies. These weak northeasterlies converge with the prefrontal flow to form the front near the terrain. In the Half-T run, postfrontal winds curve from northeasterlies to northwesterlies, converging with the prefrontal southwesterlies and pushing the Mei-yu front south. In both model runs, extreme rainfall in the terrain occurs downstream of the front.

Bibliography

Allen, Sarah M. et al., eds. (2015). *The Poetry of Du Fu*. De Gruyter. ISBN: 9781614517122. DOI: 10.1515/9781501501890.

Antofie, T. et al. (2015). "Estimating the water needed to end the drought or reduce the drought severity in the Carpathian region". In: *Hydrology and Earth System Sciences* 19.1, pp. 177–193. DOI: https://doi.org/10.5194/hess-19-177-2015. URL: https://hess.copernicus.org/articles/19/177/2015/.

Arakane, Sho et al. (2019). "Remote effect of a tropical cyclone in the Bay of Bengal on a heavy-rainfall event in subtropical East Asia". In: *npj Climate and Atmospheric Science* 2.1, p. 25. ISSN: 2397-3722. DOI: 10.1038/s41612-019-0082-8. URL: https://doi.org/10.1038/s41612-019-0082-8.

Bell, Michael M. (2022). *nsf-lrose/lrose-topaz: lrose-topaz-20220222*. DOI: 10.5281/ZENODO.6909478. URL: https://zenodo.org/record/6909478.

Blumen, W. (1992). "Propagation of fronts and frontogenesis versus frontolysis over orography". In: *Meteorology and Atmospheric Physics* 48.1, pp. 37–50. ISSN: 1436-5065. DOI: 10.1007/BF01029558. URL: https://doi.org/10.1007/BF01029558.

Chang, C-P. and George T-J. Chen (1995). "Tropical Circulations Associated with Southwest Monsoon Onset and Westerly Surges over the South China Sea". In: *Monthly Weather Review* 123.11, pp. 3254–3267. DOI: 10.1175/1520-0493(1995)123<3254:TCAWSM>2.0.CO;2. URL: https://journals.ametsoc.org/view/journals/mwre/123/11/1520-0493_1995_123_3254_tcawsm_2_0_co_2.xml.

Chang, Pao-Liang et al. (2021). "An Operational Multi-Radar Multi-Sensor QPE System in Taiwan". In: *Bulletin of the American Meteorological Society* 102.3, E555–E577. DOI: 10.1175/BAMS-D-20-0043.1. URL: https://journals.ametsoc.org/view/journals/bams/102/3/BAMS-D-20-0043.1.xml.

Chen, George Tai-Jen (1992). "Mesoscale Features Observed in the Taiwan Mei-Yu Season". In: *Journal of the Meteorological Society of Japan. Ser. II* 70.1B, pp. 497–516. DOI: 10.2151/jmsj1965.70.1B_497.

Chen, George Tai-Jen, Chung-Chieh Wang, and An-Hsiang Wang (2007). "A Case Study of Subtropical Frontogenesis during a Blocking Event". In: *Monthly Weather Review* 135.7, pp. 2588–2609. DOI: 10.1175/MWR3412.1. URL: https://journals.ametsoc.org/view/journals/mwre/135/7/mwr3412.1.xml.

Chen, Yi-Leng, Xin An Chen, et al. (1997). "A Numerical Study of the Low-Level Jet during TAMEX IOP 5". In: *Monthly Weather Review* 125.10, pp. 2583–2604. DOI: 10.1175/1520-0493(1997)125<2583:ANSOTL>2.0.CO;2. URL: https://journals.ametsoc.org/view/journals/mwre/125/10/1520-0493_1997_125_2583_ansotl_2.0.co_2.xml.

Chen, Yi-Leng and Norman B-F. Hui (1990). "Analysis of a Shallow Front during the Taiwan Area Mesoscale Experiment". In: *Monthly Weather Review* 118.12, pp. 2649–2667. DOI: 10.1175/1520-0493(1990)118<2649:AOASFD>2.0.CO;2. URL: https://journals.ametsoc.org/view/journals/mwre/118/12/1520-0493_1990_118_2649_aoasfd_2_0_co_2.xml.

Chen, Yi-Leng, Chuan-Chi Tu, et al. (2022). "An Overview of Low-Level Jets (LLJs) and Their Roles in Heavy Rainfall over the Taiwan Area during the Early Summer Rainy Season". In: *Meteorology* 1.1, pp. 64–112. ISSN: 2674-0494. DOI: 10.3390/meteorology1010006. URL: https://www.mdpi.com/2674-0494/1/1/6.

Chen, Yi-Leng, Yu-Xia Zhang, and Norman B-F. Hui (1989). "Analysis of a Surface Front during the Early Summer Rainy Season over Taiwan". In: *Monthly Weather Review* 117.5, pp. 909–931. DOI: 10.1175/1520-0493(1989)117<0909:AOASFD>2.0.CO;2.

URL: https://journals.ametsoc.org/view/journals/mwre/117/5/1520-0493_1989_117_0909_aoasfd_2_0_co_2.xml.

Chen, Shou-Jun et al. (1998). "A Modeling Case Study of Heavy Rainstorms along the Mei-Yu Front". In: *Monthly Weather Review* 126.9, pp. 2330–2351. DOI: 10.1175/1520-0493(1998)126<2330:AMCSOH>2.0.CO;2. URL: https://journals.ametsoc.org/view/journals/mwre/126/9/1520-0493_1998_126_2330_amcsoh_2.0.co_2.xml.

Chen, Shu-Hua and Yuh-Lang Lin (2005). "Effects of Moist Froude Number and CAPE on a Conditionally Unstable Flow over a Mesoscale Mountain Ridge". In: *Journal of the Atmospheric Sciences* 62.2, pp. 331–350. DOI: 10.1175/JAS-3380.1. URL: https://journals.ametsoc.org/view/journals/atsc/62/2/jas-3380.1.xml.

Chen, Shu-Hua, Yuh-Lang Lin, and Zhan Zhao (2008). "Effects of Unsaturated Moist Froude Number and Orographic Aspect Ratio on a Conditionally Unstable Flow over a Mesoscale Mountain". In: *Journal of the Meteorological Society of Japan. Ser. II* 86.2, pp. 353–367. DOI: 10.2151/jmsj.86.353.

Chi, Shui-Shang and Guo-Ji Jian (2008). "Effects of Taiwan Terrain on the Flash Flood Event of 12 June 2005". In: URL: https://photino.cwb.gov.tw/rdcweb/lib/cd/cd01conf/dissertation/2008-2/18.pdf.

Cho, Han-Ru and George T. J. Chen (1995). "Mei-Yu Frontogenesis". In: *Journal of Atmospheric Sciences* 52.11, pp. 2109–2120. DOI: 10.1175/1520-0469(1995)052<2109:MYF>2.0.CO;2. URL: https://journals.ametsoc.org/view/journals/atsc/52/11/1520-0469_1995_052_2109_myf_2_0_co_2.xml.

Dickinson, Michael J. and David J. Knight (1999). "Frontal Interaction with Mesoscale Topography". In: *Journal of the Atmospheric Sciences* 56.20, pp. 3544–3559. DOI: 10.1175/1520-0469(1999)056<3544:FIWMT>2.0.CO;2. URL: https://journals.ametsoc.org/view/journals/atsc/56/20/1520-0469_1999_056_3544_fiwmt_2.0.co_2.xml.

Dixon, M et al. (2016). "CfRadial data file format". In: *Technical report, EOL, NCAR.*

Doswell, Charles A., Harold E. Brooks, and Robert A. Maddox (1996). "Flash Flood Forecasting: An Ingredients-Based Methodology". In: *Weather and Forecasting* 11.4, pp. 560–581. DOI: 10.1175/1520-0434(1996)011<0560:FFFAIB>2.0.CO;2. URL: https://journals.ametsoc.org/view/journals/wefo/11/4/1520-0434_1996_011_0560_fffaib_2_0_co_2.xml.

Egger, J. (1992). "The orographic deformation and retardation of a frontal zone". In: *Meteorology and Atmospheric Physics* 48.1, pp. 131–137. ISSN: 1436-5065. DOI: 10.1007/BF01029563. URL: https://doi.org/10.1007/BF01029563.

European Centre for Medium-Range Weather Forecasts (2019). *ERA5 Reanalysis (0.25 Degree Latitude-Longitude Grid)*. Boulder CO. URL: https://doi.org/10.5065/BH6N-5N20.

Gochis, David et al. (2015). "The Great Colorado Flood of September 2013". In: *Bulletin of the American Meteorological Society* 96.9, pp. 1461–1487. DOI: 10.1175/BAMS-D-13-00241.1. URL: https://journals.ametsoc.org/view/journals/bams/96/9/bams-d-13-00241.1.xml.

Heinze, Rieke, Siegfried Raasch, and Dieter Etling (2012). "The structure of Kármán vortex streets in the atmospheric boundary layer derived from large eddy simulation". In: *Meteorologische Zeitschrift* 21.3, pp. 221–237. DOI: 10.1127/0941-2948/2012/0313. URL: http://dx.doi.org/10.1127/0941-2948/2012/0313.

Helmus, Jonathan J. and Scott M. Collis (2016). "The Python ARM Radar Toolkit (Py-ART), a library for working with weather radar data in the Python programming language". In: *Journal of Open Research Software* 4. ISSN: 2049-9647. DOI: 10.5334/jors.119. URL: https://www.osti.gov/biblio/1339572.

Henny, Lexi et al. (2021). "Extreme Rainfall in Taiwan: Seasonal Statistics and Trends". In: *Journal of Climate* 34.12, pp. 4711–4731. DOI: 10.1175/JCLI-D-20-0999.1. URL: https://journals.ametsoc.org/view/journals/clim/34/12/JCLI-D-20-0999.1.xml.

Hong, Song-You, Yign Noh, and Jimy Dudhia (2006). "A New Vertical Diffusion Package with an Explicit Treatment of Entrainment Processes". In: *Monthly Weather Review* 134.9, pp. 2318–2341. DOI: 10.1175/MWR3199.1. URL: https://journals.ametsoc.org/view/journals/mwre/134/9/mwr3199.1.xml.

Hor, Tai-Hwa, Mou-Hsiang Chang, and Ben Jong-Dao Jou (1998). "Mesoscale Structures of Air Flow in a Mei-yu Front Leading Edge Observed by Aircraft off the East Coast of Taiwan during TAMEX IOP 9". In: *Journal of the Meteorological Society of Japan. Ser. II* 76.4, pp. 473–496. DOI: 10.2151/jmsj1965.76.4_473.

Houze Jr., Robert A. (2004). "Mesoscale convective systems". In: *Reviews of Geophysics* 42.4. DOI: https://doi.org/10.1029/2004RG000150. URL: https://agupubs.onlinelibrary.wiley.com/doi/abs/10.1029/2004RG000150.

Iacono, Michael J. et al. (2008). "Radiative forcing by long-lived greenhouse gases: Calculations with the AER radiative transfer models". In: *Journal of Geophysical Research: Atmospheres* 113.D13. DOI: https://doi.org/10.1029/2008JD009944. eprint: https://agupubs.onlinelibrary.wiley.com/doi/pdf/10.1029/2008JD009944. URL: https://agupubs.onlinelibrary.wiley.com/doi/abs/10.1029/2008JD009944.

Janić, Zaviša I (2001). "Nonsingular implementation of the Mellor-Yamada level 2.5 scheme in the NCEP Meso model". In: URL: https://repository.library.noaa.gov/view/noaa/11409.

Jhun, Jong-Ghap and Eun-Jeong Lee (2004). "A New East Asian Winter Monsoon Index and Associated Characteristics of the Winter Monsoon". In: *Journal of Climate* 17.4, pp. 711–726. DOI: 10.1175/1520-0442(2004)017<0711:ANEAWM>2.0.CO;2. URL: https://journals.ametsoc.org/view/journals/clim/17/4/1520-0442_2004_017_0711_aneawm_2.0.co_2.xml.

Jong, Ben et al. (2011). "An Overview of SoWMEX/TiMREX". In: *The Global Monsoon System: Research and Forecast*, pp. 303–318. DOI: 10.1142/9789814343411_0018.

Ke, Ching-Yin et al. (2019). "Analysis of heavy rainfall and barrier-jet evolution during Mei-Yu season using multiple Doppler radar retrievals: a case study on 11 June 2012".

In: *Tellus A: Dynamic Meteorology and Oceanography* 71.1, p. 1571369. DOI: 10.1080/16000870.2019.1571369. URL: https://doi.org/10.1080/16000870.2019.1571369.

Kirshbaum, Daniel J. et al. (2018). "Moist Orographic Convection: Physical Mechanisms and Links to Surface-Exchange Processes". In: *Atmosphere* 9.3. ISSN: 2073-4433. DOI: 10.3390/atmos9030080. URL: https://www.mdpi.com/2073-4433/9/3/80.

Kuo, Ying-Hwa and George Tai-Jen Chen (1990). "The Taiwan Area Mesoscale Experiment (TAMEX): An Overview". In: *Bulletin of the American Meteorological Society* 71.4, pp. 488–503. DOI: 10.1175/1520-0477(1990)071<0488:TTAMEA>2.0.CO;2. URL: https://journals.ametsoc.org/view/journals/bams/71/4/1520-0477_1990_071_0488_ttamea_2_0_co_2.xml.

Ladwig, W (2017). "wrf-python (Version 1.3. 2.)" In: *UCAR/NCAR [code], doi. org/10.5065/D6W094P1*.

Li, Chih-Hsin et al. (2020). "The Taiwan WRF Ensemble Prediction System: Scientific Description, Model-Error Representation and Performance Results". In: *Asia-Pacific Journal of Atmospheric Sciences* 56.1, pp. 1–15. ISSN: 1976-7951. DOI: 10.1007/s13143-019-00127-8. URL: https://doi.org/10.1007/s13143-019-00127-8.

Li, Jun and Yi-Leng Chen (1998). "Barrier Jets during TAMEX". In: *Monthly Weather Review* 126.4, pp. 959–971. DOI: 10.1175/1520-0493(1998)126<0959:BJDT>2.0.CO;2. URL: https://journals.ametsoc.org/view/journals/mwre/126/4/1520-0493_1998_126_0959_bjdt_2.0.co_2.xml.

Lien, Tzu-Yi et al. (2022). "Variations in GPS precipitable water vapor and rainfall during the 2006–2019 Mei-yu season in Taiwan". In: *Advances in Space Research* 70.5, pp. 1375–1387. ISSN: 0273-1177. DOI: https://doi.org/10.1016/j.asr.2022.05.065. URL: https://www.sciencedirect.com/science/article/pii/S027311772200446X.

Lin, Yuh-Lang (1993). "Orographic Effects on Airflow and Mesoscale Weather Systems Over Taiwan". In: *Terrestrial, Atmospheric and Oceanic Sciences* 4.4, pp. 381–420. ISSN: 1017-0839.

Lin, Yuh-Lang, Shu-Yun Chen, et al. (2005). "Control Parameters for the Influence of a Mesoscale Mountain Range on Cyclone Track Continuity and Deflection". In: *Journal of the Atmospheric Sciences* 62.6, pp. 1849–1866. DOI: 10.1175/JAS3439.1. URL: https://journals.ametsoc.org/view/journals/atsc/62/6/jas3439.1.xml.

Lin, Yuh-Lang, Sen Chiao, et al. (2001). "Some Common Ingredients for Heavy Orographic Rainfall". In: *Weather and Forecasting* 16.6, pp. 633–660. DOI: 10.1175/1520-0434(2001)016<0633:SCIFHO>2.0.CO;2. URL: https://journals.ametsoc.org/view/journals/wefo/16/6/1520-0434_2001_016_0633_scifho_2_0_co_2.xml.

Lin, Yuh-Lang, Darrell B. Ensley, et al. (2002). "Orographic Influences on Rainfall and Track Deflection Associated with the Passage of a Tropical Cyclone". In: *Monthly Weather Review* 130.12, pp. 2929–2950. DOI: 10.1175/1520-0493(2002)130<2929:OIORAT>2.0.CO;2. URL: https://journals.ametsoc.org/view/journals/mwre/130/12/1520-0493_2002_130_2929_oiorat_2.0.co_2.xml.

Liu, Weiwei et al. (2022). "Excessive Rainfall Is the Key Meteorological Limiting Factor for Winter Wheat Yield in the Middle and Lower Reaches of the Yangtze River". In: *Agronomy* 12.1. ISSN: 2073-4395. DOI: 10.3390/agronomy12010050. URL: https://www.mdpi.com/2073-4395/12/1/50.

LoneSky (2020). *Python Script for Himawari-8*. URL: https://loneskyimages.blogspot.com/2020/04/python-script-for-himawari-8.html.

Luo, Yali, Yu Gong, and Da-Lin Zhang (2014). "Initiation and Organizational Modes of an Extreme-Rain-Producing Mesoscale Convective System along a Mei-Yu Front in East China". In: *Monthly Weather Review* 142.1, pp. 203–221. DOI: 10.1175/MWR-D-13-00111.1. URL: https://journals.ametsoc.org/view/journals/mwre/142/1/mwr-d-13-00111.1.xml.

May, Ryan M. et al. (2022). "MetPy: A Meteorological Python Library for Data Analysis and Visualization". In: *Bulletin of the American Meteorological Society* 103.10, E2273–E2284. DOI: 10.1175/BAMS-D-21-0125.1. URL: https://journals.ametsoc.org/view/journals/bams/103/10/BAMS-D-21-0125.1.xml.

Ninomiya, K. (1984). "Characteristics of Baiu Front as a Predominant Subtropical Front in the Summer Northern Hemisphere". In: *Journal of the Meteorological Society of Japan. Ser. II* 62.6, pp. 880–894. DOI: 10.2151/jmsj1965.62.6_880.

NWS (2015). *A statistical preview of Denver's September weather*. URL: https://www.weather.gov/bou/sept2015_denver_statpreview.

Parfitt, Rhys, Arnaud Czaja, and Hyodae Seo (2017). "A simple diagnostic for the detection of atmospheric fronts". In: *Geophysical Research Letters* 44.9, pp. 4351–4358. DOI: https://doi.org/10.1002/2017GL073662. eprint: https://agupubs.onlinelibrary.wiley.com/doi/pdf/10.1002/2017GL073662. URL: https://agupubs.onlinelibrary.wiley.com/doi/abs/10.1002/2017GL073662.

Pierrehumbert, R. T. (1984). "Linear Results on the Barrier Effects of Mesoscale Mountains". In: *Journal of Atmospheric Sciences* 41.8, pp. 1356–1367. DOI: 10.1175/1520-0469(1984)041<1356:LROTBE>2.0.CO;2. URL: https://journals.ametsoc.org/view/journals/atsc/41/8/1520-0469_1984_041_1356_lrotbe_2_0_co_2.xml.

Pierrehumbert, R. T. and B. Wyman (1985). "Upstream Effects of Mesoscale Mountains". In: *Journal of Atmospheric Sciences* 42.10, pp. 977–1003. DOI: 10.1175/1520-0469(1985)042<0977:UEOMM>2.0.CO;2. URL: https://journals.ametsoc.org/view/journals/atsc/42/10/1520-0469_1985_042_0977_ueomm_2_0_co_2.xml.

PRECIP (2022). *Precip 2022 Science Overview*. URL: http://precip.org/science/.

Reid, A. M., S. D. Fuhlendorf, and J. R. Weir (2010). "Weather Variables Affecting Oklahoma Wildfires". In: *Rangeland Ecology & Management* 63.5, pp. 599–603. ISSN: 1550-7424. DOI: https://doi.org/10.2111/REM-D-09-00132.1. URL: https://www.sciencedirect.com/science/article/pii/S1550742410500587.

Schär, Christoph and Dale R. Durran (1997). "Vortex Formation and Vortex Shedding in Continuously Stratified Flows past Isolated Topography". In: *Journal of the Atmospheric Sciences* 54.4, pp. 534–554. DOI: 10.1175/1520-0469(1997)054<0534:VFAVSI>2.0.CO;2. URL: https://journals.ametsoc.org/view/journals/atsc/54/4/1520-0469_1997_054_0534_vfavsi_2.0.co_2.xml.

Schär, Christoph and Ronald B. Smith (1993). "Shallow-Water Flow past Isolated Topography. Part II: Transition to Vortex Shedding". In: *Journal of Atmospheric Sciences* 50.10, pp. 1401–1412. DOI: 10.1175/1520-0469(1993)050<1401:SWFPIT>2.0.CO;2. URL: https://journals.ametsoc.org/view/journals/atsc/50/10/1520-0469_1993_050_1401_swfpit_2_0_co_2.xml.

Skamarock, William C et al. (2019). "A description of the advanced research WRF model version 4". In: *National Center for Atmospheric Research: Boulder, CO, USA* 145.145, p. 550.

Tewari, Mukul et al. (2004). "Implementation and verification of the unified NOAH land surface model in the WRF model". In: *20th conference on weather analysis and forecasting/16th conference on numerical weather prediction*. Vol. 1115. 6, pp. 2165–2170.

Thompson, Gregory and Trude Eidhammer (2014). "A Study of Aerosol Impacts on Clouds and Precipitation Development in a Large Winter Cyclone". In: *Journal of the Atmospheric Sciences* 71.10, pp. 3636–3658. DOI: 10.1175/JAS-D-13-0305.1. URL: https://journals.ametsoc.org/view/journals/atsc/71/10/jas-d-13-0305.1.xml.

Trier, Stanley B., David B. Parsons, and Thomas J. Matejka (1990). "Observations of a Subtropical Cold Front in a Region of Complex Terrain". In: *Monthly Weather Review* 118.12, pp. 2449–2470. DOI: 10.1175/1520-0493(1990)118<2449:OOASCF>2.0.CO;2. URL: https://journals.ametsoc.org/view/journals/mwre/118/12/1520-0493_1990_118_2449_ooascf_2_0_co_2.xml.

Tu, Chuan-Chi, Yi-Leng Chen, Pay-Liam Lin, and Yu Du (2019). "Characteristics of the Marine Boundary Layer Jet over the South China Sea during the Early Summer Rainy Season of Taiwan". In: *Monthly Weather Review* 147.2, pp. 457–475. DOI: 10.1175/MWR-D-18-0230.1. URL: https://journals.ametsoc.org/view/journals/mwre/147/2/mwr-d-18-0230.1.xml.

Tu, Chuan-Chi, Yi-Leng Chen, Pay-Liam Lin, and Mu-Qun Huang (2022). "Analysis and Simulations of a Heavy Rainfall Event Associated with the Passage of a Shallow Front over Northern Taiwan on 2 June 2017". In: *Monthly Weather Review* 150.3, pp. 505–

528. DOI: 10.1175/MWR-D-21-0113.1. URL: https://journals.ametsoc.org/view/journals/mwre/150/3/MWR-D-21-0113.1.xml%22.

Tu, Chuan-Chi, Yi-Leng Chen, Pay-Liam Lin, and Po-Hsiung Lin (2020). "The relationship between the boundary layer moisture transport from the South China Sea and heavy rainfall over Taiwan". In: *Terrestrial, Atmospheric and Oceanic Sciences* 31, pp. 159–176.

Wang, C.-C. et al. (2022). "A modelling study of an extreme rainfall event along the northern coast of Taiwan on 2 June 2017". In: *Atmospheric Chemistry and Physics Discussions* 2022, pp. 1–39. DOI: 10.5194/acp-2022-377. URL: https://acp.copernicus.org/preprints/acp-2022-377/.

Wang, Chung-Chieh, Chu-Ying Kung, et al. (2012). "Development and Evaluation of Mei-Yu Season Quantitative Precipitation Forecasts in Taiwan River Basins Based on a Conceptual Climatology Model". In: *Weather and Forecasting* 27.3, pp. 586–607. DOI: 10.1175/WAF-D-11-00098.1. URL: https://journals.ametsoc.org/view/journals/wefo/27/3/waf-d-11-00098_1.xml.

Wang, Chung-Chieh, Ming-Siang Li, et al. (2021). "Ensemble-based sensitivity analysis and predictability of an extreme rainfall event over northern Taiwan in the Mei-yu season: The 2 June 2017 case". In: *Atmospheric Research* 259, p. 105684. ISSN: 0169-8095. DOI: https://doi.org/10.1016/j.atmosres.2021.105684. URL: https://www.sciencedirect.com/science/article/pii/S0169809521002362.

Xu, Xiangde et al. (2010). "Large-scale topography of China: A factor for the seasonal progression of the Meiyu rainband?" In: *Journal of Geophysical Research: Atmospheres* 115.D2. DOI: https://doi.org/10.1029/2009JD012444. eprint: https://agupubs.onlinelibrary.wiley.com/doi/pdf/10.1029/2009JD012444. URL: https://agupubs.onlinelibrary.wiley.com/doi/abs/10.1029/2009JD012444.

Zhang, Qinghong et al. (2000). "Numerical simulation on mesoscale convective system along Mei-Yu front in Southern China". In: *Chinese Science Bulletin* 45, pp. 2093–2096. DOI: https://doi.org/10.1007/BF03183534.

Zhao, Yuchun et al. (2020). "Quasi-stationary extreme rain produced by mesoscale convective system on the Mei-Yu front". In: *Meteorology and Atmospheric Physics* 132.5, pp. 721–742. ISSN: 1436-5065. DOI: 10.1007/s00703-019-00717-1. URL: https://doi.org/10.1007/s00703-019-00717-1.

Zhou, Yushu, Shouting Gao, and Samuel S.P. Shen (2004). "A Diagnostic Study of Formation and Structures of the Meiyu Front System over East Asia". In: *Journal of the Meteorological Society of Japan. Ser. II* 82.6, pp. 1565–1576. DOI: 10.2151/jmsj.82.1565.